

# UC Merced

## UC Merced Electronic Theses and Dissertations

### Title

Lead selenide nanowire solar cells via LPNE and its new found derivatives

### Permalink

<https://escholarship.org/uc/item/9hw977qp>

### Author

Hujdic, Justin

### Publication Date

2012-03-16

Peer reviewed|Thesis/dissertation

UNIVERSITY OF CALIFORNIA, MERCED

**Lead selenide nanowire solar cells via LPNE and  
its new found derivatives**

DISSERTATION

submitted in partial satisfaction of the requirements for the degree of

DOCTOR OF PHILOSOPHY

in Chemistry

by

**Justin Hujdic**

Dissertation Committee:

Professor Erik J. Menke, Adviser

Professor Anne Kelley, Chair

Professor Reginald Penner, UCI

Professor Matthew Meyer, UCM

2012

© 2012 Justin Hujdic

The dissertation of Justin Hujdic is approved, and is acceptable in  
quality and form for publication:

**Committee on Graduate Work:**

---

Adviser      Professor Erik J. Menke

---

Chair      Professor Anne M. Kelley

---

Professor Reginald M. Penner

---

Professor Matthew P. Meyer

University of California, Merced

2012

## **Dedicated To:**

My inspiration family; to my lovely wife Jessica, to my energetic son Joel, and to my future children, this is for you.

# Contents

List of Figures	vi
List of Tables	xiv
Acknowledgements	xv
Curriculum Vitae	xvii
Abstract of the dissertation	xviii
<b>1. Cost-effective solar energy using nanowires</b>	<b>1</b>
1.1 Objectives of the dissertation.....	1
1.2 Motivation for a cost effective solar energy source.....	2
1.3 LMR in semiconductors to enhance device efficiency.....	8
1.4 Plasmonics for light trapping.....	16
<b>2. Lead Selenide Nanowires Prepared by LPNE</b>	<b>24</b>
2.1 Motivation.....	24
2.2 Experimental details.....	30
2.3 Characterization.....	41
<b>3. High-Density Gold Nanowire Arrays</b>	<b>58</b>
3.1 Motivation.....	58
3.2 Experimental details.....	60
3.3 Results.....	68
3.4 Characterizations.....	76
<b>4. PbSe Nanowire Solar Cells</b>	<b>82</b>
4.1 Au-PbSe core-shell via coaxial LPNE.....	82
4.2 Characterization.....	86
4.3 Preliminary devices.....	96
4.4 Routes to improve device efficiency.....	105
<b>Bibliography</b>	<b>119</b>

# List of Figures

Figure 1.1- Solar electricity cost as a function of device efficiency and cost. Three theoretical efficiency limits are shown: Shockley-Queisser limit for a single junction solar device; the second-law thermodynamic limit of 1 Sun concentration; and the second-law thermodynamic limit for any Earth-based solar-to-electric system. The dashed lines give imagery of the cost per watt.....6

Figure 1.2- Proposed band diagram for the solar cell fabricated in this work.....9

Figure 1.3- A depiction of multiple internal reflections generating a leaky-mode in a semiconducting nanowire with radius,  $r$ .....11

Figure 1.3. Photocurrent enhancement and optical resonances in rectangular nanowire arrays on glass. (a) Calculated photocurrent density  $J_{sc}$  of an array of 130 nm wide square nanowires as a function of the nanowire separation. The left-side vertical axis indicates the photocurrent normalized to that of a continuous film (zero separation). Inset, schematic illustration of the array structure. A 25% enhancement while utilizing half of the material compared to thin film analogue results in a 250% efficiency increase per unit volume (b) Calculated dependence of the photocurrent density  $J_{sc}$  on the illumination angle for the array with various spacings (50, 130 and 260 nm) and a 130 nm thick film. (c) Calculated absorption spectra of a 130 nm wide square nanowire in the array with different separations of 30 and 130 nm. Take note that the 130 nm pitch is optimal pitch, and that smaller pitch does not necessarily correlate to more efficient absorption; the 30 nm pitch has less efficient absorption than an individual wire itself.....13

Figure 1.4- Generality of the photocurrent enhancement: (upper) short circuit photocurrent density  $J_{sc}$  in nanowires of other major photovoltaic materials, including CuInGaSe, Ge, CdTe, amorphous Si, and GaAs, and (lower) photocurrent enhancement in the nanowires compared to their bulk counterparts.....15

Figure 1.5- Generality of the optical resonance and short-circuit current enhancement to one-dimensional nanostructures: (a) Simulated short-circuit current density for one dimensional a-Si structures of rectangular, circular,

hexagonal, and triangular cross section as a function of size. The red arrow in the inset shows illustrates the illumination geometry used in Cao's calculations. (b) Simulated absorption spectra of these one dimensional a-Si structures. Note the small variation in peak absorption which is believed to exist simply as a matter of volume change.....16

Figure 1.6- Illustrating classic optical absorption in a thin film solar cell; An AM1.5 filter solar spectrum, together with a graph that indicates the solar energy absorbed by a standard 2 $\mu$ m-thick Si film. It is clear that a large fraction of incident light in the spectral range of 600-1100 nm is not absorbed in a thin film solar cell.....17

Figure 1.7- Plasmonic light-trapping geometries for thin-film solar cells: (a) Light trapping by scattering from metal nanoparticles at the surface of the solar cell. Light is preferentially scattered and trapped into the semiconductor thin film by multiple and high-angle scattering, causing an increase in the effective optical path length in the cell. (b) Light trapping by the excitation of localized surface plasmons in metal nanoparticles embedded in the semiconductor. The excited particles' near-field causes the creation of electron-hole pairs in the semiconductor. (c) Light trapping by the excitation of surface plasmon polaritons at the metal/semiconductor interface. A corrugated metal back surface couples light to surface plasmon polariton or photonic modes that propagate in the plane of the semiconductor layer.....19

Figure 1.8- Electrical measurements of solar cells containing a plasmonic grating like that shown in Figure 1.7, revealing that when comparing the flat structure with no grating, to the two structures with 500 and 700 nm pitch, the pitched systems lead to an enhanced short-circuit current.....20

Figure 1.9- Results from measuring external quantum efficiency (EQE) spectra of flat, nanopatterned (500 and 700 nm pitch) and randomly structured cells (Asahi). The primary enhancement in photocurrent over the flat reference occurs from 550-800 nm; the range where the standard thin film has low absorption efficiency as displayed from Figure 1.6.....21

Figure 2.1- MEG in a quantum dot. A photon with energy  $E_{ph}$  excites an electron to a higher energy level (red arrow), leaving behind a positively-charged hole. This electron and hole form an exciton that then relaxes to a lower energy level, and at the same time a second electron is excited to a higher energy level (green arrows). As a result, a single photon creates two



excitons. Horizontal blue lines represent quantum dot energy levels; and black lines represent potential barriers.....25

Figure 2.2- The calculated density of states of lead sulfide for (from top to bottom) an 8-atom, 32-atom, 56-atom, and 88-atom cluster [70].....27

Figure 2.3- 'New' ultimate photovoltaic conversion efficiency (red) of 65% at 0.3 eV compared to the previous 44% at 1.2 eV (black).....29

Figure 2.4- Process flow diagram for traditional LPNE method devised by the Penner group as a new method of nanowire fabrication.....31

Figure 2.5- Optical microscope image taken under 50x, with relative scale bar of 5  $\mu\text{m}$  shown, illustrating lithography with no line edge variation; acceptable photolithography and development to proceed with next step in LPNE method.....33

Figure 2.6- Control of LPNE trench and associated cross section image. (a) Trench width as a dependency of etching time, where longer etching time results in a wider trench- this will become important in chapter 3. (b) Cross-section scanning electron micrograph displaying the trench adjacent to the nickel edge, both layers sitting on top of the glass, but beneath the structurally stable photoresist.....34

Figure 2.7- a-c) Cyclic voltammograms ( $20 \text{ mV s}^{-1}$ ) for solutions containing a) lead ( $[\text{Pb}^{2+}] = 10 \text{ mM}$ ) with  $0.1 \text{ M}$  EDTA at  $\text{pH} = 4$  in aqueous solution, b) selenium ( $[\text{HSeO}_3^-] = 1 \text{ mM}$ ) with  $0.1 \text{ M}$  EDTA at  $\text{pH} = 4$  in aqueous solution, and c) lead and selenium ( $[\text{Pb}^{2+}] = 10 \text{ mM}$ ,  $[\text{HSeO}_3^-] = 1 \text{ mM}$ ) with  $0.1 \text{ M}$  EDTA at  $\text{pH} = 4$  in aqueous solution. Voltammetric waves are assigned to the following reactions: Wave (i),  $\text{Pb}^{2+} + 2 \text{ e}^- \rightarrow \text{Pb}^0$ ; Wave (ii),  $\text{HSeO}_3^- + 5 \text{ H}^+ + 4 \text{ e}^- \rightarrow \text{Se}^0 + 3 \text{ H}_2\text{O}$ ; Wave (iii),  $2 \text{ H}_3\text{O}^+ + 2 \text{ e}^- \rightarrow \text{H}_2 + 2 \text{ H}_2\text{O}$ ; Wave (iv),  $\text{Se}^0 + 3 \text{ H}_2\text{O} \rightarrow \text{HSeO}_3^- + 5 \text{ H}^+ + 4 \text{ e}^-$ ; Wave (v),  $\text{Pb}^{2+} + \text{HSeO}_3^- + 5 \text{ H}^+ + 6 \text{ e}^- \rightarrow \text{PbSe} + 3 \text{ H}_2\text{O}$ ; Wave (vi),  $\text{PbSe} + 3 \text{ H}_2\text{O} \rightarrow \text{Pb}^{2+} + \text{HSeO}_3^- + 5 \text{ H}^+ + 6 \text{ e}^-$ .....35

Figure 2.8. An optical micrograph of a parallel array of PbSe nanowires after completion of the entire LPNE process flow.....36

Figure 2.9- Low magnification SEM image showing an array of parallel PbSe nanowires with  $5 \mu\text{m}$  separation (scale bar =  $50 \mu\text{m}$ ).....37

Figure 2.10- Both the height and width of a nanowire produced by LPNE can be independently controlled. (a) Nanowire height measured by atomic force microscopy (AFM) versus the thickness of evaporative layer. (b) Nanowire

width measured by SEM <i>versus</i> electrodeposition duration; from reference 53.....	39
Figure 2.11- Calibration curve of PbSe nanowire width as a function of electrodeposition duration.....	40
Figure 2.12- High magnification SEM image of a single PbSe nanowire depicting the protrusions opposite of the nickel edge (scale bar= 500 nm).....	41
Figure 2.13- EDX spectra of a single PbSe nanowire showing the presence of lead and selenium with a measured atomic ratio nearly 50:50.....	42
Figure 2.14- X-ray diffraction patterns from an array of 500 nm wide PbSe nanowires (black) compared to a reference pattern for cubic PbSe (JCPDS 06-0354).....	43
Figure 2.15- A SEM image of a 50um x 50um support film at the center of a silicon nitride TEM grid (provided by Ted Pella).....	45
Figure 2.16- Illustrating growth of LPNE nanowires on TEM grid. (a) From left to right; Alligator clip from potentiostat, Ag paste connecting alligator clip to the TEM grid. (b) Immersion of substrate containing the TEM grid into a three electrode electrochemical cell that is ready to electrodeposit.....	46
Figure 2.17- TEM image of a single nanowire showing grain sizes ranging from 20-100 nm (scale bar = 50 nm).....	47
Figure 2.18- Selected area electron diffraction of the nanowire from Figure 2.17 with the inner five rings indexed to cubic PbSe (JCPDS 06-0354).....	48
Figure 2.19- Comparison of Raman spectra for a PbSe quantum dot film measured in air (red) and measured in an airtight cell (black). The asterisk marks the position of the silicon film used as a background correction.....	49
Figure 2.20- Raman spectra of air exposed PbSe nanowires prepared by LPNE.....	50
Figure 2.21- A SEM image of a PbSe nanowire created by LPNE with a width of approximately 30 nm.....	52
Figure 2.22- Comparison of PbSe nanowire width with varying nickel film thickness. The thicker nickel film leads to an increased rate of deposition.....	53
Figure 2.23- SEM image of a single PbSe nanowire with two nickel contacts.....	54

Figure 2.24- Large bias I-V curve of a single 40 nm (h) x 158 nm (w) x 63  $\mu$ m (l) PbSe nanowire displaying diode like behavior.....55

Figure 2.25- Small bias I-V curves of a single PbSe nanowire with dimensions of 40 nm (h) x 158 nm (w) x 64  $\mu$ m (l) (blue circles), 40 nm(h) x 395 nm (w) x 68.5  $\mu$ m(l) (green squares), 80nm(h) x 486 nm (w) x 138  $\mu$ m (l) (red diamonds), and 80 nm (h) x 574 nm (w) x 98.5  $\mu$ m (l) (black crosses).....56

Figure 3.1- Schematic of HDLPNE process flow.....60

Figure 3.2- CV in nickel electroplating solution where gold nanobands act at the working electrode.....63

Figure 3.3- An SEM image of initial HDLPNE results using a nickel reduction potential of -0.7 V vs Ag/AgCl.....64

Figure 3.4- Winding Au nanowire array resulting from increasing the deposition potential of Ni from -0.70V to -1.0V.....66

Figure 3.5- Well defined 200 nm Au nanowire edges with a well defined pitch of 100 nm.....68

FIGURE 3.6- The ability to create a variety of pitch and nanowire width using HDLPNE. (a) Two 100-nm Au nanowires with pitch of 75 nm. (b) Three-100 nm Au nanowires with pitch of 100 nm. (c) Four-75 nm Au nanowires with pitch of 250 nm. (d) Five-100 nm Au nanowires with pitch of 100 nm.....69

Figure 3.7- Functional relationships resulting from HDLPNE. (a) Dependence of gold nanowire width on gold electrodeposition time. (b) Dependence of gold nanowire spacing or pitch on nickel electrodeposition time.....70

Figure 3.8- High resolution SEM image of two gold nanowires with approximately 60 nm in width separated by an average of 40 nm.....71

Figure 3.9- Low resolution SEM image showing the ability to adapt HDLPNE to create a plasmonic lens type structure.....72

Figure 3.10- The ability to create nanowire width and pitch independent of one another in the same array. (a) Two gold nanowires approximately 500 nm apart, with widths of 200 (left) and 100 nm (right). (b) An array of three gold nanowires with widths of 80 (left), 120 (center), and 170 nm (right) separated by 350 nm (left to center) and 750 nm (center to right).....73

Figure 3.11- Consistent pitch from top-to-bottom (a) Low-magnification SEM image displaying 13 high density Au nanowire arrays. (b-d) High-magnification SEM images along 1 array exhibiting excellent pitch control over long array lengths.....74

Figure 3.12- Side-by-side comparison of nanowire width and pitch. (a) Low-magnification SEM image displaying 18 high density gold nanowire arrays. (b) Low-magnification SEM image displaying 8 high density gold nanowire arrays. (c) SEM image displaying 3 high density gold nanowire arrays which have pitch comparable to adjacent high density arrays.....75

Figure 3.13- Current-versus-voltage curve for a high-density 3 wire array, with a resistance of 51.6 k $\Omega$  and a resistivity of  $1.3 \times 10^4 \Omega \text{ cm}$ .....77

Figure 3.14- left; AFM image of 4 gold nanowires, right; Linescan across 4 nanowires shown in left image.....78

Figure 3.15- TEM analysis on HDLPNE nanowires. (a) TEM image after electrodeposition of 1 gold nanowire followed by 1 nickel spacer. Inset- SAED showing nanocrystalline nature and lack of alloying after gold and nickel deposition. (b) TEM image of two 50 nm wide gold nanowires with pitch of 200 nm.....79

Figure 4.1- The coaxial LPNE process flow to create a core-shell structure.....83

Figure 4.2- CV of the PbSe electrodeposition with gold nanowires acting as the working electrode.....84

Figure 4.3- SEM image showing a 100 nm gold nanowire with a 200 nm PbSe shell; created by using coaxial LPNE.....85

Figure 4.4- EDX spectra of a PbSe-coated gold nanowire showing the presence of both lead and selenium.....86

Figure 4.5- XRD spectrum of a PbSe-coated gold nanowire with the 111, 200 peaks of gold (red labels) and the 112, 200, and 220 peaks of PbSe (black labels) identified.....87

Figure 4.6- SAED image of a PbSe-coated gold nanowire with the 200, and 222 peaks of gold (yellow text) and the 222, 113, and 220 peaks of PbSe labeled (black text).....88

Figure 4.7- TEM image of a PbSe-coated gold nanowire.....	89
Figure 4.8- Calibration curve relating the PbSe shell thickness to electrodeposition time and the gold nanowire width.....	91
Figure 4.9- Light (green) and dark (black) IV curves of an array of 40 x 100 nm gold nanowires coated with 250 nm of PbSe.....	92
Figure 4.10- Experimental setup to test for coaxial nanowire ability to respond to an on-off input signal at a frequency determined by the optical chopper. The blue signal in the oscilloscope refers to the chopper frequency and the red signal in the oscilloscope corresponds to the nanowire signal.....	94
Figure 4.11- The photocurrent through an array of 40 x 100 nm gold nanowires coated with 250 nm of PbSe chopped at 50 Hz.....	95
Figure 4.12- Proposed solar cell structure where pitch, and therefore device density, is determined by photolithography.....	98
Figure 4.13- Solar cell curve for a solar cell based on using coaxial LPNE where the pitch is determined by photolithography; $FF = 0.274$ , $V_{oc} = 0.275$ V, $J_{sc} = 4.26$ $\mu$ A.....	99
Figure 4.14- Proposed solar cell structure where pitch, and therefore device density, is determined by electrodeposition by using HDLPNE.....	100
Figure 4.15- HD-Coaxial nanowire array for solar cell. (a) Low resolution SEM image showing the consistency of the PbSe on the gold core. (b) High resolution image showing the increased crystallinity and smooth deposit of 250 nm Pbse on the 100 nm gold cores.....	101
Figure 4.16- Solar cell curve for a solar cell based on using HD and coaxial LPNE in conjunction with one another; $FF = 0.278$ , $V_{oc} = 0.279$ V, $J_{sc} = 40.15$ $\mu$ A.....	102
Figure 4.17- CV on nickel substrates provided to Stickney's group to determine optimal UPD of Te.....	109
Figure 4.18- CV on nickel substrates provided to Stickney's group to determine optimal UPD of Cd.....	110
Figure 4.19- CdTe nanowire array prepared by alternating UPD of Cd-Te on LPNE substrates.....	111
Figure 4.20- EPMA of CdTe nanowires by UPD on LPNE substrates.....	112

Figure 4.21- Light (green) and dark (black) IV curves of an array UPD CdTe nanowires prepared by Stickney's group.....	113
Figure 4.22- Experimental setup to measure optical absorption of nanowire arrays.....	116
Figure 4.23- Absorption spectra of nanowire array using experimental setup in Figure 4.22.....	117

## List of Tables

Table 2.1- Average grain size from Scherrer Analysis.....	44
---	----

Table 2.2- Comparison of Electrical Resistivity for PbSe Nanowires with Different Aspect Ratios.....	57
--	----

Table 4.1- Comparison of current density, Voc, and FF by varying device structure.....	103
--	-----

## Acknowledgements

As this work is a culmination of years of my professional work, I want to acknowledge individuals in order as it relates to my ability to produce this dissertation. I would first like to acknowledge individuals who assisted me in deciding to attend graduate school. I first need to give credit to God for graciously allowing me to survive a life threatening brain hemorrhage at the age of 16. This experience bestowed upon me the desire to live up to my potential and I believe this dissertation is an example of this potential. I would next like to thank my undergraduate research adviser, Dr. David Saiki who encouraged me to attend graduate school. Secondly I would like to thank my wife Jessica for encouraging me to not accept job offers I had coming out of my undergraduate studies, but instead push myself for an advanced degree. Once deciding to pursue my PhD, I need to thank Professor David Kelley for calling me to inquire if I had any interest in attending UC Merced. I had already accepted an offer from UC Davis without considering UC Merced, and without that call, would most likely not be at the point I am today. Once on campus at UC Merced I need to graciously acknowledge Professor Erik Menke for allowing me to be his first graduate student. At first being a member of Professor Menke's group was tough; Erik wanting me to become independent from the beginning presented a problem as I was not use to this. However after spending the last few years in his group presents the realization that his leadership style is short of brilliance. I would also like to acknowledge Professor Reginald Penner, Dr. Sheng-Cheng Kung, and Dr. David Taggart from UC Irvine for allowing me to visit their group and teach me the basics of the LPNE method. Specifically Dr. Sheng-Cheng Kung spent extra time to help me when I was struggling- I remember the last Sunday of my stay at UCI, Dr. Kung came in willing on his own to run a XRD on PbSe nanowires. Had he



not taken the time out of his weekend to help me, this dissertation may have had an entirely different topic. Next I would like to thank Somnath Ghosh for joining the Menke group in the summer of 2009. Somnath has not only taught me too much about academics and life to put in this short section, but also has become a good friend that I can trust. The same can be said of another member that joined the Menke lab in 2009, Luke Reed. I would like to thank the undergraduate students that have been an integral part of my lab, Alan Sargisian, Arnold Barreras, and Ibrahim Yusufu. Specifically I would like to acknowledge Alan for his assistance getting our lab fully developed and assisting in some of my initial work on my PbSe and high density projects to the point where he has been named a contributing author. Acknowledgement is also due to my colleagues at Western Digital who allowed me to join their integration team for a summer to fully cement in my mind that I want to pursue an industrial career. I would lastly like to thank my son Joel for the inspiration he has given me and the joy he brings to my life. There are many more acknowledgements that could be made, but the truth is that would take up too much time and space. My educational training has been a long journey that has required assistance at all points, while none not necessarily more important than the rest, still all necessary to get where I am now. I want to conclude by saying I am sincerely and graciously thank you to all who have taken time to aid me with this journey.

# Curriculum Vitae

Justin Hujdic

2008	B.S. in Chemistry, Magna cum Laude California State University Stanislaus
2004-2005	Biogas Intern Del Monte Foods, Modesto, Ca
2011	Process Integration Engineer Intern Western Digital, Fremont, Ca
2012	PhD in Chemistry University of California, Merced Dissertation: Lead selenide nanowire solar cells via LPNE and its new found derivatives Professor Erik J. Menke, Adviser

## Publications

Ghosh S., Hujdic J., Menke E., *Journal of Physical Chemistry C*, **2011**, 115, p 17670-17675.

Hujdic J., Sargisian A., Shao J., Ye T., Menke E., *Nanoscale*, **2011**, 3 , p 2697-2699.

Hujdic J., Taggart D., Kung S., Menke E., *Journal of Physical Chemistry C*, **2010**, 7, p 1055-1059.

# **Abstract of the Dissertation**

Lead selenide nanowire solar cells via LPNE and its  
new found derivatives

by

Justin Hujdic

Doctor of Philosophy in Chemistry

University of California, Merced, 2012

Professor Erik J. Menke, Adviser

Solar energy has yet to break into the mainstream market mainly due to its elevated cost relative to its competitors. I introduce the ability to use lithographically patterned nanowire electrodeposition (LPNE), a cost-effective nanowire growth method developed by the Penner group in 2006, to fabricate PbSe nanowires as a base for solar cells. I then transition into demonstrating how LPNE can be amended to permit for high density nanowire fabrication on the order of 50 nm pitch, resulting in a significantly larger device density compared to traditional LPNE. Next, I will illustrate successful fabrication of solar cells based on PbSe and how high density LPNE has shown the potential ability to increase the efficiency of the device due to nanoscale phenomena. I conclude with two systematic routes for future improvement to the device which are already underway. Consequently there exists the potential that an improved solar cell

based on these methods could compete as a cost-effective energy source.

# **Chapter 1**

## **Cost-effective solar energy using nanowires**

### **1.1 Objectives of the Dissertation**

This dissertation has four main parts. The first of these is the introduction, where I give a brief motivation for investigating a carbon neutral energy source which can serve the exponentially increasing worldwide energy demand via fabrication of a cost effective solar cell. This solar cell should be designed and produced in such a way that it allows for a reduction in material and processing costs while simultaneously attempting to maintain reasonable efficiencies through various light trapping and efficiency enhancement phenomena at the nanoscale. The second part is an in depth overview of the how and why I fabricated lead selenide nanowires as the semiconductor for my solar cell using lithographically patterned nanowire electrodeposition (LPNE). The third part of the dissertation investigates how to improve the density of nanowires created by LPNE, typically limited by photolithography, to not only beat the limits of photolithography, but introduce dimensions that can potentially enhance the efficiency of a solar cell fabricated via this technique. The final portion of the

dissertation illustrates initial results of single nanowire PbSe solar cells constructed via a new found derivative of LPNE, coaxial LPNE, and compares these results to high density coaxial PbSe nanowire solar cells. The final portion of this work is highlighted with two potential areas for future investigation.

## **1.2. Motivation for a cost effective solar energy source**

Just 10 years ago the entire worldwide energy consumption was  $4.25 \times 10^{20}$  J, equating to 13.5 TW [1]. Of power consumption 86% was obtained from fossil fuel sources with an equal distribution between oil, coal, and natural gas. Approximately 6% of the total energy used originated from nuclear power, and the remainder of energy demand was met by 'other' sources. Renewable energy provided for an exceptionally small portion of this energy demand, with only a fraction deriving from solar sources [2]. In the next 50 years alone the US Department of Energy (DOE) expects worldwide power consumption to double to over 27TW, and by 2100 to be approximately 50 TW [3]. Therefore a road needs to be chosen wisely as to how to meet this growing demand over the both the near and long term.

If the world continues on its traditional path, it is supported by 1998 consumption rates that there is enough oil, coal, and natural gas resources available at an annual rate of consumption between 25-30 TW to meet

energy demand for nearly seven centuries [4]. However consuming fossil fuels at this rate will present a significant global problem- If the intensity of carbon emissions were to remain constant, the world carbon emission rate would still increase from 6.6 billion metric tons (GtC)  $\text{yr}^{-1}$  to 13.5 GtC  $\text{yr}^{-1}$  by 2050. However because of significant research and development into making traditional energy sources more carbon efficient, the global carbon emission rate is expected to be reduced to 11.0 GtC  $\text{yr}^{-1}$  by 2050 [1]. While this reduction in  $\text{CO}_2$  emissions is a step in the right direction, historical data cannot be argued as to the possible effects of such emissions; data from different ice cores have shown an ever increasing  $\text{CO}_2$  concentration over a time period which correlates to ice ages on Earth [5]. However the increase in  $\text{CO}_2$  concentration in the ice cores cannot be identified as a direct cause of the ice ages, it is a prime suspect due to correlation, and therefore attempts at reducing  $\text{CO}_2$  emissions are being addressed by researching plausible carbon neutral energy sources [6, 7].

There are virtually three paths that can be taken to produce carbon neutral energy and at the same time meet the ever increasing worldwide energy demand. One process that could be taken to meet demand would be nuclear fission [8]. While this is likely the most plausible option, because nuclear energy is already being created and used worldwide with high efficiencies, the main problem with this energy source is the extensive

construction timeline associated with building the magnitude of nuclear power plants necessary to meet the energy demand of the next 50-100 years [1]. On top of this, the recent Japanese tsunami of 2011 has brought attention to the possible offsets of any benefit nuclear power could provide to the environment. A second path to carbon neutral power would be to actually capture and store the emitted carbon from fossil fuels in underground reservoirs. However extensive results on long term studies are still not yet available. In addition results from one carbon storing reservoir will not necessarily give confidence as to the function of other reservoirs based on obvious geographical differences in potential storage locales [9]. Needless to say, these two aforementioned methods of carbon neutral energy production may possess promise for the future, but no immediate confidence can be assured that they will meet energy demand due to the associated remaining challenges.

The lack of confidence in the first two paths to immediately address the increase in energy demand leads to the third and final path to producing carbon neutral power- the use of renewable energy. The largest renewable resource presently available is the sun;  $4.3 \times 10^{20}$  J of energy in the form of sunlight strike the earth every hour [4]. This amount of energy would have been sufficient to provide for the entire world energy demand in 2001 ( $4.1 \times 10^{20}$  J). In spite of this fact, less than 0.1% of electricity is delivered to



the consumer in the form of solar energy. Aligned with the increasing energy demands of the future and the prospective for that demand to be met by carbon neutral sources, coupled with the fact that the potential of solar energy has been, for the most part, not exploited, solar energy sources provide an excellent carbon neutral electricity source and therefore, will be the chosen topic of this work.

To successfully turn the sun's energy into usable electrical energy requires the ability to first capture light, then to convert light energy into usable electrical energy, and finally store the energy efficiently; the storage of solar energy is a separate area of intense research and will not be addressed in this work. My main focus will be on capturing light and converting light into usable energy. The capture and conversion of sunlight can be performed by commercial solar devices at efficiencies between 15 and 20% at an average cost of \$300 m<sup>-2</sup> [1]. Coupling in the balance of systems cost (BOS)- the costs associated with installation and startup- and a 30 year lifetime, the average cost of solar energy is between \$0.25 and \$0.30 per kilowatt-hour (kWh) to recover the cost associated with the initial purchase [10,11]. Compare this to the average cost of electricity the consumer pays to their utilities of \$0.05-\$0.10 kWh, and it is apparent that there needs to be a decrease in the cost of solar energy to make this energy option more attractive to the consumer. The potential improvements related

to reducing the cost can be addressed by cutting the cost to create the device, improving the efficiency of solar cells, or both. Figure 1.1 illustrates the average cost per watt as a function of the efficiency of the device against the cost of production; a practical conversion for this figure is \$1/W equates to \$0.05/kWh over the lifetime of a 30 year working solar device.

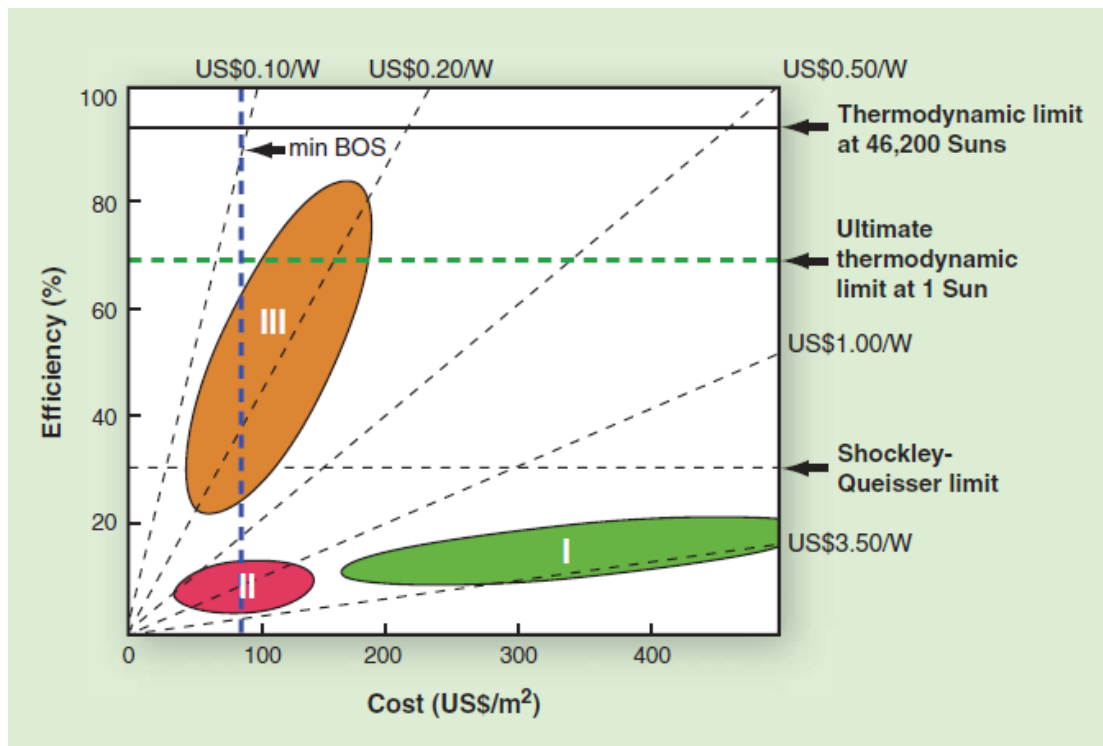


**Figure 1.1-** Solar electricity cost as a function of device efficiency and cost. Three theoretical efficiency limits are shown: Shockley-Queisser limit for a single junction solar device; the second-law thermodynamic limit of 1 Sun concentration; and the second-law thermodynamic limit for any Earth-based solar-to-electric system. The different generation of cells can be described as follows; I, green, corresponds to first generation solar technology based on thick silicon cells, II, pink, corresponds to second generation thin semiconductor film based cells, and III, orange, corresponds to third generation cells based on nanowires, quantum dots and organics but these are still in the research phase. The dashed lines give imagery of the cost per watt. [12]

My work on solar cells will aim to bring light to an approach which can maintain respectable efficiency with a simultaneous effort to reduce the cost of production of the associated device. To keep the efficiency reasonable I first looked into historical reports on solar efficiencies and found that Shockley and Queisser (S&Q) calculated the theoretical efficiency limit of a single junction photovoltaic to be 31% [13]. However since this initial report dating to 1961, there has been extensive research into ways in which this theoretical efficiency can be improved. In the work of S&Q, one key element of their limit was that all energy absorbed in excess of the band gap ( $E_g$ ) will be lost through thermal relaxation. This provided a route by which researchers have discovered routes to acquire this lost energy via the creation of multiple excitons that were once restricted by the S&Q limit [14-20]. If this were possible, it would in turn create a higher efficiency and therefore lower the cost. I will discuss my research into creating multiple excitons in further detail in Chapter 2 of this work.

While most researchers agree the efficiency of solar energy cannot be improved dramatically outside of research presently being performed at the university level, most do believe the cost of producing a device can be reduced considerably. Most commercial solar modules are based on first generation devices (Green section, I, in Figure 1.1) consisting of a thick silicon film. The silicon film, on the order of 100-200  $\mu\text{m}$  or more, calls for a hefty material

cost on top of the intensive processing costs associated with this great amount of silicon. This has led to the second generation solar cell (Pink section, II, in Figure 1.1), based on thin film silicon or other materials such as CdTe, Copper Indium Diselenide (CIS), etc. The second generation devices require less semiconducting material and therefore reduce the material cost and subsequently the associated manufacturing costs while maintaining reasonable efficiency.

Still not satisfied with the first and second generation modules, research is being investigated into what is being called the third generation solar cell (Orange section, III, in Figure 1.1). Though not yet commercially available, Figure 1.1 illustrates that these devices have the potential to cost as little as \$0.01 kWh over a 30 year lifetime making them much cheaper than the average electricity cost and potentially can serve as a new mainstream energy source. One type of solar cell in this third generation technology that has shown promise is the nanowire. Nanowires have been shown to drastically reduce the amount of necessary material to fabricate a solar cell leaving them as a competitive option for reducing material and production cost while simultaneously keeping the efficiency respectable [21-25]. Therefore, the main goal of my work will be to fabricate an efficient nanowire based solar cell that drastically reduces production and material cost.

### 1.3. Leaky-Mode Resonance (LMR) in semiconductors to enhance device efficiency

Figure 1.2 displays the proposed band diagram for the solar cell that will be discussed in chapter 4. In addition Figure 1.2 illustrates the elementary operation of a solar device; as light is captured in the semiconductor portion of the cell, an electron-hole pair (e-h) is created, separated, and used as electrical current in a resistor. After being utilized across the resistor the e-h recombine and the process begins anew.

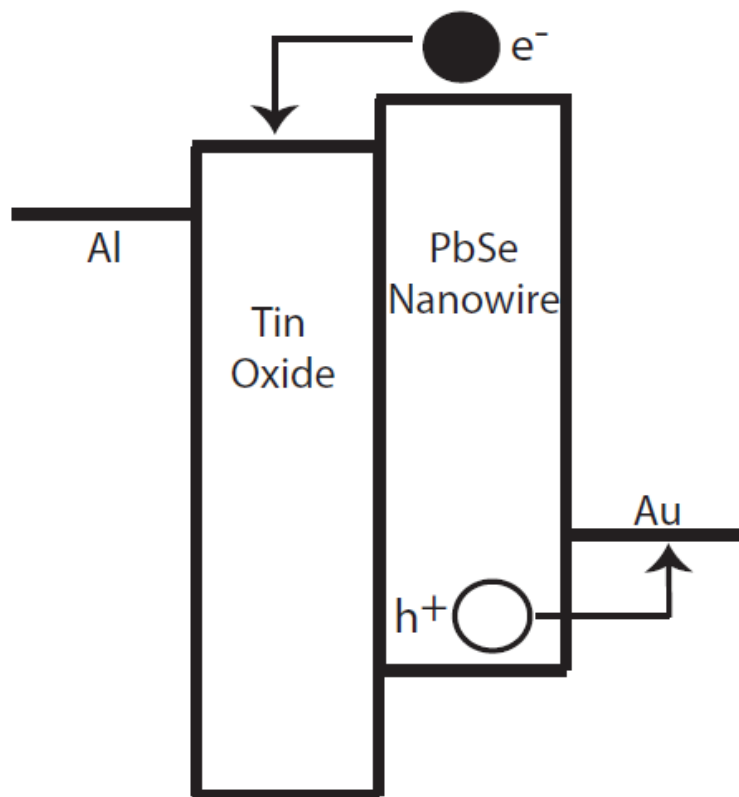


**Figure 1.2-** Proposed band diagram for the solar cell fabricated in this work.

The efficiency of a solar cell,  $\eta$ , like that shown in Figure 1.2 is described by the following equation,

$$\eta = J_{sc} * V_{oc} * FF / P_{in}$$

Where  $J_{sc}$  is the short-circuit current,  $V_{oc}$  is the open-circuit voltage,  $P_{in}$  is the input power while testing the efficiency, and FF is the fill factor which is governed by the equation:

$$FF = J_{sc,mp} * V_{oc,mp} / (J_{sc} * V_{oc})$$

The fill factor equation refers to the  $J_{sc}$  at maximum power and  $V_{oc}$  at maximum power as  $J_{sc,mp}$  and  $V_{oc,mp}$  respectively.

Individual attention to improving  $J_{sc}$ ,  $V_{oc}$ , and FF could be the topic of an entire dissertation per variable, so I will reserve my focus solely on the effects of  $J_{sc}$ . A main factor in controlling the  $J_{sc}$  is the varying thickness of the absorber, where a thick absorbing layer will absorb a large amount of light leading to a larger  $J_{sc}$  and higher efficiency, up to a point, and a cheaper cost-per watt compared to a thin device which lacks the necessary thickness for proper light absorption. However this limited light absorption in thin devices has led to a new field of study known as photon management (PM) which attempts to 'trap' light in a thin solar cell. By trapping the light in the thin cell it is theorized a higher ratio of e-h could be produced per absorbed photon per unit area compared to the thicker cell. PM therefore

has the potential to provide a thin cell a  $J_{sc}$  per unit area comparable to a thick device. Because there is a desire to reduce the material cost, researchers favor the thin devices and therefore extensive research has gone into PM in thin nanowire solar cells to hopefully absorb light on the scale of the thicker devices while still reducing the material necessary for operation and thereby reducing production cost [26-32].

Specifically Linyou Cao has discovered what he terms leaky-mode resonance (LMR) in semiconducting nanowires, a new field of investigation for effective PM. A function of the nanowire radius, index of refraction, and incident wavelength, LMRs trap light in circulating orbits via multiple internal reflections in semiconducting nanowires, beginning to resemble resonant cavities, acting in a manner like the illustration in Figure 1.3 [33-37].

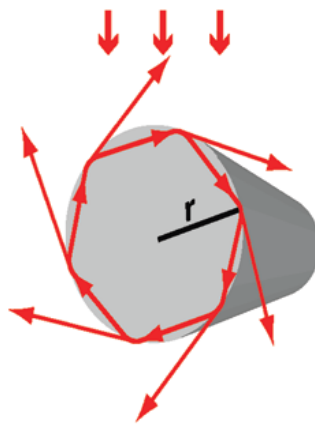


**Figure 1.3-** A depiction of multiple internal reflections generating a leaky-mode in a semiconducting nanowire with radius,  $r$ . [34]

These multiple internal reflections have been shown to increase the absorption efficiency of incident light in semiconducting nanowires [35]. Linyou Cao went on to show that when investigating amorphous silicon (a-Si) nanowires with specific dimensions, there was an optimum distance between adjacent nanowires, or pitch, of 130nm. Figure 1.3c shows that as the pitch was reduced below the 130nm optimum pitch to a 30 nm pitch, deconstructive interference of the leaky-modes occurs resulting in a decrease in light absorption compared to an individual nanowire, illustrating that there was in fact an optimum pitch for maximum absorption [33, 36]. After determining the optimum pitch for maximizing absorption in the a-Si nanowires, Cao proceeded to determine how this would affect a solar cell. He ran models to show that the 130nm pitch between adjacent 130x130nm nanowires resulted in a photocurrent enhancement of 25% when compared to the thin film analogue- seen in Figure 1.3a. The 25% enhancement coupled with the fact that half of the material is used in the pitched system compared to thin film version leads to an efficiency enhancement per unit volume of 250%.



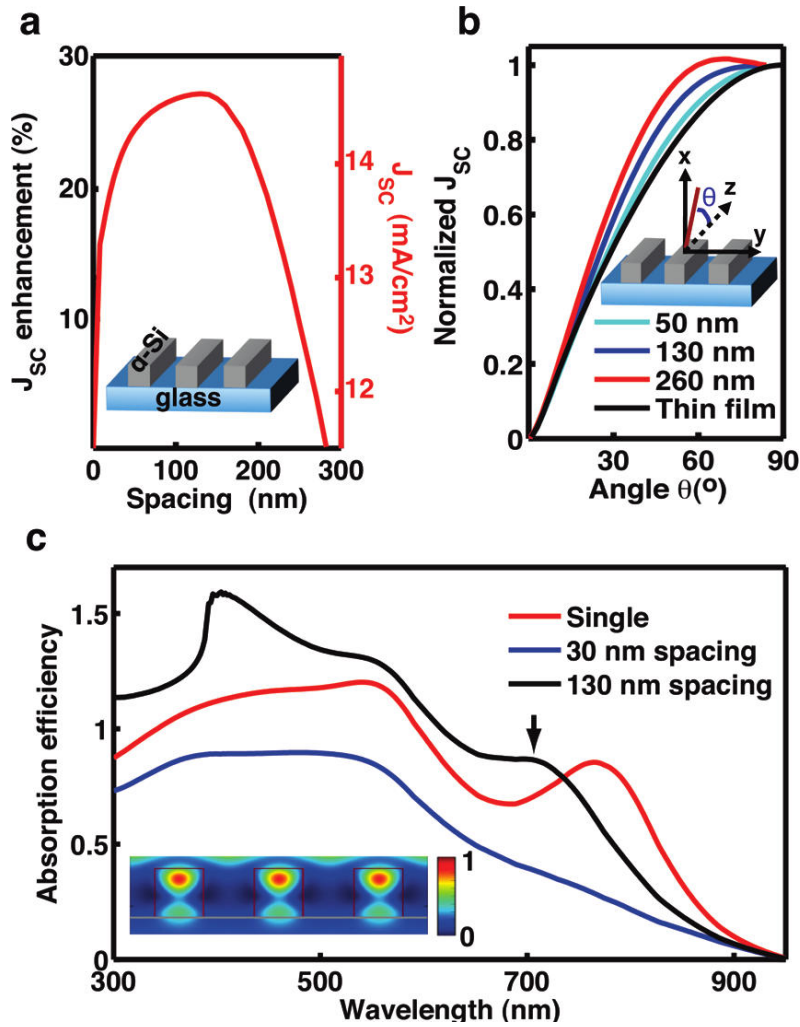


**Figure 1.3.** Photocurrent enhancement and optical resonances in rectangular nanowire arrays on glass. (a) Calculated photocurrent density  $J_{sc}$  of an array of 130 nm wide square nanowires as a function of the nanowire separation. The left-side vertical axis indicates the photocurrent normalized to that of a continuous film (zero separation). Inset, schematic illustration of the array structure. A 25% enhancement while utilizing half of the material compared to thin film analogue results in a 250% efficiency increase per unit volume (b) Calculated dependence of the photocurrent density  $J_{sc}$  on the illumination angle for the array with various spacings (50, 130 and 260 nm) and a 130 nm thick film. (c) Calculated absorption spectra of a 130 nm wide square nanowire in the array with different separations of 30 and 130 nm. Take note that the 130 nm pitch is optimal pitch, and that smaller pitch does not necessarily correlate to more efficient absorption; the 30 nm pitch has less efficient absorption than an individual wire itself [36].

Most large scale solar panels require solar trackers which change the incident angle of light throughout the day to maintain operating efficiency by maximizing the number of input photons from the sun as the sun tracks across the atmosphere. However according to Linyou Cao's results shown in Figure 1.3b, the leaky-modes in the a-Si nanowires are less dependent on incident photon angle when compared to a thin film analogue. This leads to the idea that there can even be a potential decrease in the minimum BOS of a solar cell system if LMRs can be taken advantage of thereby further reducing the overall cost.

However all in-depth study up to this point performed by Cao was solely on circular a-Si nanowires. It would therefore be beneficial to determine if the advantages of LMRs could be realized independent of both material and shape. As displayed in Figure 1.4, Cao went on to show that LMRs do in fact occur in different materials, though at different rates, still enhance the short-circuit current.

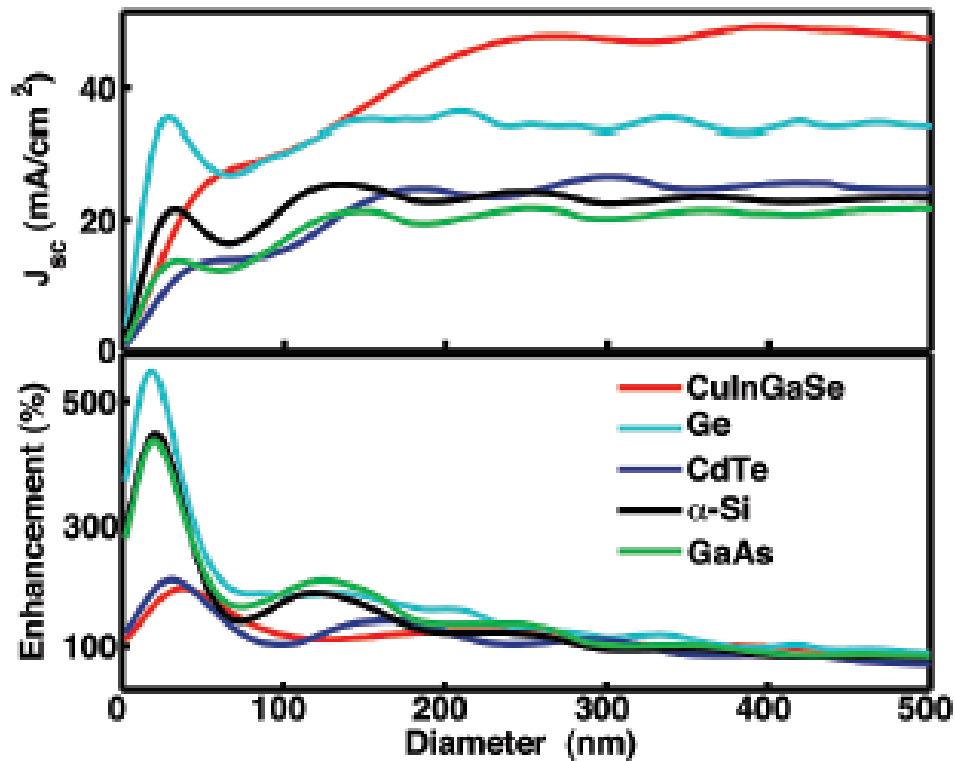


**Figure 1.4-** Generality of the photocurrent enhancement: (upper) short circuit photocurrent density  $J_{sc}$  in nanowires of other major photovoltaic materials, including CuInGaSe, Ge, CdTe, amorphous Si, and GaAs, and (lower) photocurrent enhancement in the nanowires compared to their bulk counterparts [36].

In addition to proving LMRs are independent of material, Cao showed that the shape of the semiconducting nanowire has a minimal effect on the LMR efficiency- displayed in Figure 1.5a. It is believed that the efficiency difference results from the change in volume as the shape changes. This small difference can be further accounted for by the relatively small shift in the LMR peaks seen in Figure 1.5b. It can still be concluded as a result of Cao's investigation that LMRs do in fact occur regardless of geometry.

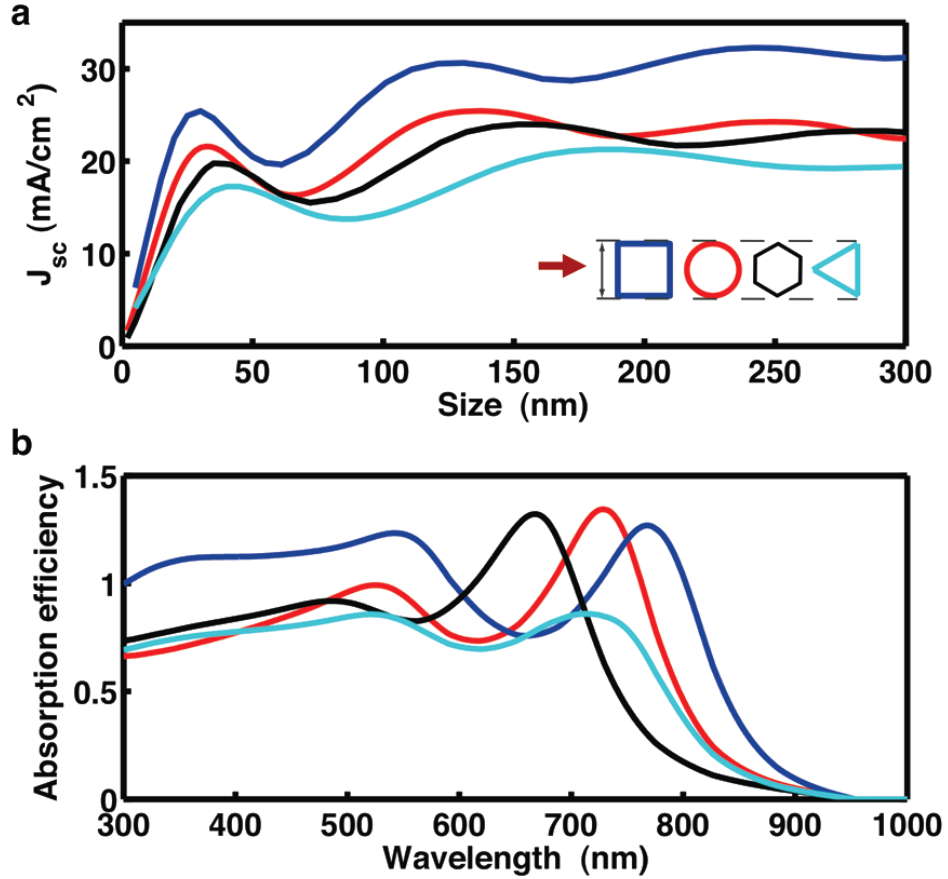


**Figure 1.5-** Generality of the optical resonance and short-circuit current enhancement to one-dimensional nanostructures: (a) Simulated short-circuit current density for one dimensional a-Si structures of rectangular, circular, hexagonal, and triangular cross section as a function of size. The red arrow in the inset shows illustrates the illumination geometry used in Cao's calculations. (b) Simulated absorption spectra of these one dimensional a-Si structures. Note the small variation in peak absorption which is believed to exist simply as a matter of volume change [36].

## 1.4 Plasmonics for light trapping

If there was a method available by which I can increase  $J_{sc}$  in the absorber portion of the solar cell via PM as seen by LMRs, I was motivated to

determine a way in which I could further increase  $J_{sc}$  via the back metallic contact portion of the device. The standard explanation as to why light is not efficiently absorbed at longer wavelengths is illustrated in Figure 1.6. The significant drop off in absorption in a thin Si film can be explained by the inset in Figure 1.6; red and infrared light has a longer absorption length than blue and green light, and therefore this light will not be absorbed efficiently in thin films.

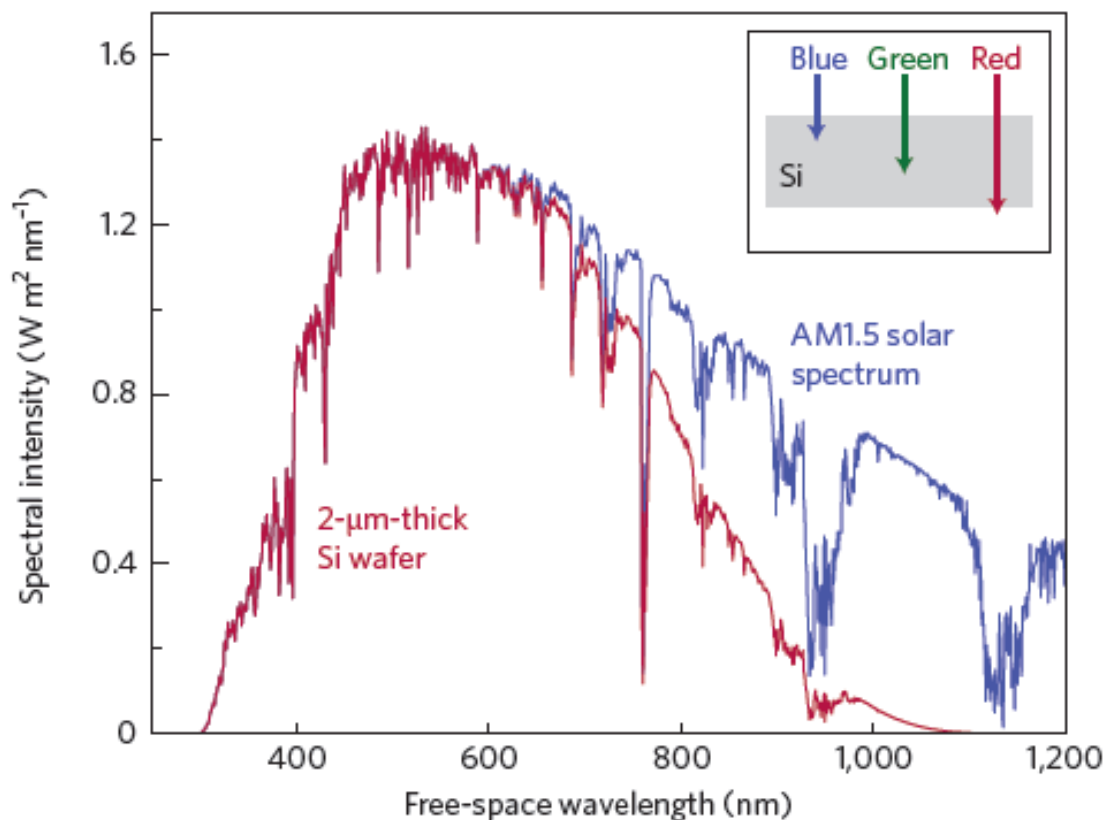


**Figure 1.6-** Illustrating classic optical absorption in a thin film solar cell; An AM1.5 filter solar spectrum, together with a graph that indicates the solar energy absorbed by a standard 2μm-thick Si film. It is clear that a large fraction of incident light in the spectral range of 600-1100 nm is not absorbed in a thin film solar cell [46].

If there was a way to concentrate or trap this 'lost' light in the thin film, this trapping effect would lead to higher efficiency in the cell resulting in a cheaper product. Plasmon resonance, or excitation of conduction electrons in metallic nanostructures (in this case the back contact), have already shown the facility to increase light absorption via a light trapping mechanism in multiple applications, and will be employed into the solar cell I attempt to create [38-45].

There are a number of different methods that can be used to take advantage of the effect of plasmonic structures as are shown in Figure 1.7. First, Figure 1.7a shows metallic nanoparticles acting both as a scattering and reflecting component as it guides light into the absorber layer. Second, Figure 1.7b displays metallic nanoparticles acting as a sub-wavelength antenna to increase the absorption cross-section of the absorber. Third, Figure 1.7c illustrates a metallic grating on the back surface of the device which can result in coupling of light into surface plasmon polariton (SPP) modes at the metal-semiconductor interface. SPPs are electromagnetic waves which travel along the interface between the metal contact and the semiconductor. This geometry has the net effect of efficiently trapping and guiding light into the semiconductor layer by turning the incident solar flux  $90^\circ$ . This bending of light into the horizontal results in absorption into the

semiconductor layer in a direction orders of magnitude longer than the absorption length leading to more efficient light absorption.

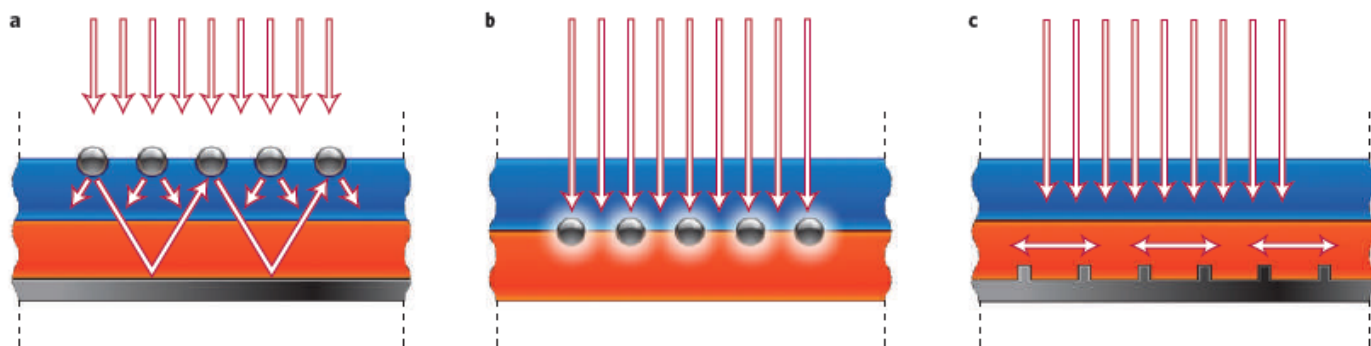


**Figure 1.7-** Plasmonic light-trapping geometries for thin-film solar cells: (a) Light trapping by scattering from metal nanoparticles at the surface of the solar cell. Light is preferentially scattered and trapped into the semiconductor thin film by multiple and high-angle scattering, causing an increase in the effective optical path length in the cell. (b) Light trapping by the excitation of localized surface plasmons in metal nanoparticles embedded in the semiconductor. The excited particles' near-field causes the creation of electron-hole pairs in the semiconductor. (c) Light trapping by the excitation of surface plasmon polaritons at the metal/semiconductor interface. A corrugated metal back surface couples light to surface plasmon polariton or photonic modes that propagate in the plane of the semiconductor layer [46].

Work by Vivian Ferry of Harry Atwater's research group at Caltech has shown the ability of the metallic grating option shown in Figure 1.7c to enhance the  $J_{sc}$  in her devices [47]. What she found was that as she introduced a 500 and 700 nm pitch metallic grating structure into the a-Si cell the short-circuit current was enhanced significantly compared to the cell without the metallic grating- shown in Figure 1.8.

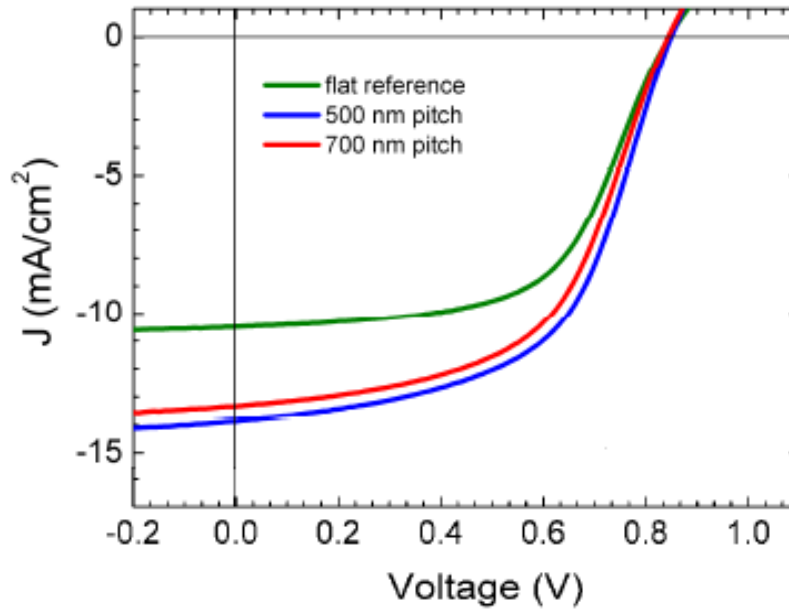


**Figure 1.8-** Electrical measurements of solar cells containing a plasmonic grating like that shown in Figure 1.7, revealing that when comparing the flat structure with no grating, to the two structures with 500 and 700 nm pitch, the pitched systems lead to an enhanced short-circuit current [47].

The increase in short-circuit current can be attributed to the ability of the metallic grating to trap light more effectively by redirecting the absorption path into the plane of the device as a result of phenomena like that in Figure 1.7c. As Figure 1.9 demonstrates, there is a stark increase in external quantum efficiency in the red region of the spectrum for the devices which have the metallic grating then for the device with the flat metallic conductor, showing the ability to 'trap' the once lost light.



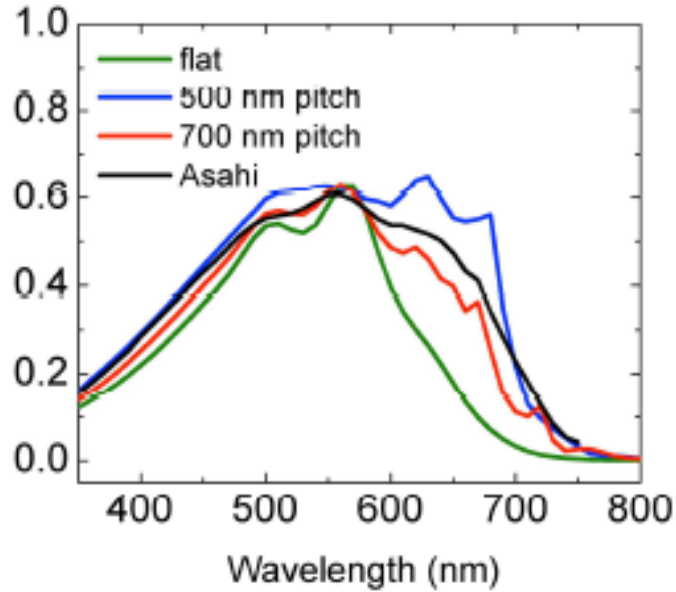


**Figure 1.9-** Results from measuring external quantum efficiency (EQE) spectra of flat, nanopatterned (500 and 700 nm pitch) and randomly structured cells (Asahi). The primary enhancement in photocurrent over the flat reference occurs from 550-800 nm; the range where the standard thin film has low absorption efficiency as displayed from Figure 1.6 [47].

What was also realized was that as the a-Si layer was made thinner, from 340 nm to 160 nm, the efficiency of the device stayed constant at 6.6%. Even though the magnitude of  $J_{sc}$  was reduced in the 160 nm device compared to the 340 nm device, the  $V_{oc}$  and FF were increased due to the decreased bulk recombination rate [48].

The conclusion of this work was twofold- first, the plasmonic grating back contact can be utilized to create SPPs which will oscillate in the horizontal plane of the device and thereby increase the number of e-h pairs created and second, efficiency is maintained while scaling down the

thickness of the absorber layer. This would lead me to believe that devices where the absorber layer is thinner than 160 nm can also provide respectable efficiencies while further reducing the material cost associated with the device.

In summary, the experiments performed throughout this dissertation were then done so with the goal of meeting the increasing worldwide energy demand through the use of a carbon neutral nanowire solar cell, while reducing processing and material costs and simultaneously attempting to maintain reasonable efficiencies. From the previously mentioned work I believe I can take advantage of both LMRs and plasmonic properties to help preserve efficiency in my solar cell while dropping the material demand by basing my device on nanowires. Based on this overall theme the first goal of my work will require the ability to fabricate metal and semiconducting nanowires, the subject of chapter two. Secondly, to fabricate a tunable grating-like structure of nanowires on the order 100 nm pitch and greater to allow for LMR and plasmon properties, the subject of chapter 3, and finally to build a single nanowire solar cell like that shown in Figure 1.2 and compare the single nanowire solar cell to a solar cell which potentially exhibits properties of LMRs and plasmons, the subject of chapter four. I will conclude in chapter four with how my work can further be adapted in the future to help meet the overall goal of providing an efficient and low-cost

solar cell as an attractive carbon neutral energy source which if realized, can serve as the new mainstream energy source of the future.

## Chapter 2

### Lead Selenide Nanowires Prepared by LPNE

#### 2.1 Motivation

Determining the semiconductor to be employed in my specific solar cell was an interesting choice. After careful thought and consideration it was decided that I would choose the optimal semiconducting material which demonstrates the highest efficiency of what is known as multiple exciton generation (MEG), with the hope of increasing the efficiency of the solar cell by generating multiple excitons from one input photon. As mentioned in chapter one, the S&Q calculation assumed that any energy in excess of the  $E_g$  of the semiconductor will be lost through thermal relaxation to the conduction band edge. The theory behind MEG provides a way in which energies in excess of this bandgap can instead be converted to create additional e-h pairs and thereby increase the  $J_{sc}$  of the cell and subsequently the efficiency- leading to a more cost effective device [67].

To further understand MEG one must first understand the term impact ionization (II). II, schematically shown in Figure 2.1, is a term describing a

process in bulk semiconductors whereby a photon,  $E_{ph}$ , with energy in excess of the bandgap, has the ability to knock additional electrons out of the valence band and into the conduction band as the mechanism of electron cooling- the MEG electron is shown as green in Figure 2.1 .

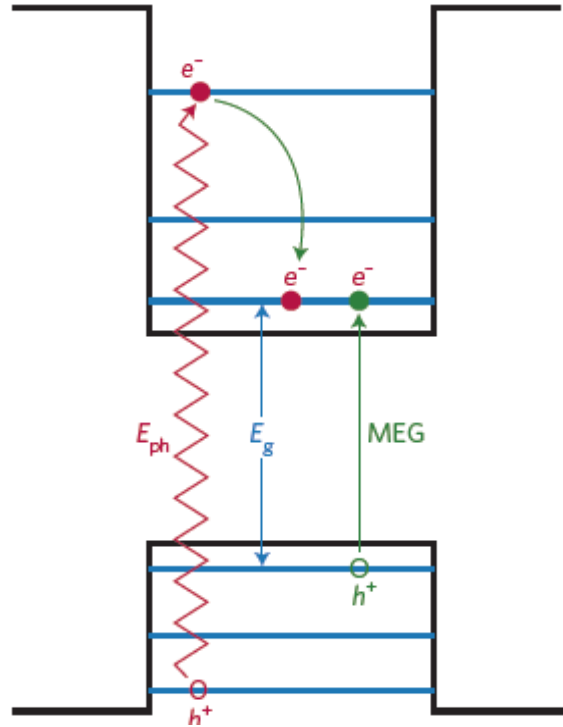


**Figure 2.1-** MEG in a quantum dot. A photon with energy  $E_{ph}$  excites an electron to a higher energy level (red arrow), leaving behind a positively-charged hole. This electron and hole form an exciton that then relaxes to a lower energy level, and at the same time a second electron is excited to a higher energy level (green arrows). As a result, a single photon creates two excitons. Horizontal blue lines represent quantum dot energy levels; and black lines represent potential barriers.

II in bulk semiconductors is not an efficient process and requires multiples of the semiconductor bandgap to create multiple excitons. The dominant semiconductor in the photovoltaic market is silicon with a  $E_g$  of 1.1

eV. With this  $E_g$ , II would require a minimum of 2.2 eV to occur. Energies this high do not correspond readily to energies abundant in the solar spectrum. However it has been shown that as quantum confinement begins to take place impact ionization can occur in quantum confined regions with much higher efficiency than in bulk material, assuming a material with a small  $E_g$  is being studied [67]. The term multiple exciton generation (MEG) is the analogue of II in quantum confined spaces. Observations have been made and will be discussed in further detail later in this work to show that MEG is an efficient process in quantum confined regions.

The ability to create multiple excitons for every absorbed photon leads to an increase in the photocurrent and thereby increases the solar-to electric energy conversion efficiency. The theoretical limit assuming an efficient MEG process has been proposed to allow for solar cell efficiencies to reach as high as 42-44% [68,69]. For MEG to occur, it must first be the dominant cooling mechanism for absorption energies in excess of  $2E_g$ . Because of the limitations imposed by II, other cooling pathways in the system will need to be impeded to allow for MEG to occur when  $E_{ph} > E_g$ . In the nanoscale level it is believed that competing cooling pathway in bulk devices, electron-phonon scattering, can be slowed due to quantum confinement properties.

A first theorized advantage held by nanoscale materials over the bulk is that as particles become smaller and begin to approach the material

specific Bohr radius, energy bands begin to cease and instead begin to resemble energy levels- this is shown in Figure 2.2.

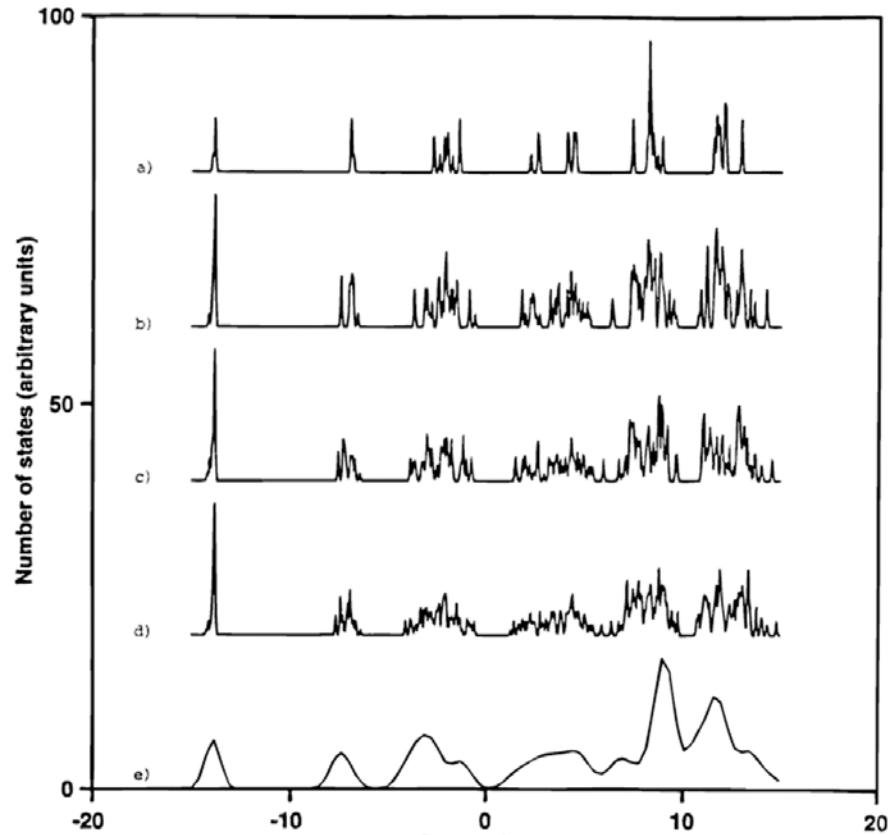


**Figure 2.2-** The calculated density of states of lead sulfide for (from top to bottom) an 8-atom, 32-atom, 56-atom, and 88-atom cluster [70].

As the energy levels become more discrete as the particles get smaller, the energy required to move from band to band grows to a point where multiple phonon scattering events are necessary to allow for transition between energy levels. This discretization is important because it removes an energy dissipation pathway. As the energy levels become more discrete, the energy required to move down one level becomes large

compared to the energy of a phonon so that to lose electronic energy via a phonon assisted process will require multiple phonons, making this less likely.

The ability to slow electron-phonon scattering as explained by energy levels is only one proposed advantage held by nanomaterials as opposed to bulk. There is a second advantage in quantum confined spaces that can cause the electron-phonon scattering rate to be retarded. The minimal space for exciton population causes the relaxation of linear momentum transition rules in this one-dimensional space and induces angular momentum selection rules, similar to that of an atom. This further limits the cooling rate of a hot exciton because it limits the energy levels that either the electron or hole can transition between.

The combination of discrete energy bands with the angular momentum conservation rules lead to a low probability of phonon scattering in quantum confined regions, thereby allowing for impact ionization to compete or potentially dominate as the major cooling pathway in such quantum confined regions.

If MEG does occur in nature, it would then be ideal to use the semiconducting material that has been shown to have the highest efficiency for MEG. The highest efficiency of MEG to date was found by Klimov in PbSe nanocrystals. The PbSe nanocrystals made are reported to have the ability



to create as many as 7 excitons at  $7.8 E_g$ . As a result of Klimov's study in conjunction with previous studies on MEG in PbSe, he proposed a 'new' photovoltaic efficiency shown in Figure 2.3 of 65% at 0.3 eV [71-75].

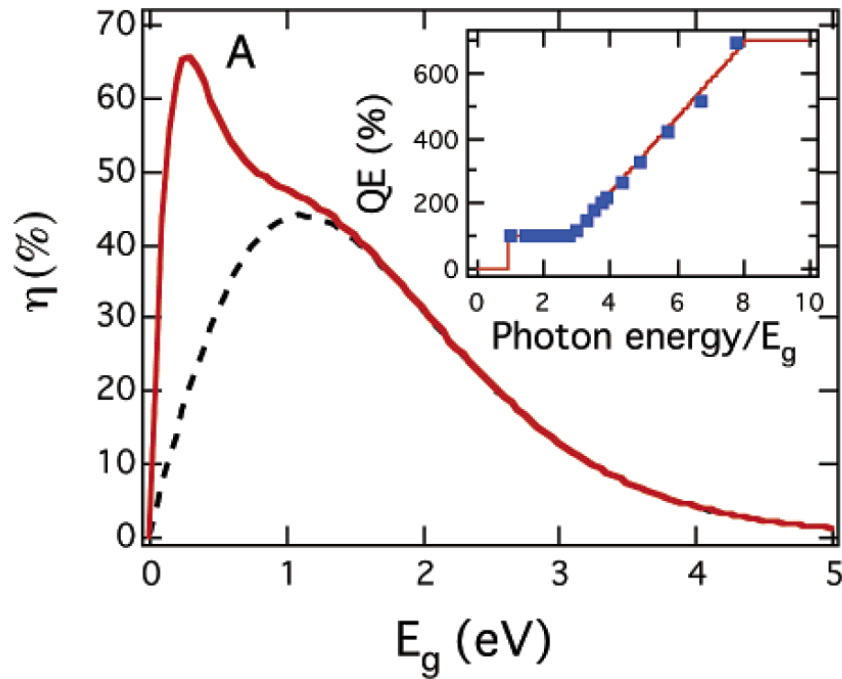


**Figure 2.3-** 'New' ultimate photovoltaic conversion efficiency (red) of 65% at 0.3 eV compared to the previous 44% at 1.2 eV (black) [69].

How appropriate that PbSe has a direct bandgap of 0.3 eV, which not only corresponds to the 'new' ultimate efficiency, but as well as to the material that has been reported to have created the highest amount of excitons. It should follow that PbSe nanowires fabricated by LPNE would then be an excellent choice to serve as a solar cell base. As an additional benefit, because PbSe has a large exciton Bohr radius of 46 nm it will not be

difficult to test for the presence of MEG to find agreement with Klimov's findings because of this relatively large dimension limit.

## **2.2 Experimental details**

With the knowledge that I will use PbSe as the semiconductor, I utilized a method which can create large arrays of nanowires which at the same time remains cost effective- lithographically patterned nanowire electrodeposition (LPNE). Lithographically patterned nanowire electrodeposition (LPNE) is a nanowire growth method which provides a cheaper alternative to present nanowire synthesis methods such as electron beam lithography, chemical vapor deposition, or chemical bath deposition. LPNE will result in more affordable production costs because it is a combination of parallel and time efficient processes, photolithography and electrodeposition, in opposition to standard methods of deposition which are either serial in nature and/or time consuming. LPNE therefore has the potential to reduce the processing costs associated with producing a solar cell and will therefore be the nanowire fabrication method of choice for my work, the process details of which will be explained shortly.

LPNE is a multistep nanowire deposition process, developed by the Penner group that uses photolithography to create a template for nanowire

deposition, and has been used to prepare gold, silver, platinum, palladium, bismuth, lead telluride, cadmium selenide, and even organic nanowires [49-66]. Nanowires synthesized from LPNE have been used in a variety of applications ranging from hydrogen sensors, to photo detectors, and even virus detection to name a few. A main advantage held by LPNE, and a main motivation in using it for my work, as will soon become evident, is that the height and width of fabricated nanowires are tunable from 10-100 nm and 20-500 nm respectively as well as independent from one another.

With a clear defined goal of creating PbSe nanowires utilizing the cheap fabrication method of LPNE, I will now transition into discussing how I successfully fabricated and characterized PbSe nanowires from LPNE.

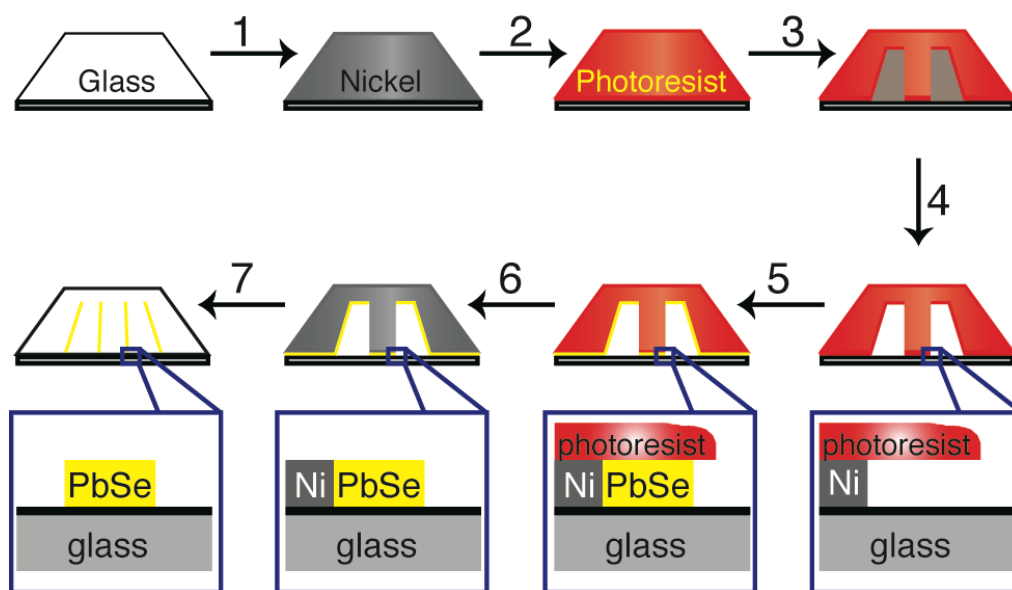


**Figure 2.4-** Process flow diagram for traditional LPNE method devised by the Penner group as a new method of nanowire fabrication.

To make lead selenide nanowires according to the LPNE process flow shown in scheme 1 above, the following seven steps of LPNE were followed:

- 1) Thermal evaporation using a Denton bench top turbo IV to evaporate a layer of 20-100 nm Ni film (Ni pellets 99.9999% from Kurt J. Lusk Company) onto a piece of 1"x1" glass previously submerged in a 10%:90% Nichromix/Sulfuric acid bath for a minimum of 24 hours;
- 2) Spin coat 1 mL of Microposit S1808 positive photoresist using a Laurel Technologies WS-400 spin coater at 2500 rpm for 80 seconds;
- 3) Pattern the photoresist with 3.3 seconds of exposure to 365 nm light from a 150 mW Hg ARC lamp inside an OAI Model 30 photolithography tool followed by 30 seconds of resist strip using MF-30 from Rohm and Haas;
- 4) Chemically etch the exposed Nickel using 0.8 M Nitric acid, resulting in an undercut of the photoresist to create a deposition template;
- 5) Electrochemically deposit the desired material, in this case PbSe, into the deposition template;
- 6) Remove excess photoresist via acetone rinse;
- 7) Chemically etch away the excess nickel with 0.8 M Nitric acid, leaving nanowires whose placement and length are determined by lithography.

After step 1-3 of the LPNE process are complete, I needed to verify that I had defined lithography before proceeding to the next step. The lack of variation in the photoresist edges seen in Figure 2.5 gives confidence that

photolithography will not present any fabrication limitations and I can therefore proceed to the next step in the LPNE process.



**Figure 2.5-** Optical microscope image taken under 50x, with relative scale bar of 5  $\mu\text{m}$  shown, illustrating lithography with no line edge variation; acceptable photolithography and development to proceed with next step in LPNE method.

Step 4 of the LPNE process requires a chemical etch to completely etch away all exposed nickel after photolithography as well as continued etching under the photoresist to create a trench underneath the photoresist. In the initial LPNE study the presence of the photoresist undercut was verified via SEM- this cross-section image is shown in Figure 2.6b [52]. The isotropically etched nickel edge can be seen sitting under the photoresist where the

adjacent trench sits, awaiting electrodeposition. I am including Figure 2.6a to show that the trench width is tunable as a function of etching time; this function will find further importance in chapter 3.

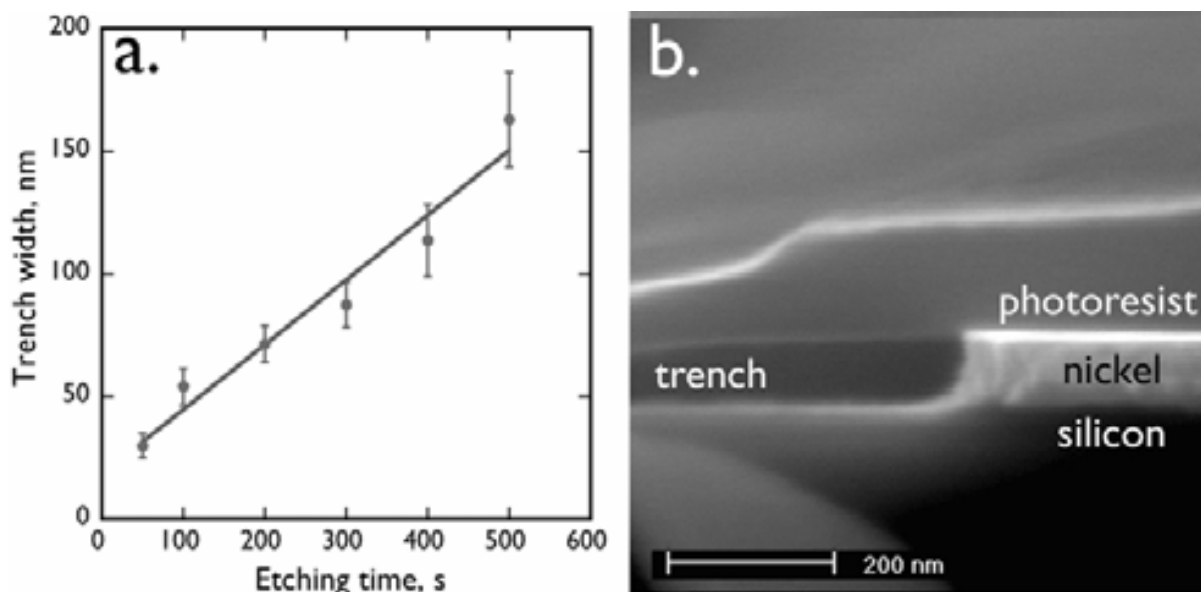


**Figure 2.6-** Control of LPNE trench and associated cross section image. (a) Trench width as a function of etching time, where longer etching time results in a wider trench- this will become important in chapter 3. (b) Cross-section scanning electron micrograph displaying the trench adjacent to the nickel edge, both layers sitting on top of the glass, but beneath the structurally stable photoresist [51].

Step 5 of the LPNE process is when I need to insure stoichiometric, cubic PbSe is electrochemically deposited. I synthesized PbSe nanowires via a constant potential method similar to the PbSe thin film electrodeposition reported by Saloniemi, et al with resulting current versus voltage (I-V) curves in Figure 2.7 below [76,77].

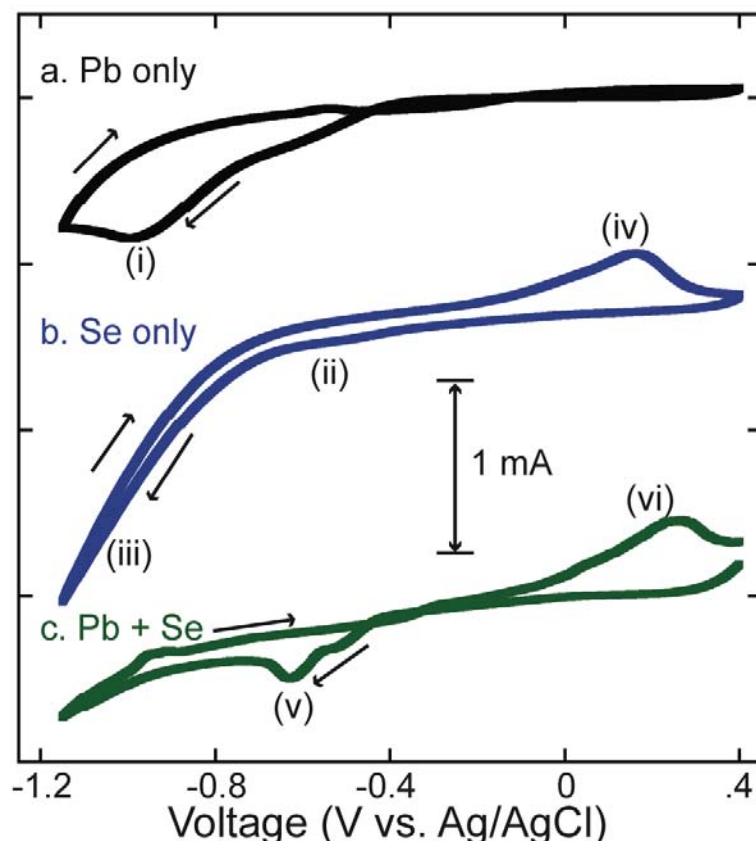


**Figure 2.7-** a-c) Cyclic voltammograms ( $20 \text{ mV s}^{-1}$ ) for solutions containing a) lead ( $[\text{Pb}^{2+}] = 10 \text{ mM}$ ) with  $0.1 \text{ M}$  EDTA at  $\text{pH} = 4$  in aqueous solution, b) selenium ( $[\text{HSeO}_3^-] = 1 \text{ mM}$ ) with  $0.1 \text{ M}$  EDTA at  $\text{pH} = 4$  in aqueous solution, and c) lead and selenium ( $[\text{Pb}^{2+}] = 10 \text{ mM}$ ,  $[\text{HSeO}_3^-] = 1 \text{ mM}$ ) with  $0.1 \text{ M}$  EDTA at  $\text{pH} = 4$  in aqueous solution. Voltammetric waves are assigned to the following reactions: Wave (i),  $\text{Pb}^{2+} + 2 \text{ e}^- \rightarrow \text{Pb}^0$ ; Wave (ii),  $\text{HSeO}_3^- + 5 \text{ H}^+ + 4 \text{ e}^- \rightarrow \text{Se}^0 + 3 \text{ H}_2\text{O}$ ; Wave (iii),  $2 \text{ H}_3\text{O}^+ + 2 \text{ e}^- \rightarrow \text{H}_2 + 2 \text{ H}_2\text{O}$ ; Wave (iv),  $\text{Se}^0 + 3 \text{ H}_2\text{O} \rightarrow \text{HSeO}_3^- + 5 \text{ H}^+ + 4 \text{ e}^-$ ; Wave (v),  $\text{Pb}^{2+} + \text{HSeO}_3^- + 5 \text{ H}^+ + 6 \text{ e}^- \rightarrow \text{PbSe} + 3 \text{ H}_2\text{O}$ ; Wave (vi),  $\text{PbSe} + 3 \text{ H}_2\text{O} \rightarrow \text{Pb}^{2+} + \text{HSeO}_3^- + 5 \text{ H}^+ + 6 \text{ e}^-$

In our method, PbSe electrodeposition was achieved with a computer controlled Gamry Instruments G300 Series potentiostat/galvanostat at room temperature, from a deposition solution containing  $0.1 \text{ M}$   $\text{Na}_2\text{EDTA}$  (Sigma Aldrich, Purity 99%),  $10 \text{ mM}$   $\text{Pb}(\text{NO}_3)_2$  (Sigma Aldrich, Purity 99.999%), and

1 mM  $\text{SeO}_2$  (Sigma Aldrich, Purity 99.999%) in NANOPure water (resistivity =  $18.0 \text{ M}\Omega \text{ cm}$ ), with the final solution pH adjusted to 4 by the drop-wise addition of conc.  $\text{HNO}_3$  (Sigma Aldrich, Reagent grade). The EDTA and large excess of  $\text{Pb}(\text{NO}_3)_2$ , relative to the  $\text{SeO}_2$  concentration, are needed to shift the deposition potentials so that the start of the lead reduction (wave (i) in Figure 1a) occurs at approximately the same potential as selenium reduction (wave (ii) in Figure 1b). This ensures that lead and selenium are co-deposited (wave (v) in Figure 1c) at a potential of approximately  $-0.6 \text{ V}$  vs.  $\text{Ag}/\text{AgCl}$  without excess lead or selenium present, as is evidenced by the lack of a second stripping wave in Figure 1c. After the final LPNE step all that remains on the glass surface is a parallel array of PbSe nanowire whose presence is verified using optical microscopy shown in FIGURE 2.8.

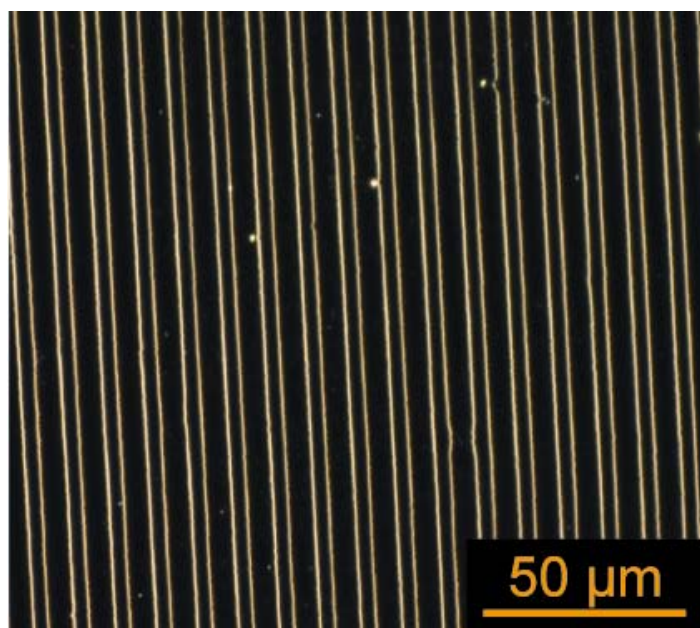


**Figure 2.8.** An optical micrograph of a parallel array of PbSe nanowires after completion of the entire LPNE process flow.



The successful electrodeposition of a nanowire array can be further verified using a FEI Nova NanoSEM at UC Davis' Northern California Nanotechnology Center (NCNC), equipped with a field emission gun (FEG), operating at 10 kV - a resulting array of PbSe nanowires is shown in Figure 2.9. All subsequent scanning electron microscope (SEM) will be assumed to be under the same conditions unless otherwise noted.

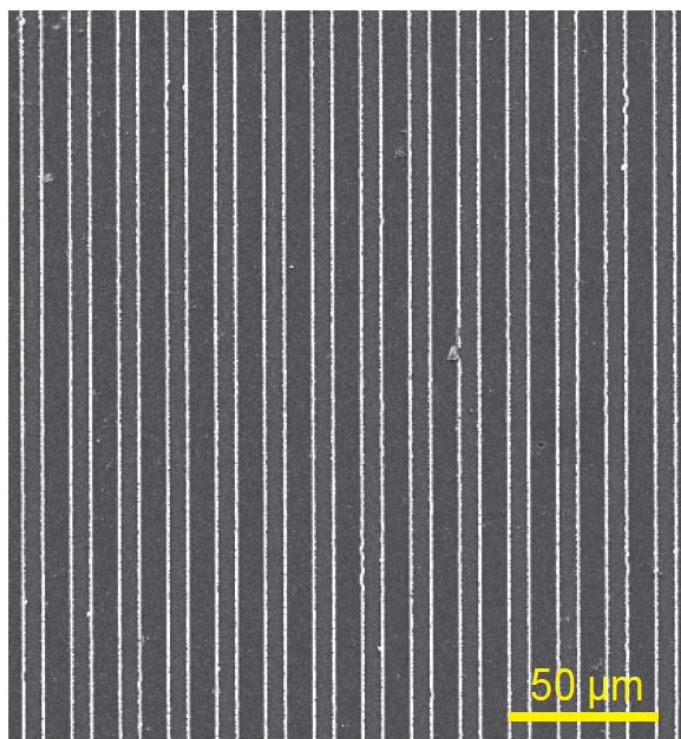


**Figure 2.9-** Low magnification SEM image showing an array of parallel PbSe nanowires with 5  $\mu\text{m}$  separation (scale bar = 50  $\mu\text{m}$ ).

The pitch in the nanowire array above is controlled by the photomask. The heights of all LPNE nanowires are equivalent to the height of the Nickel film thermally evaporated in step 1 of the LPNE process. The width of the

nanowire is dependent on electrodeposition time where the longer the deposition time the wider the wire. The width of the electrodeposited nanowire,  $w$ , into a rectangular trench using a time-invariant current density,  $J_{dep}$ , is governed by the following equation:

$$w = J_{dep} t_{dep} V_m / (nF)$$

Where  $t_{dep}$  is the deposition time,  $V_m$  is the molar volume of the deposited material,  $n$  is the number of electrons required for reduction, and  $F$  is Faraday's constant ( $9.645 \times 10^4 \text{C}$ ) [53].

While the heights of all LPNE are nanowires equivalent to the nickel film thickness independent of material, the rate of horizontal growth of LPNE nanowires are material dependent. This comparison is seen in the Figure 2.10 below.

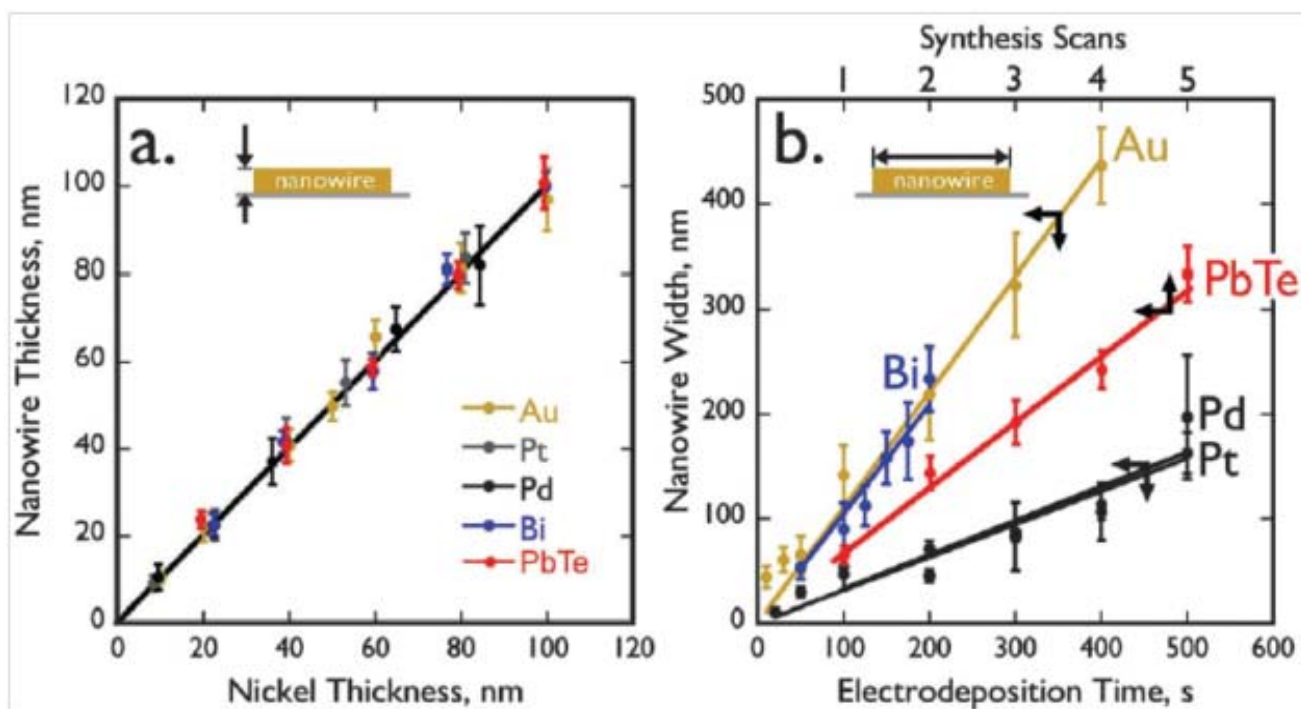


**Figure 2.10-** Both the height and width of a nanowire produced by LPNE can be independently controlled. (a) Nanowire height measured by atomic force microscopy (AFM) versus the thickness of evaporative layer. (b) Nanowire width measured by SEM *versus* electrodeposition duration; from reference 53.

Based on Figure 2.10a above I did not characterize the height of the lead selenide wires because previous nanowire materials Au, Pd, Pt all had a slope of 1.0 when plotting wire height versus Nickel thickness. Based on Figure 2.10b I did however see the need to calibrate the PbSe wire thickness versus deposition time because of the varying slope as the deposition material is changed- the resulting curve can be seen in Figure 2.11.

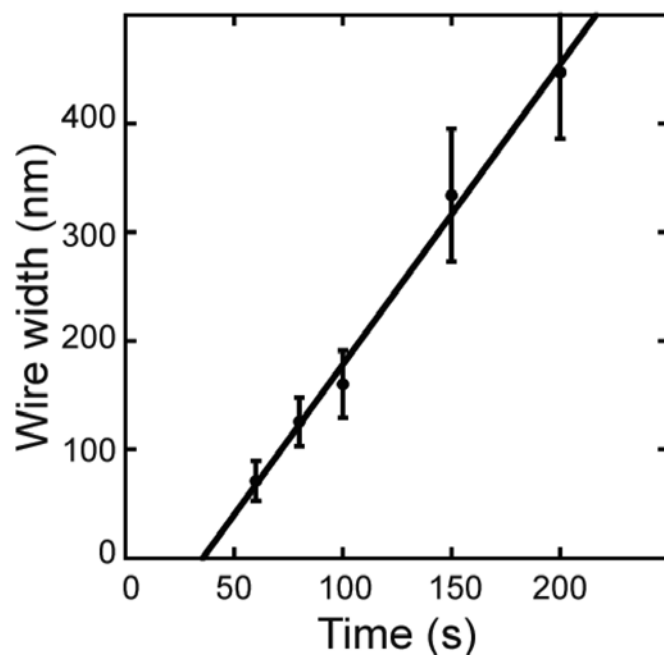


**Figure 2.11-** Calibration curve of PbSe nanowire width as a function of electrodeposition duration. The error bars indicate one standard deviation in the average width of nanowires across different LPNE samples.

As can be seen in Figure 2.12, the lead selenide nanowire growth which takes place opposite the Nickel electrode begins to have random protrusions which grow larger at longer electrodeposition times, resulting in a larger PbSe nanowire variation width at longer deposition times. Even with these large protrusions at long deposition times, the PbSe width versus time calibration curve shows linearly leading me to the confidence that there is still a high degree of control over the nanowire width.

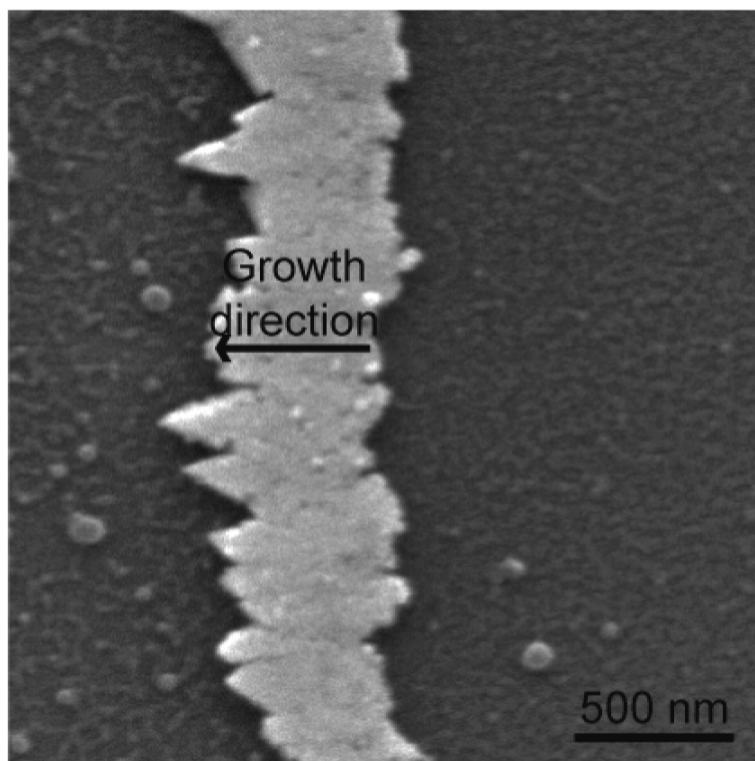


**Figure 2.12-** High magnification SEM image of a single PbSe nanowire depicting the protrusions opposite of the nickel edge (scale bar= 500 nm).

## 2.3 Characterization

After successful synthesizing nanowires from the PbSe electrodeposition bath, it was necessary to confirm the presence of stoichiometric cubic lead selenide and *only* stoichiometric cubic lead selenide in the nanowire. The first characterization tool used was an energy-dispersive X-Ray spectrometer (EDX). A resulting EDX spectrum of a single nanowire like that in Figure 2.12 is shown in Figure 2.13. The atomic percentage analysis of the EDX spectrum led to a ratio suggesting

stoichiometric PbSe nanowires as only lead and selenium are present, and are so at a ratio of 50.2:49.8.

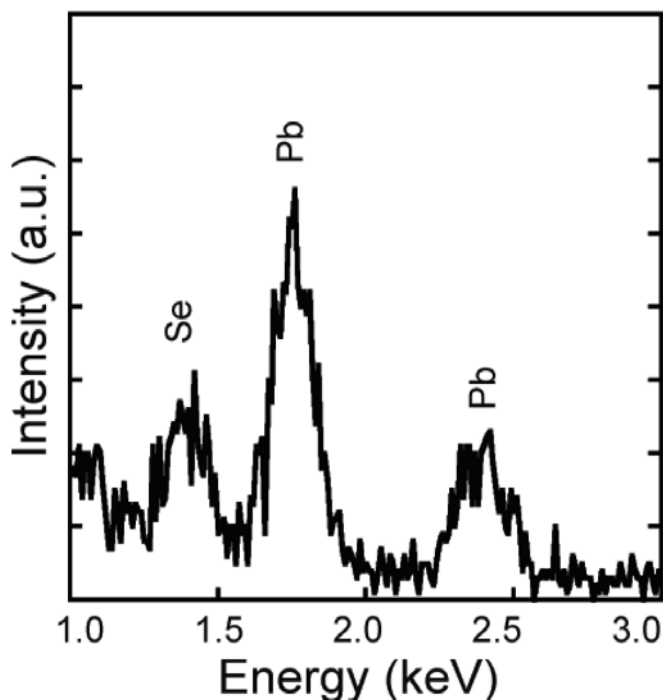


**Figure 2.13-** EDX spectra of a single PbSe nanowire showing the presence of lead and selenium with a measured atomic ratio nearly 50:50.

Now fully confident that I have the correct stoichiometric ratio of lead and selenium for PbSe nanowires, the next step was to test for the structural makeup of the electrodeposit. PbSe is a face-centered cubic structure just like rock salt, NaCl. If I can confirm the face-centered cubic presence of PbSe via X-Ray diffraction (XRD) and selected area electron diffraction (SAED) in conjunction with the EDX results I can be confident that stoichiometric PbSe has in fact been electrodeposited.

A sample of 500 nm wide lead selenide nanowires was prepared, upon which X-ray diffraction was performed using a Rigaku Ultima III (Rigaku, Tokyo, Japan) high resolution X-ray diffractometer (XRD) with a Cu Ka irradiation, operated at 40 kV and 44 mA. Data processing software was used to resolve the crystal size and full-width at half-maximum.

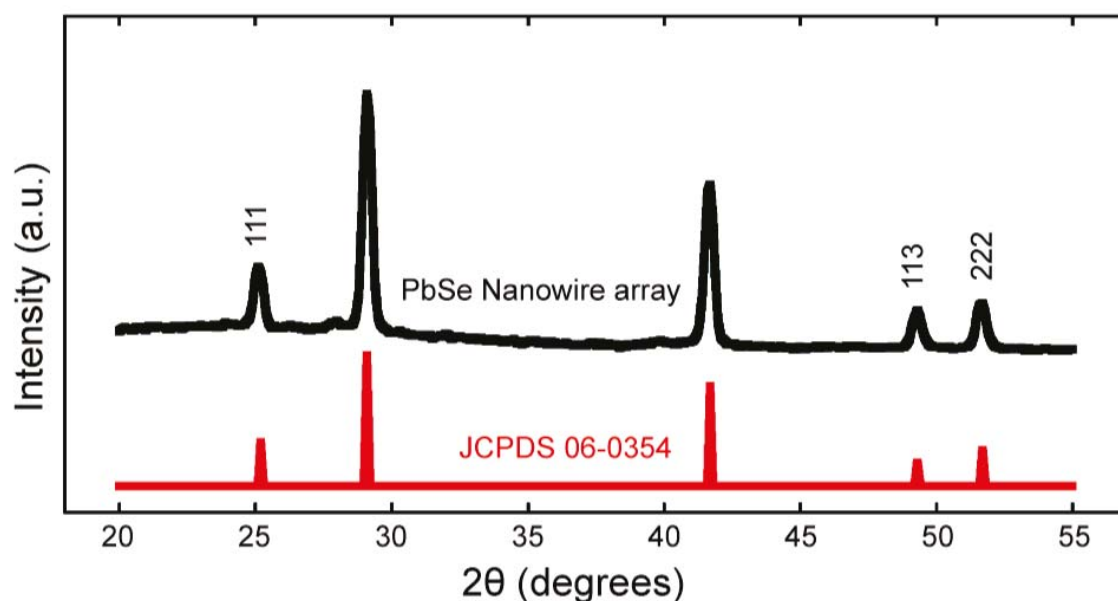


**Figure 2.14-** X-ray diffraction patterns from an array of 500 nm wide PbSe nanowires (black) compared to a reference pattern for cubic PbSe (JCPDS 06-0354).

The X-ray diffraction spectrum obtained using the PbSe nanowire array is shown, and compared with the standard cubic PbSe diffraction pattern in Figure 2.14. The resulting spectrum is a match for the presence of cubic PbSe as well as evidence that no residual deposits of Pb or Se are present in

the nanowire array. After completion of the Scherrer analysis it was shown that the average grain size in the PbSe nanowire was 15 nm as shown in Table 2.1 below. The Scherrer analysis was performed using the following equation:

$$d = \frac{K\lambda}{\beta \cos \theta}$$

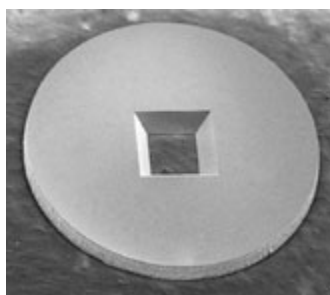
Where d is the particle size, K is the dimensionless shape factor taken to be 0.9,  $\beta$  is the full width at half-max (FWHM), and  $\theta$  is the Bragg angle. The FWHM was determined by using XPert High Score Plus XRD Analysis software.

Table 2.1- Average Grain Size from Scherrer Analysis

FWHM	2theta (deg)	grain size (nm)
0.2564	25.11	5.95
0.3067	29.20	5.02
0.0712	41.67	22.38
0.0936	49.27	17.45
0.0759	51.66	21.79
Average		14.52



To obtain electron diffraction requires the use of a TEM. To place nanowires on a TEM grid using LPNE is not a trivial task. The nanowires need to be grown traditionally by LPNE on glass and then transferred from the glass substrate to a TEM grid, as previously done, or the nanowires can to be grown directly on a TEM grid following the LPNE process [56]. I wanted to attempt to grow the nanowires directly on a TEM grid, but this would require a portion of the grid to be substantially thin, as thin as 50 nm to allow for the TEM electrons to penetrate through the thickness of the nanowire for viable imaging. After searching for TEM grids that would meet the aforementioned requirements, it was found that Ted Pella manufactures silicon nitride TEM grids with a 50 nm support film dimensions of 50  $\mu\text{m}$  x 50 $\mu\text{m}$  as shown in via SEM in Figure 2.15.



**Figure 2.15-** A SEM image of a 50 $\mu\text{m}$  x 50 $\mu\text{m}$  support film at the center of a silicon nitride TEM grid (provided by Ted Pella).

The 2500  $\mu\text{m}^2$  area is a sufficient substrate size for nanowires to be grown directly using the LPNE process without needing to transfer nanowires from glass to a grid. This type of TEM grid is then employed for nanowire

growth, following all steps identical to LPNE process, but instead of using glass as the substrate the TEM grid now is the substrate. A silver paste is used as a conductive metal contact across the supporting glass substrate where an alligator clip acts as a conductor from the potentiostat to the TEM grid itself as shown in Figure 2.16a. The TEM grid can then be immersed in the PbSe electrolytic bath for deposition as shown in Figure 2.16b.

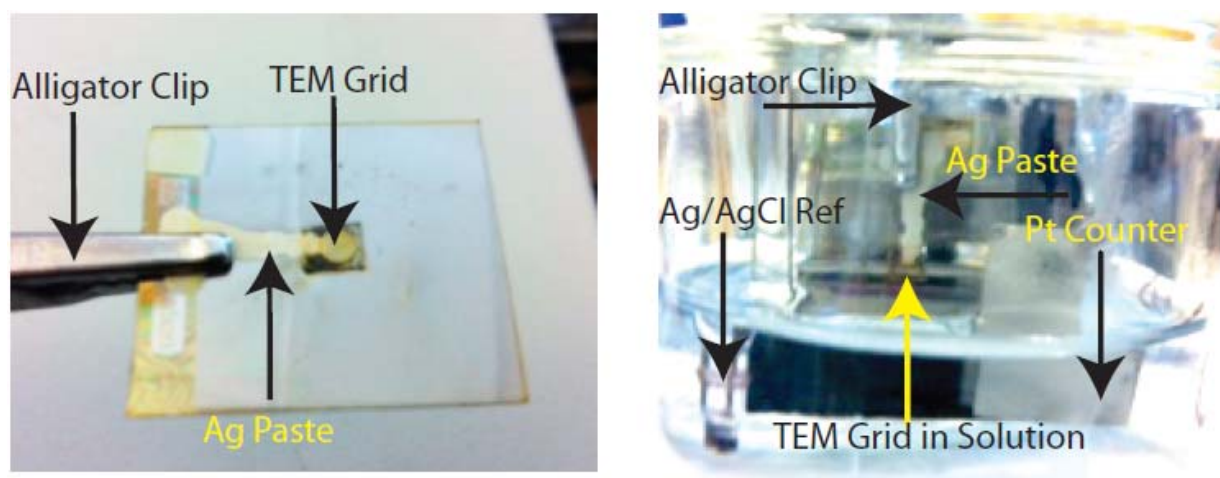


**Figure 2.16-** Illustrating growth of LPNE nanowires on TEM grid. (a) From left to right; Alligator clip from potentiostat, Ag paste connecting alligator clip to the TEM grid. (b) Immersion of substrate containing the TEM grid into a three electrode electrochemical cell that is ready to electrodeposit.

A single PbSe nanowire, approximately 40 nm in height and 250 nm wide, was then grown on a TEM grid as shown above and imaged using a FEI Tecnai 12 transmission electron microscope (TEM) operated at 120 kV at UC Berkeley's Electron Microscopy Lab. The resulting images, shown in Figure 2.17 below, display the nanocrystalline nature of LPNE nanowires, with grain

sizes in the range of 5-100 nm. One observation from Figure 2.17 is PbSe grains which grow closer to the Nickel edge (left side of the nanowire) are smaller than grains which grow further from Nickel edge; this observation concurs with previous work on LPNE nanowires [51].

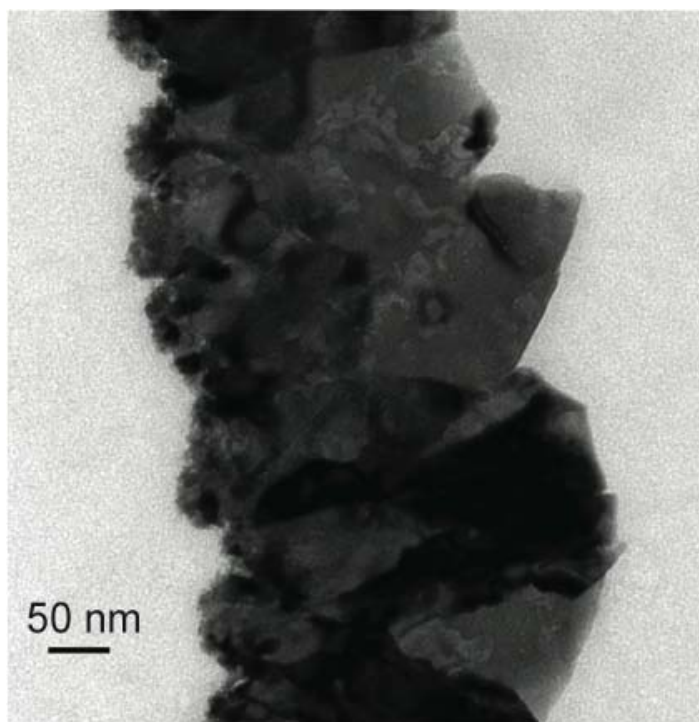


**Figure 2.17-** TEM image of a single PbSe nanowire showing grain sizes ranging from 20-100 nm (scale bar = 50 nm).

Selected area electron diffraction (SAED) was next obtained on the nanowire in Figure 2.17 with the resulting diffraction pattern displayed in Figure 2.18. The result of the SAED shows that the five inner rings can be indexed to cubic PbSe (JCPDS 06-0354). On top of this result there was no other material present, leading to the conclusion, in conjunction with the

EDX and XRD that I have successfully fabricated stoichiometric, cubic lead selenide nanowires.

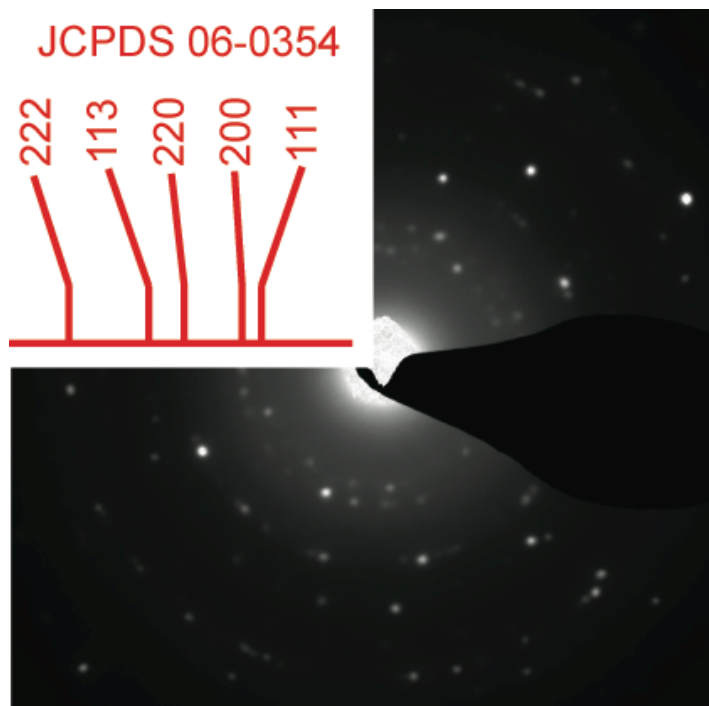


**Figure 2.18-** Selected area electron diffraction of the nanowire from Figure 2.17 with the inner five rings indexed to cubic PbSe (JCPDS 06-0354).

Raman spectroscopy was another characterization tool employed on the PbSe nanowires. An in depth study on the Raman spectra of PbSe quantum dots was done by Blackburn *et al.* and their results can be used as for comparison [78]. It should also be noted that first-order Raman scattering in the rock salt crystal structure of PbSe is forbidden due to the inversion symmetry of its point group.

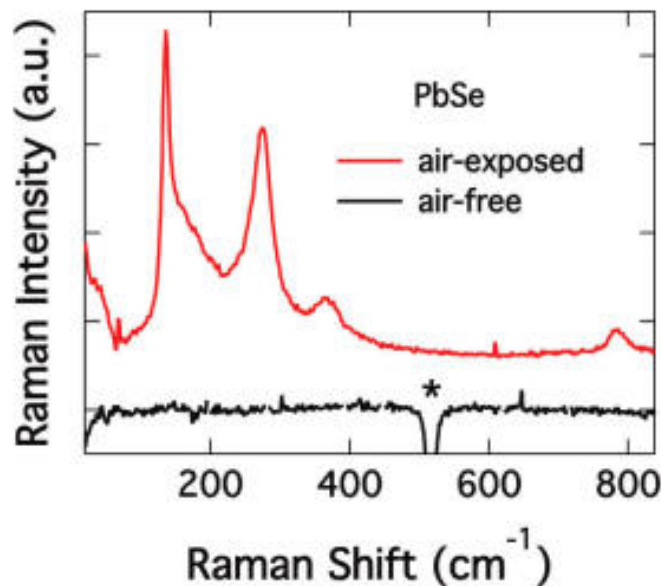


**Figure 2.19-** Comparison of Raman spectra for a PbSe quantum dot film measured in air (red) and measured in an airtight cell (black). The asterisk marks the position of the silicon film used as a background correction.

In Blackburn's study, the Raman spectra of identical PbSe quantum dots were taken in open atmosphere and in an air-free cell; the results are shown in Figure 2.19. The spectrum in black corresponds to the PbSe quantum dots in the air-free cell and shows the presence of zero Raman peaks. The spectrum in red corresponds to the sample of quantum dots taken in open air and shows stark differences to the spectrum in the air-free cell- namely the presence of multiple peaks. The conclusion of this study was that the peaks in the open air sample correspond to the photooxidation of the PbSe quantum dots, a result of this material being extremely prone to

oxidation, while the lack of peaks in air-free sample could be considered a more reasonable spectrum for PbSe [79-84].

The Raman spectra of PbSe nanowires synthesized in our lab was studied, with the resulting spectra excited with an Argon-ion laser at 514.5 nm shown in Figure 2.20.

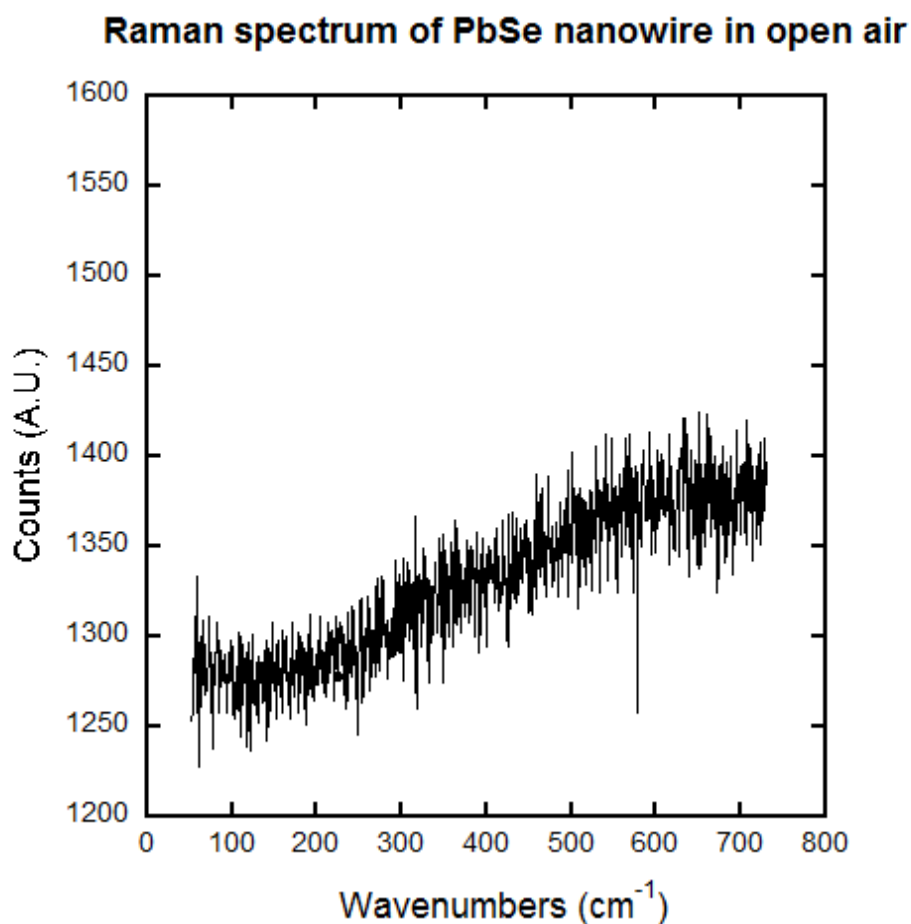


**Figure 2.20-** Raman spectra of air exposed PbSe nanowires prepared by LPNE.

It was previously concluded from the SAED, and XRD that my PbSe nanowires do not oxidize in open air based on the absence of PbO or PbSeO<sub>4</sub> in both of these characterization tools; however it would be hard to characterize a thin oxidation layer with these instruments. The Raman spectrum of our PbSe nanowires could also prove the absence of any oxidation of the PbSe nanowires which is also positive for a potential solar cell based on this material. There could however be experimental error as the Raman spectra of nanowires have not been heavily studied on the setup used to investigate my nanowires. In addition, there exists the possibility that the present employed characterization tools are not adequate to identify an oxidation layer. Another lead chalcogenide nanowire prepared via LPNE, PbTe, has shown the presence of oxidation in small amount via X-ray photoelectron spectroscopy (XPS) [56]. XPS would be a characterization more beneficial to investigate the presence of oxides in my PbSe nanowire; however no XPS was readily available for use during my tenure and would be a relevant subject for future study.

Now fully confident that I have successfully fabricated PbSe nanowires, the next step will be to determine if I can construct nanowires in the regime where quantum confinement takes place. The SEM image shown in Figure 2.21 illustrates the ability to tune the width of the nanowire to a size smaller than that of the Bohr radius of PbSe, 46 nm.

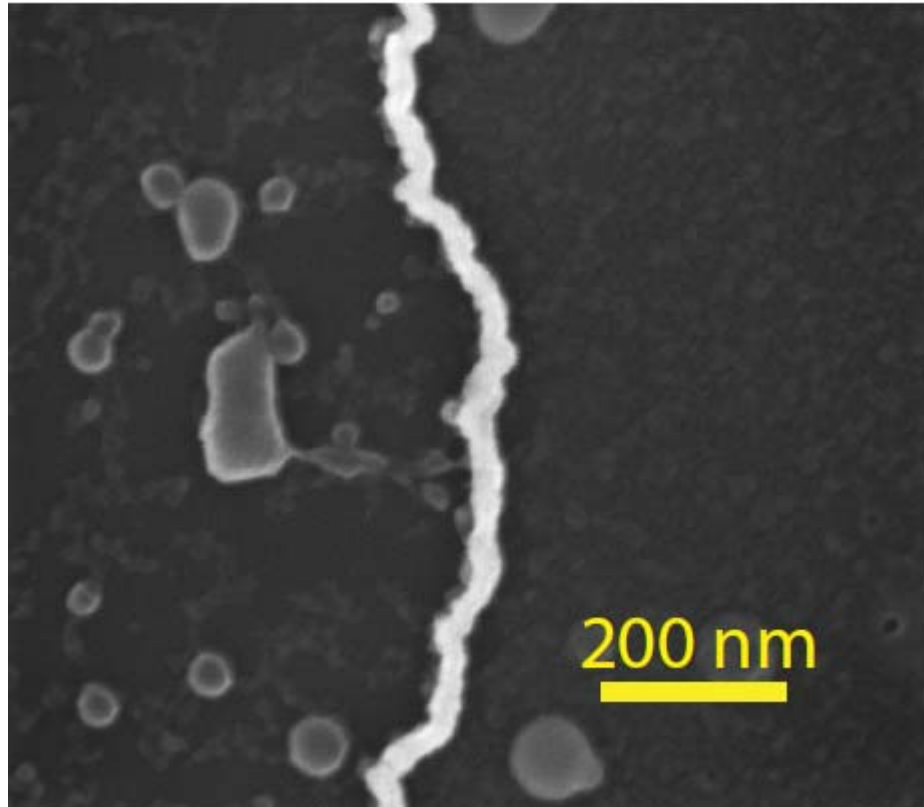


**Figure 2.21-** A SEM image of a PbSe nanowire created by LPNE with a width of approximately 30 nm.

By fabricating wires with widths smaller than the Bohr radius of PbSe, I now have the ability to obtain a two-dimensional structure. With the goal of creating a structure as small as one-dimension to take of advantage of the MEG properties, I still need to create another tunable dimension, in this case the height of the wire. Because I am using LPNE as my nanowire fabrication method, and the height of the nickel deposition is the height of the nanowire when employing this method, I can tune the nanowire height below the Bohr radius of 46 nm as shown in Figure 2.22.



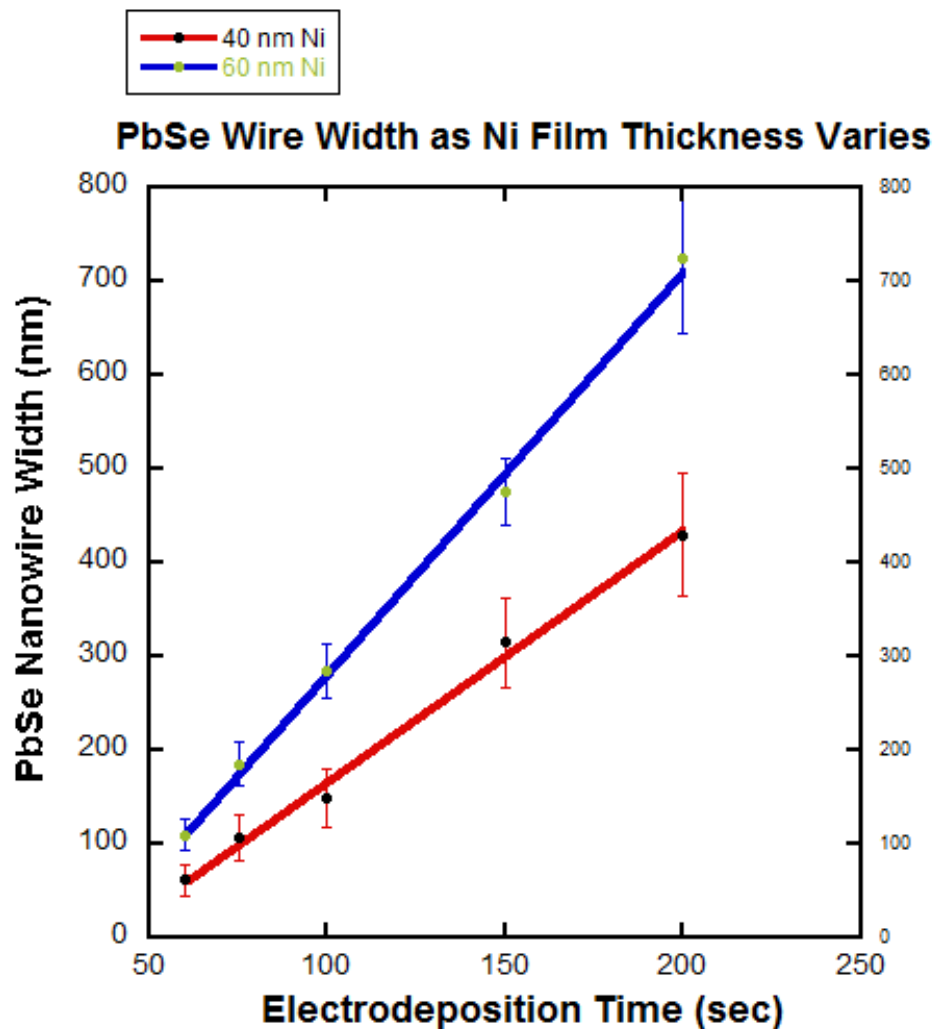


**Figure 2.22-** Comparison of PbSe nanowire width with varying nickel film thickness. The thicker nickel film leads to an increased rate of deposition.

The increase in slope as the height of Ni film thickness increases can be explained by the increased rate of mass transfer during electrodeposition due to the larger 'opening' provided by the taller trench. Even though the rate of electrodeposition changes as the height of the nickel thickness varies, I can still control the width of the nanowire as a function of time leading to

the ability to tune the wire height and width independent of one another. Due to this result I can be certain that I have the ability to tune two dimensions of the nanowire and therefore provide dimensions at which the MEG efficiency in PbSe nanowires via LPNE can be calculated.

To test for MEG with electrical measurements I need to confirm that such a measurement is possible with the fabricated nanowires. Electrical measurements of a single PbSe nanowire can in fact be performed by a slight modification to the LPNE method. Instead of performing the final etch step to leave isolated nanowires, an additional photolithography step can be added to selectively etch away portions of the nickel. Nickel contacts can be now be made to a single nanowire as shown in Figure 2.23.

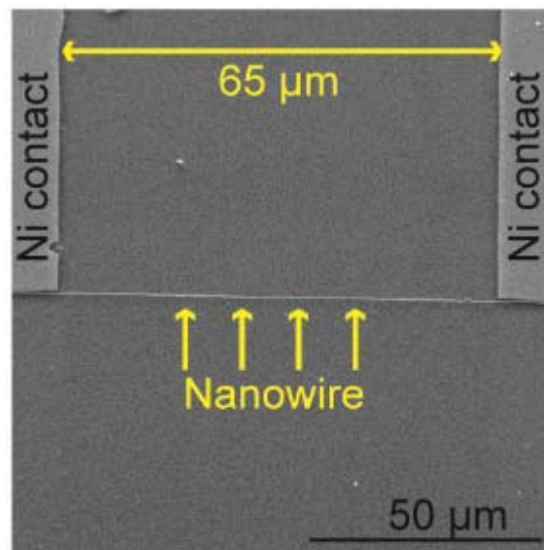


**Figure 2.23-** SEM image of a single PbSe nanowire with two nickel contacts.

By placing metal contacts on a single nanowire, current-voltage (I-V) characteristics of that nanowire can be performed. The I-V curve of a single nanowire over a large voltage range is shown in Figure 2.24, shows diode-like behavior, suggesting that the metal-nanowire contact is not Ohmic.

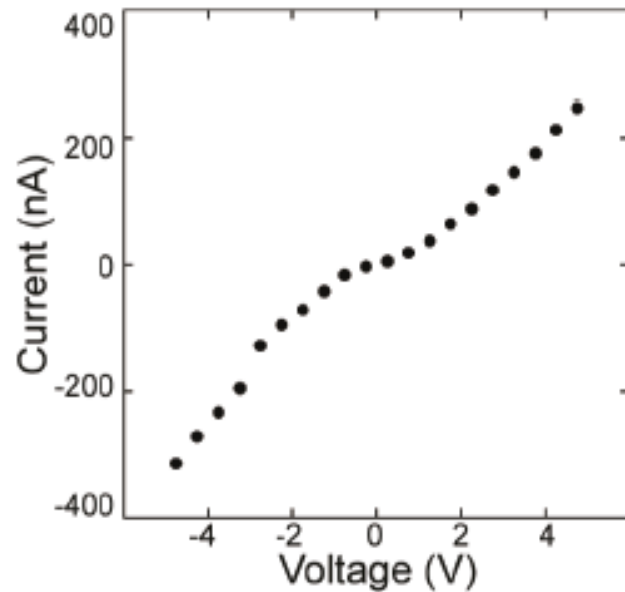


**Figure 2.24-** Large bias I-V curve of a single 40 nm (h) x 158 nm (w) x 63  $\mu$ m (l) PbSe nanowire displaying diode like behavior.

However, over a smaller voltage range the curve is linear, as can be seen for four separate nanowires with differing aspect ratios in Figure 2.25.

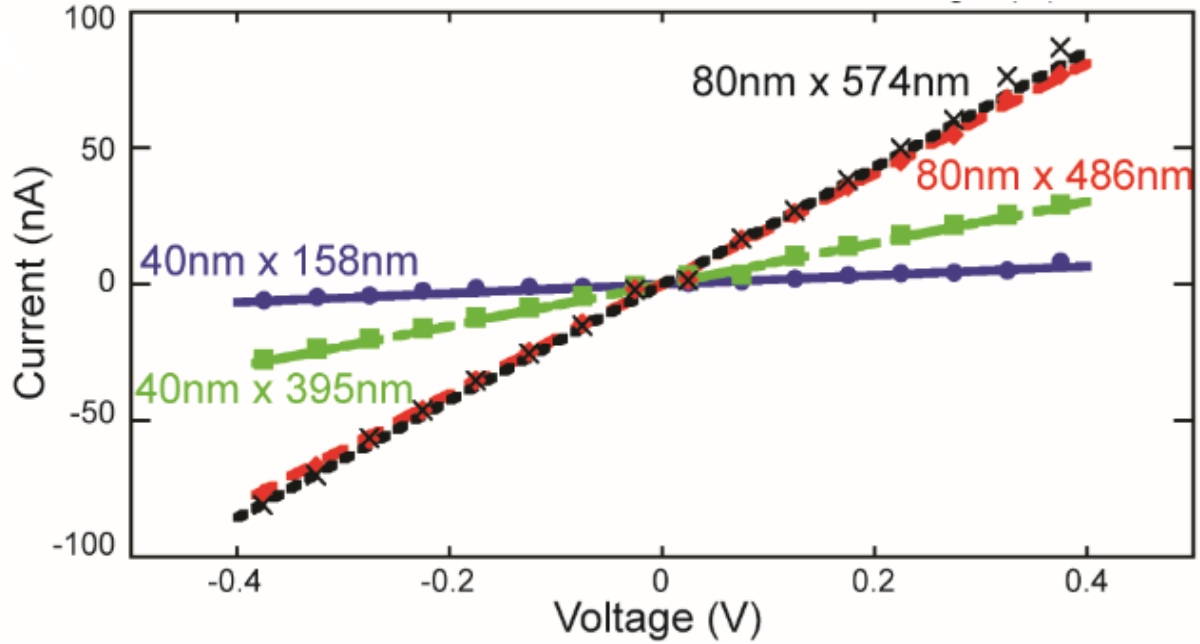


**Figure 2.25**-Small bias I-V curves of a single PbSe nanowire with dimensions of 40 nm (h) x 158 nm (w) x 64  $\mu\text{m}$  (l) (blue circles), 40 nm(h) x 395 nm (w) x 68.5  $\mu\text{m}$ (l) (green squares), 80nm(h) x 486 nm (w) x 138  $\mu\text{m}$  (l) (red diamonds), and 80 nm (h) x 574 nm (w) x 98.5  $\mu\text{m}$  (l) (black crosses).

The calculated resistivities from the I-V curves are shown in Table 2.1, and are similar to, although larger than, both the resistivity of a single crystal nanowire prepared via VLS by Fardy et al, and a nanowire like assembly of PbSe nanoparticles prepared via chemical reaction [85,86]. The slight increase in resistivity of our nanowire deposits could be explained by electric scattering at grain boundaries as well as gaps between grains when comparing the resistivity to the aforementioned measurements on higher quality materials.

Table 2.2- Comparison of Electrical Resistivity for PbSe Nanowires with Different Aspect Ratios

sample	height (nm)	width (nm)	length (um)	resistivity ( $10^{-3} \Omega m$ )
1	40	158	64	6.0
2	40	395	68.5	3.0
3	80	486	138	1.4
4	80	574	98.5	2.2
ref 85				1.5
ref 86				1.5

With the new knowledge that I can successfully make electrical measurements on PbSe nanowires fabricated via LPNE I now know that I have the ability to test for the presence of MEG. However at this point I will diverge from MEG as testing for MEG itself is an intensive process and will be revisited briefly at the conclusion of the dissertation.

I will instead use the knowledge that I have successfully fabricated PbSe nanowires via LPNE with the ability to perform electrical measurements, use this as the absorber layer in my solar cell, and proceed to chapter 3 of the dissertation- creating the grating structure for improved PM.

## Chapter 3

### High-Density Gold Nanowire Arrays

#### 3.1 Motivation

With the need to create a grating-like structure on the order of 100 nm pitch while using LPNE presents a real problem; presently the LPNE method limits the spacing between nanowires, or pitch, as a function of the diffraction of light. If I found a means to bypass this pitch limitation it not only allow for PM studies to be performed but as a byproduct, would also increase the surface density of any device constructed with LPNE nanowires- sensors, photodetectors, thermoelectric, as well as solar cells [49-66]. The smallest resolvable feature,  $d$ , that can be printed by optical lithography is determined by the Rayleigh equation [87]:

$$d=k\lambda/(NA)$$

The variable  $\lambda$  is the wavelength of light used during exposure, the variable  $NA$  is called the numerical aperture and is a function of the range of angles that can be accepted or emitted during exposure, and the variable  $k$  is the resolution factor- a complex combination of variables in the photolithography

process including the quality of the photoresist and the use of resolution enhancing techniques.

In my lab the variable  $\lambda$  is 365 nm, the variable  $k$  is 0.75, and the variable NA is 0.8. With these numbers in the Rayleigh equation, the LPNE systems in our lab will allow for the smallest resolvable feature to be approximately 400 nm. Couple this result with the fact that the smallest resolvable feature from published LPNE results is 2  $\mu\text{m}$ , and it can be seen that the ability to meet the pitch requirement for PM is not readily available with present LPNE standards where photolithography determines the pitch.

If I want to increase the number of devices or nanowires per area to improve present LPNE devices and allow for dimensions necessary for efficient PM while still taking advantage of the cost efficient LPNE method, I need to amend the LPNE method in such a way to reduce the pitch between nanowires where photolithography no longer is the variable affecting the pitch. I also would need to do so in such a way that does not require an increase in cost associated with this change. Additionally if I were successful I would want to make this adaptation to allow for a tunable nanowire pitch below 500 nm. This would allow me to take advantage of the leaky mode and plasmon resonances that occur in semiconducting and metal nanomaterials as it relates to the goal of creating a cheaper solar cell.

## **3.2 Experimental Details**

To address this pitch limitation of LPNE, the high-density LPNE method or HDLPNE method was theorized and is shown in Figure 3.1.

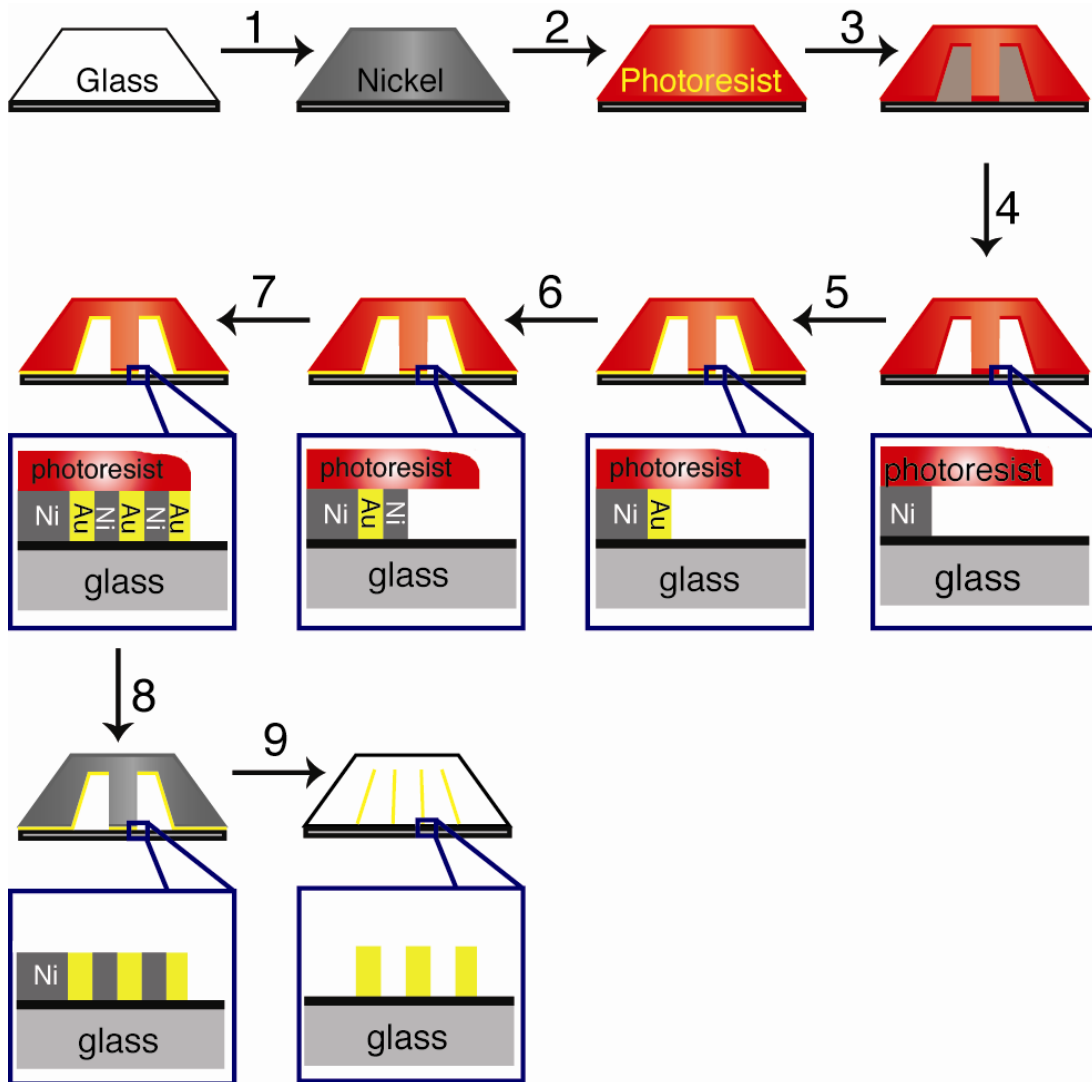


**Figure 3.1-** Schematic of HDLPNE process flow.

The HDLPNE process flow is identical to the LPNE method until step 6 where Au electrodeposition has been performed on the Ni edge. As opposed to the LPNE process where the photoresist would be removed and a final Ni



edge would be removed resulting in standalone Au wires with pitch limited by diffraction of light, the Au edge is instead used as an electrodeposition edge for a Ni electrodeposition step. Once Ni has been electrodeposited onto the Au edge, Au can be electrodeposited onto the new electrodeposited Ni edge and the alternating depositions of Au-Ni-Au-Ni can be repeated until I want to terminate the process or until the trench has been completely filled. What follows after all electrodeposition steps are complete is a resist strip and final chemical etch of Ni, including all electrodeposited Ni. What should result is a metal nanowire array whose pitch is a function of the Ni electrodeposition width. It was further hypothesized that the Ni electrodeposition width should also be a function of electrodeposition time resulting in the pitch between adjacent Au nanowires being a function of Ni electrodeposition time.

I put the HDLPNE idea to practice to determine if the LPNE could be modified to create nanowires with pitch below 500 nm. The first alteration to the LPNE method will occur during step 4 from scheme 1 above, where the initial chemical etch of Ni will be performed for a longer period of time. As opposed to the 200-300 nm trench created after a 5 minute initial chemical etch, the HDLPNE method will require a tunable trench width up to and occasionally greater than 1  $\mu\text{m}$  in width. A trench width of this magnitude can require over 20 minutes of initial etching, as can be verified from Figure

2.6a, but will allow for multiple electrodeposits to take place without overfilling the trench.

After creating the wide trench necessary for HDLPNE I employed the commercially available Clean Earth Nickel and Gold plating solutions to electrodeposit Au and Ni. The Au nanowire electrodeposition has been studied in the LPNE process previously so it was straightforward to determine a reasonable electrodeposition potential and time- between 10 and 300 seconds at -0.95V vs. Ag/AgCl should yield a Au nanowire with width between 30-300 nm. However Ni electrodeposition had not been studied previously with LPNE and would therefore need to be investigated. The first step to electroplating nickel was to determine a reasonable deposition potential. This was done by studying the CV in the Clean Earth Ni plating solution on Au nanoband working electrodes which had been electrodeposited on the Nickel edge. The resulting curve of this study can be observed in Figure 3.2, which shows current corresponding to reduction beginning at -0.2 V vs Ag/AgCl. I wanted to be sure that Ni was being plated, so I decided to use a potential of -0.70 V as a starting point for nickel reduction. A potential far negative from the initial reduction had to be avoided due to hydrogen evolution occurring below -0.6 V.

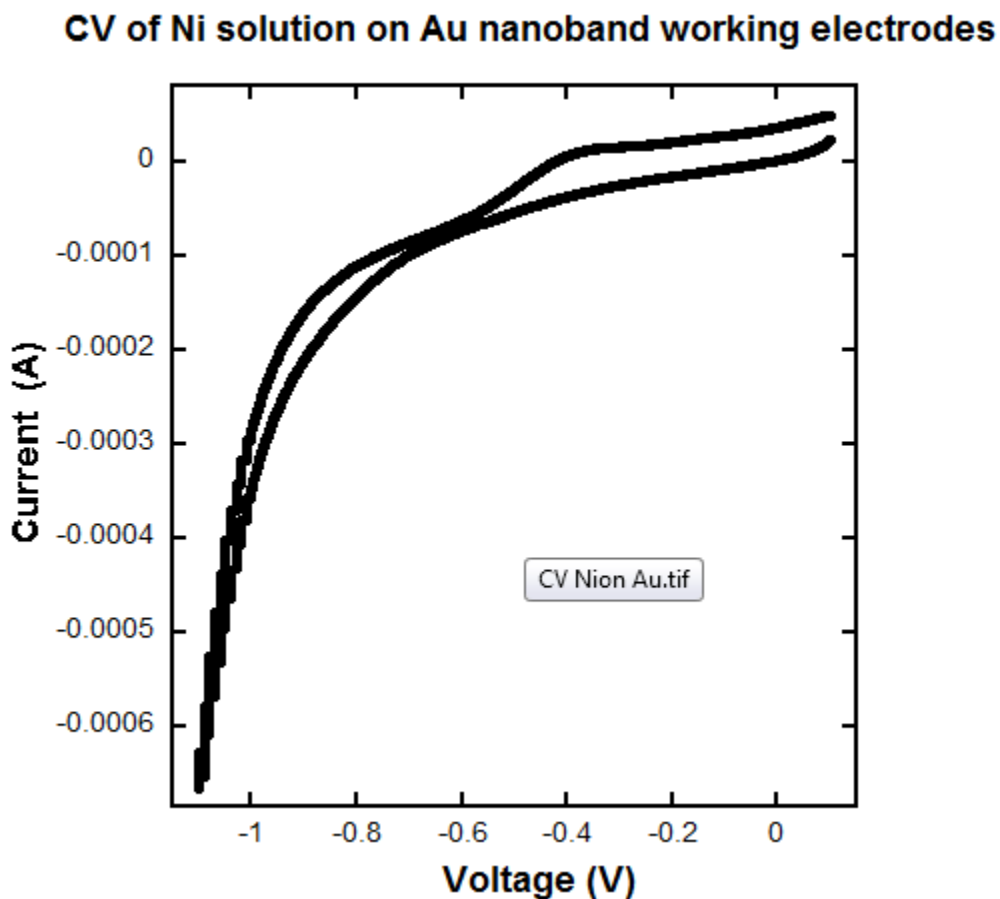


**Figure 3.2-** CV in nickel electroplating solution where gold nanobands act at the working electrode.

After determining a plating potential for Ni the next step was to determine the plating time. Because Ni is a metal, it was thought that the deposition time should be in the same realm of previous metal depositions from LPNE like that shown from Figure 2.10. On top of the large overpotential of -0.70V being applied it was thought a deposition time of 500 seconds would yield a pitch of at least a few hundred nanometers. Couple that thought with the fact that during deposition the reductive current was

nearly an order of magnitude larger than that of Au only added to the belief that a wide Ni electrodeposition was being performed. After completing a second Au deposition on the electrodeposited Ni edge, removing the photoresist and Ni, I took the samples to the SEM to view the presence of what I hoped would be Au nanowires that were separated by a few hundred nanometers. Instead what I saw was something like that shown in Figure 3.3- a wide Au nanowire with next to no real separation present in the wire array.

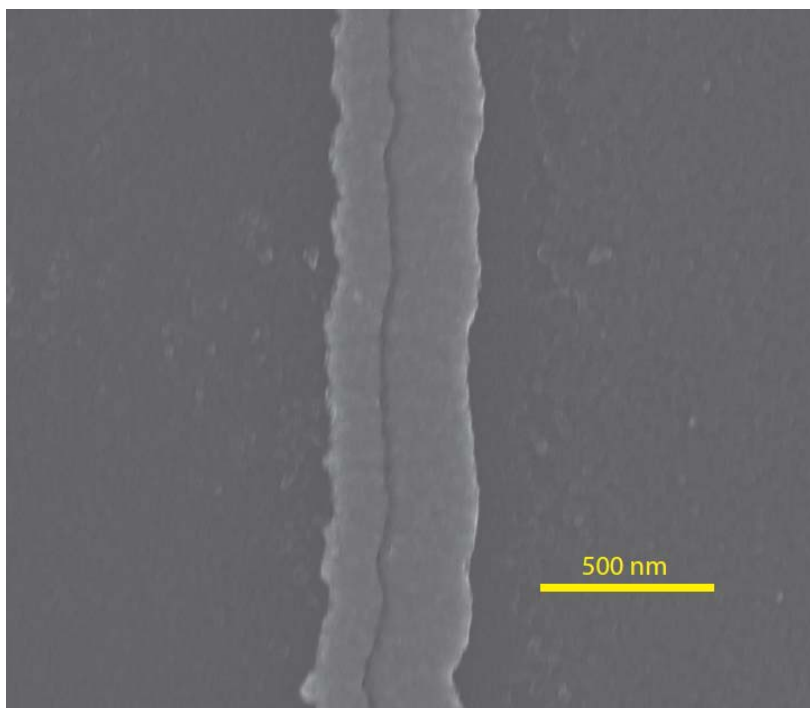


**Figure 3.3-** An SEM image of initial HDLPNE results using a nickel reduction potential of -0.7 V vs Ag/AgCl.

The result from Figure 3.3 leads me to believe that I was in fact electrodepositing a small amount of Ni onto the Au nanoelectrode. The next

course was to either apply a larger overpotential or increase the deposition time. Wanting to keep the HDLPNE processing costs down, the choice was to increase the overpotential. On top of this motivation, all published data on LPNE metal nanowires require no more than 500 seconds of deposition time for a deposition width greater than 200 nm. With these ideas in mind I proceeded to increase my deposition potential from -0.70V to -1.0V in the hopes that this will increase the rate of deposition and increase the pitch between adjacent Au nanowires. Upon changing the deposition potential for Ni while depositing the same duration as before, I received nanowire arrays like that shown in Figure 3.4.

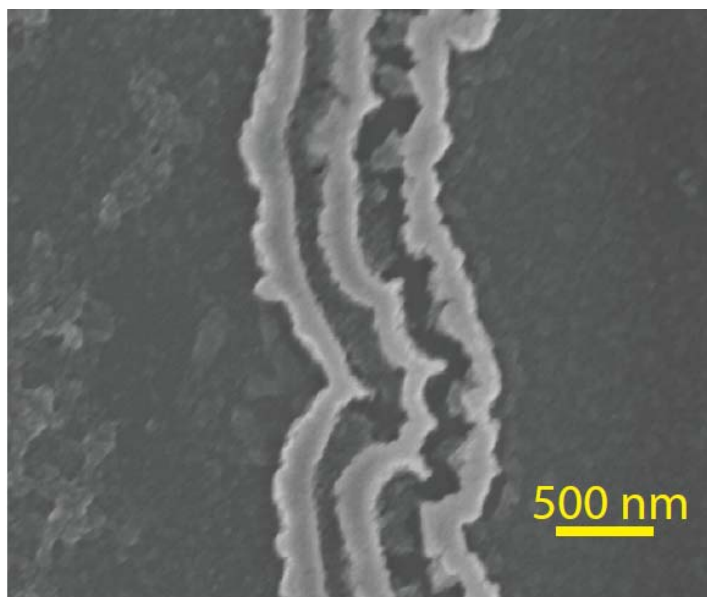


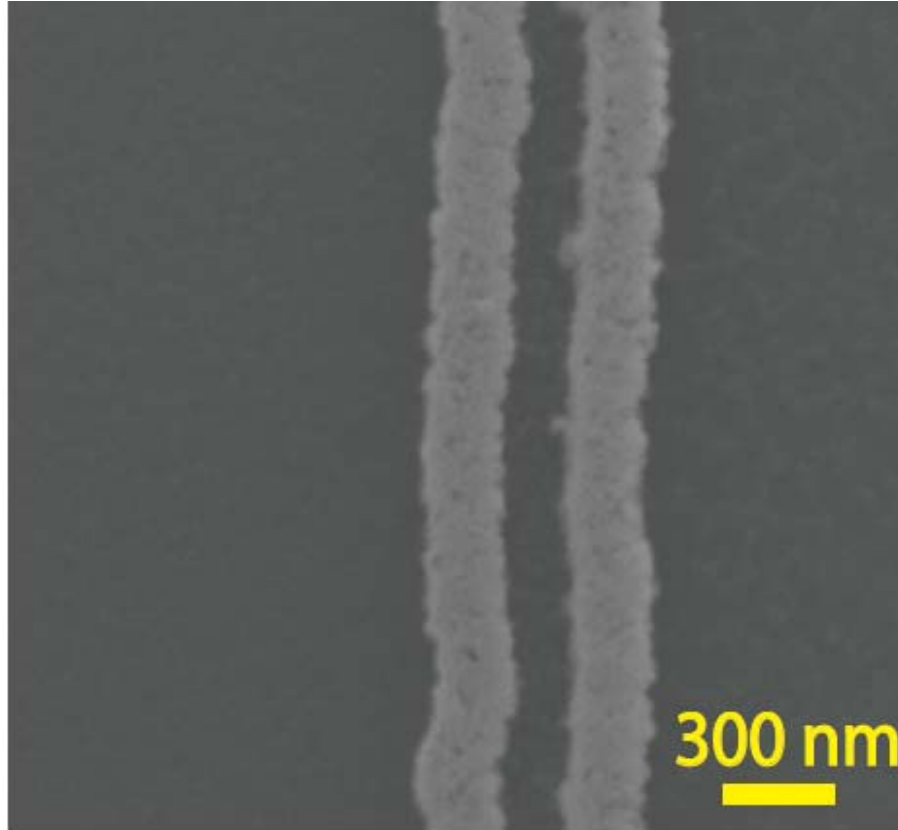
**Figure 3.4-** Winding Au nanowire array resulting from increasing the deposition potential of Ni from -0.70V to -1.0V

This type of nanowire array was an initial success because of the fact that I have been able to successfully place Au nanowires within a pitch of

100 nm. However there are still a couple of problems with the array in Figure 3.4; Problem number one is that the standard deviation of the pitch is large, or the pitch between Au nanowires is not well defined, and problem number two is that the Au nanowire edges themselves are not well defined. However, possessing the knowledge that I was in fact able to create an array with a pitch of 100 nm gives promise that the HDLPNE method is plausible. At this point the next question became how can a smoother pitch and Au nanowire edge be realized while still being able to fabricate a pitch down to 100 nm?

To address this I decided to reduce the deposition potentials and increase the deposition time. Additionally I introduced a nucleation step for both the Au and Ni electrodeposition to allow for a quick initial nucleation or 'coating' of Au on Ni or Ni on Au. For the Au deposition a nucleation potential of -1.1V was applied for 0.25 seconds and for Ni a nucleation potential of -1.1V was applied for 0.50 seconds. After the nucleation steps were complete I would further continue to grow the metals at a slower rate to provide for slower mass transfer; for both Nickel and Au I decided to tune the deposition potential to -0.85V, in the hopes that the pitch and Au nanowire edges will be smoother. What resulted after performing the nucleation steps and slower deposition rate potential can be seen in Figure 3.5. This two Au nanowire array has a pitch of approximately 100 nm but

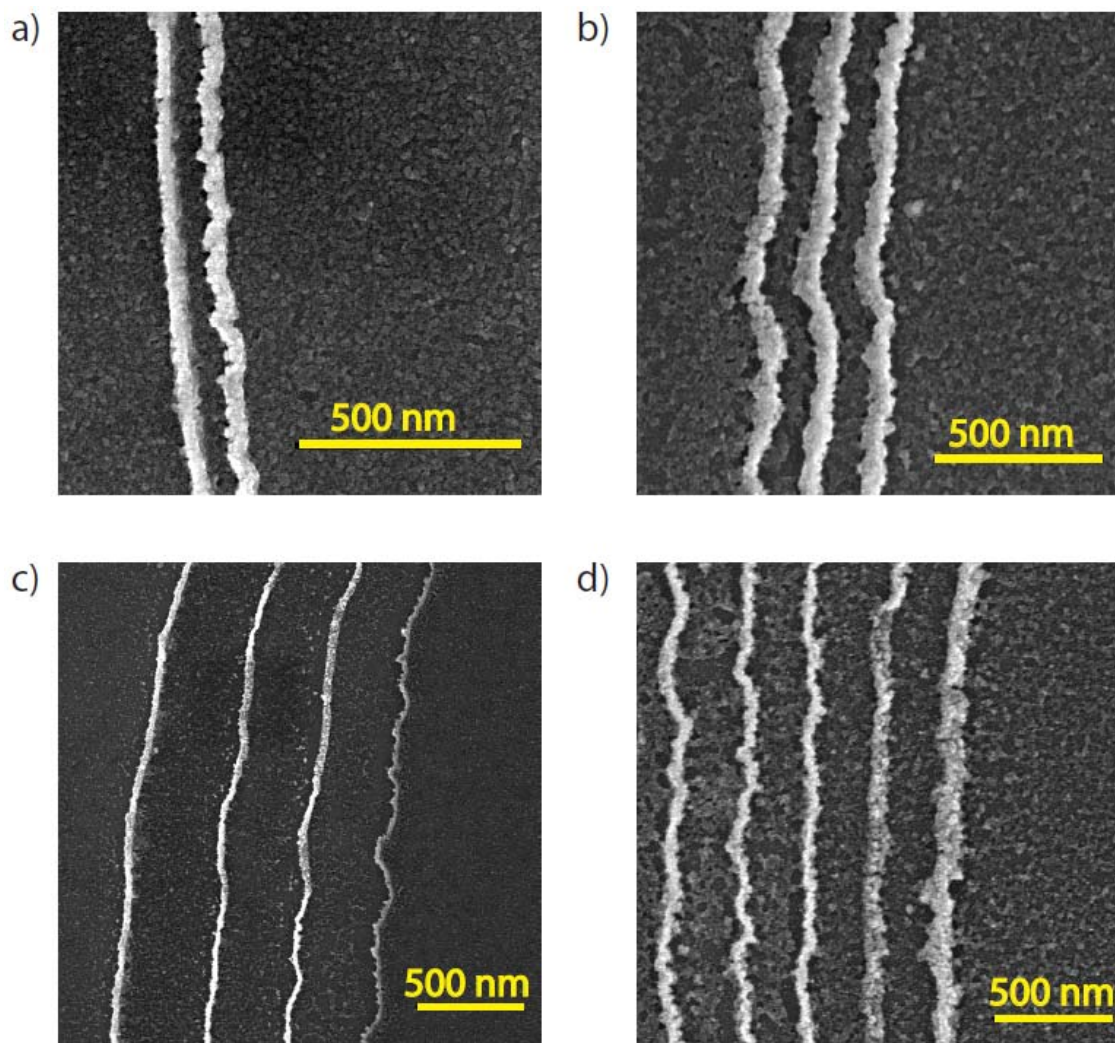
more importantly the Au nanowire edges and pitch between the Au nanowires is well defined. The conclusion from this image was to proceed by using the short nucleation growth followed by a slower electrodeposition rate caused by application of the smaller overpotential.



**Figure 3.5-** Well defined 200 nm Au nanowire edges with a well defined pitch of 100 nm.

### 3.3 Results

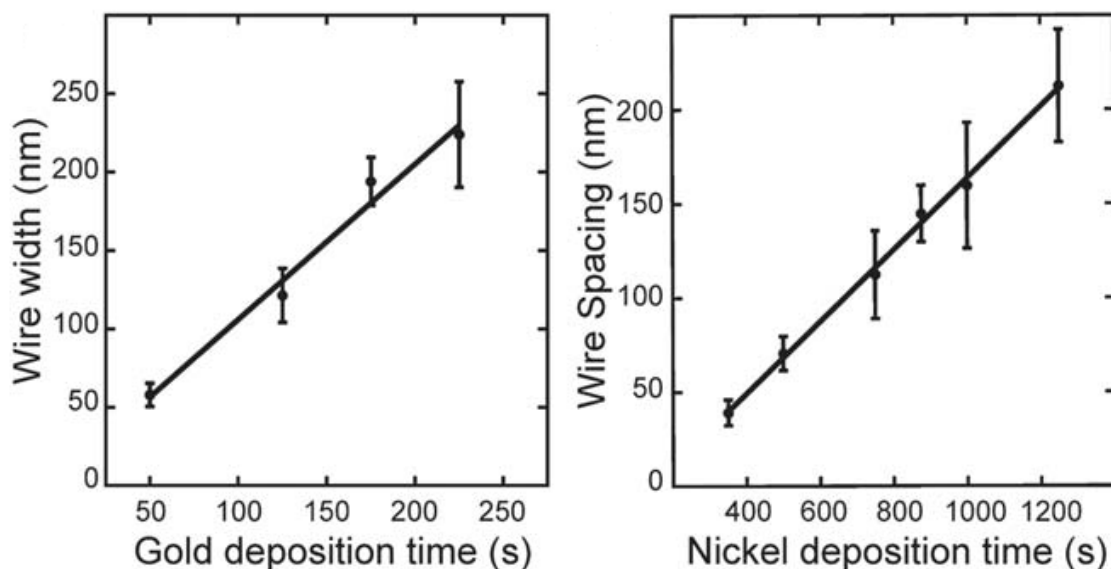
After the realization that the HDLPNE method can produce adjacent Au nanowires with well defined edges and pitch, the next step was to confirm that this method can create not just two Au nanowires at small pitch, but that the number of nanowires is tunable depending on how many times the alternating Au-Ni electrodepositions occur. What I proceeded to do was attempt to make different numbers of nanowires in the arrays; arrays of two, three, four, and five Au nanowires are shown in Figure 3.6.





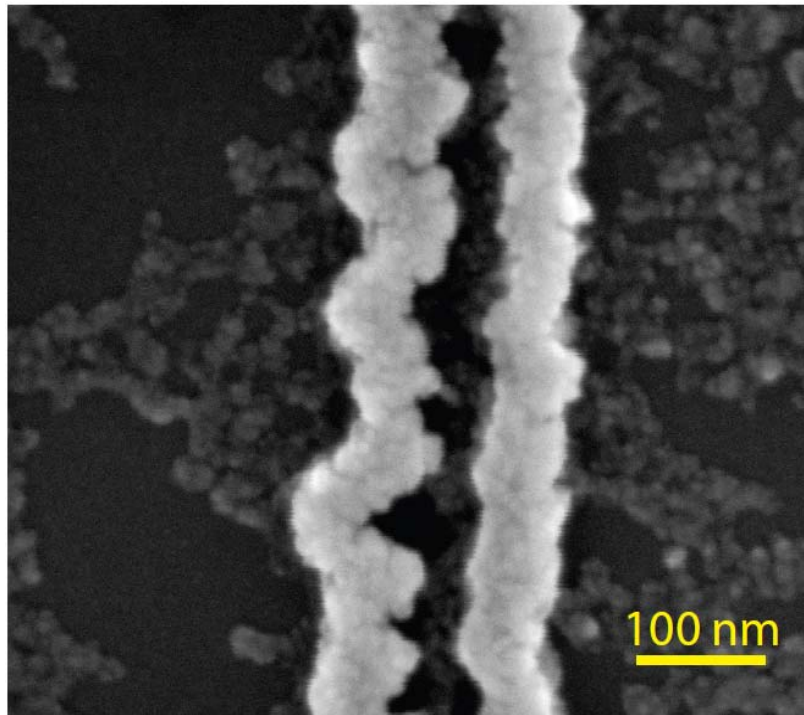
**FIGURE 3.6-** The ability to create a variety of pitch and nanowire width using HDLPNE. (a) Two 100-nm Au nanowires with pitch of 75 nm. (b) Three-100 nm Au nanowires with pitch of 100 nm. (c) Four-75 nm Au nanowires with pitch of 250 nm. (d) Five-100 nm Au nanowires with pitch of 100 nm.

Figure 3.5 also shows the ability of the HDLPNE method to tune the pitch of the overall system from 75-250 nm. This is because the Ni electrodeposition width is a function of time and because the width of the Ni determines the pitch, the wire spacing or pitch itself is a function of Ni electrodeposition time as can be seen in Figure 3.7a. The Au nanowire width is also a function of electrodeposition time and is independent of Ni electrodeposition as seen in Figure 3.7b.



**Figure 3.7-** Functional relationships resulting from HDLPNE. (a) Dependence of gold nanowire width on gold electrodeposition time. (b) Dependence of gold nanowire spacing or pitch on nickel electrodeposition time. The error bars refer to one standard deviation in the width across multiple LPNE samples.

Figure 3.7b demonstrates the ability of the HDLPNE to produce an array with a pitch as small as 50nm, and example of which can be seen in Figure 3.8.



**Figure 3.8-** High resolution SEM image of two gold nanowires with approximately 60 nm in width separated by an average of 40 nm.

With the result that I could now create nanowire pitch and width at will, I wanted to confirm that different shapes of high density arrays could also be created via HDLPNE as was shown in the original work on LPNE. Plasmonic lenses for the use of lithography, typically a circular shape, have

been a subject of recent study to reduce feature sizes [89-95]. I therefore decided that a high density circle would be a good starting point to confirm that HDLPNE can be performed on different shapes. After designing a photomask with a circle of radius 5 $\mu$ m, I proceeded to follow the HDLPNE method just as I would for a straight line exposure mask. The successful result of this experiment is demonstrated in Figure 3.9.

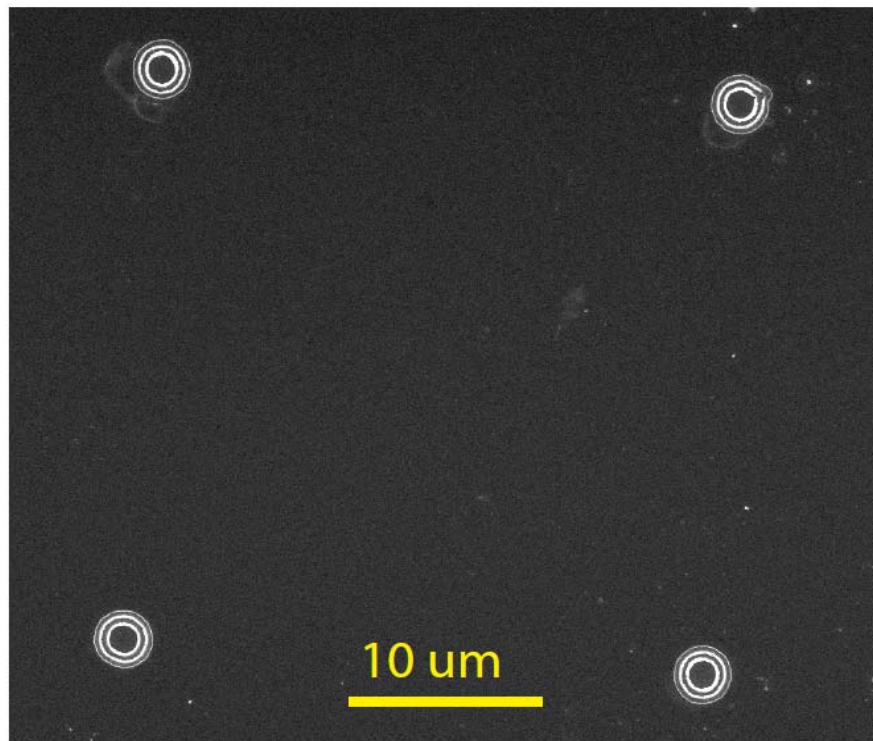


**Figure 3.9-** Low resolution SEM image showing the ability to adapt HDLPNE to create a plasmonic lens type structure.

My next investigation was into confirming that HDLPNE provides the ability to create Au nanowires at different widths with different pitch because the Au nanowire width and the distance between adjacent Au nanowires

should be independent of one another. I created samples that should display this behavior and further examined under SEM- the results of this successful attempt are shown in Figure 3.10.

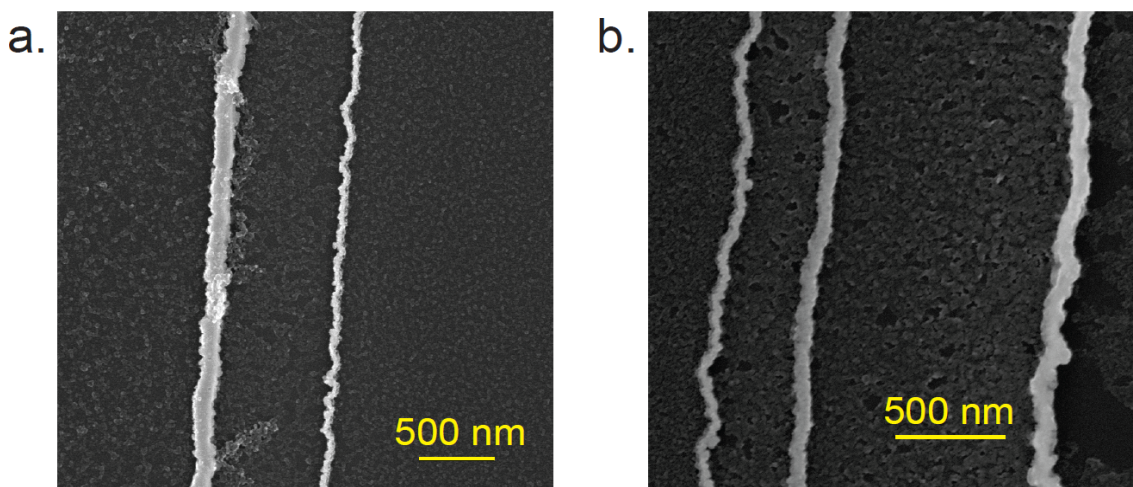


**Figure 3.10-** The ability to create nanowire width and pitch independent of one another in the same array. (a) Two gold nanowires approximately 500 nm apart, with widths of 200 (left) and 100 nm (right). (b) An array of three gold nanowires with widths of 80 (left), 120 (center), and 170 nm (right) separated by 350 nm (left to center) and 750 nm (center to right).

It is a compelling result that the HDLPNE method has appeared to be successful in creating nanowires with pitch down to 50nm as well as the pitch and nanowire size are independent of one another but I still need to confirm if these variables are consistent throughout the sample. To test this I will need to investigate in the SEM for consistent pitch and nanowire width from top-to-bottom and from side-to-side in the entire array. The results of the top-to-bottom investigation, illustrated in Figure 3.11, exhibit the

capability of the HDLPNE to allow for excellent pitch control over a long length giving confidence that the pitch is consistent up and down the entire array.

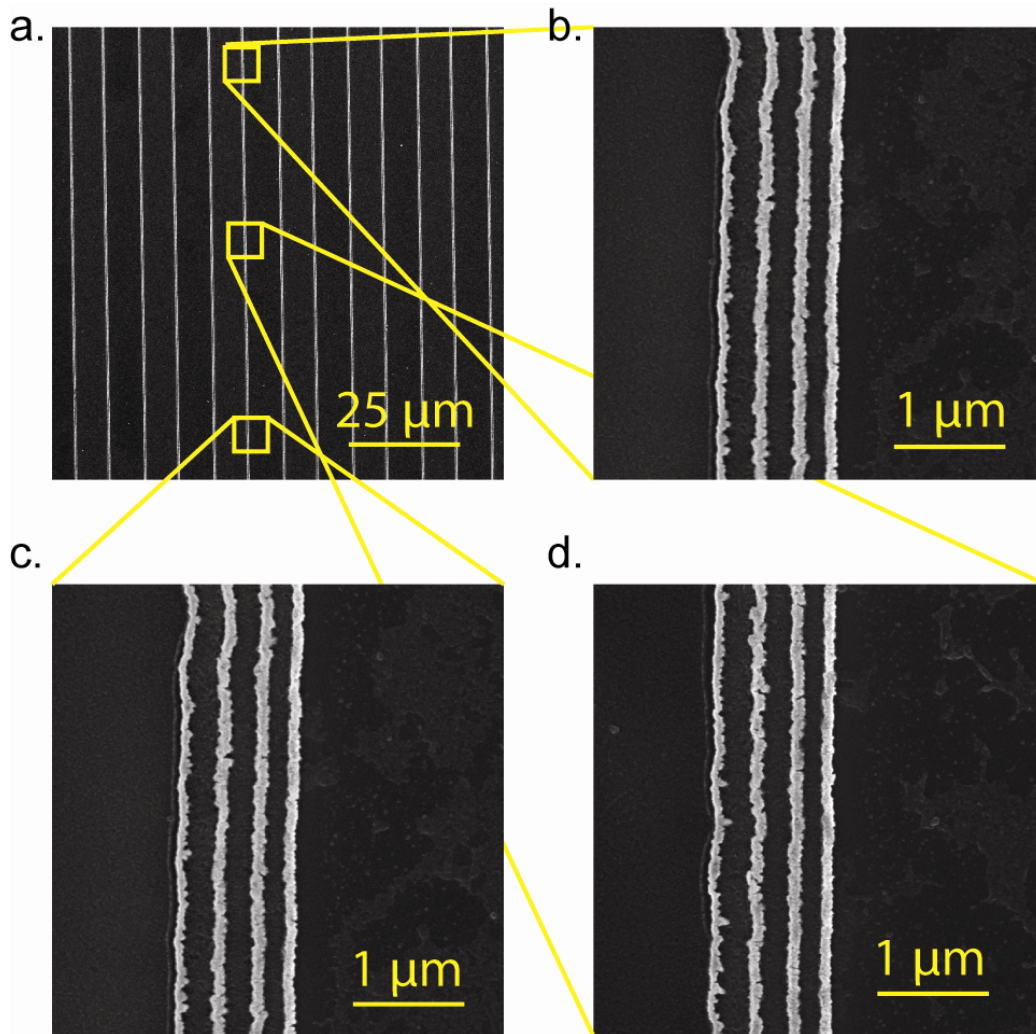


**Figure 3.11-** Consistent pitch from top-to-bottom (a) Low-magnification SEM image displaying 13 high density Au nanowire arrays. (b-d) High-magnification SEM images along 1 array exhibiting excellent pitch control over long array lengths.



The investigation into the side-by-side consistency of pitch and nanowire width also yields confidence that each adjacent array has the same pitch and gold nanowire width as the array before it- shown in Figure 3.12.

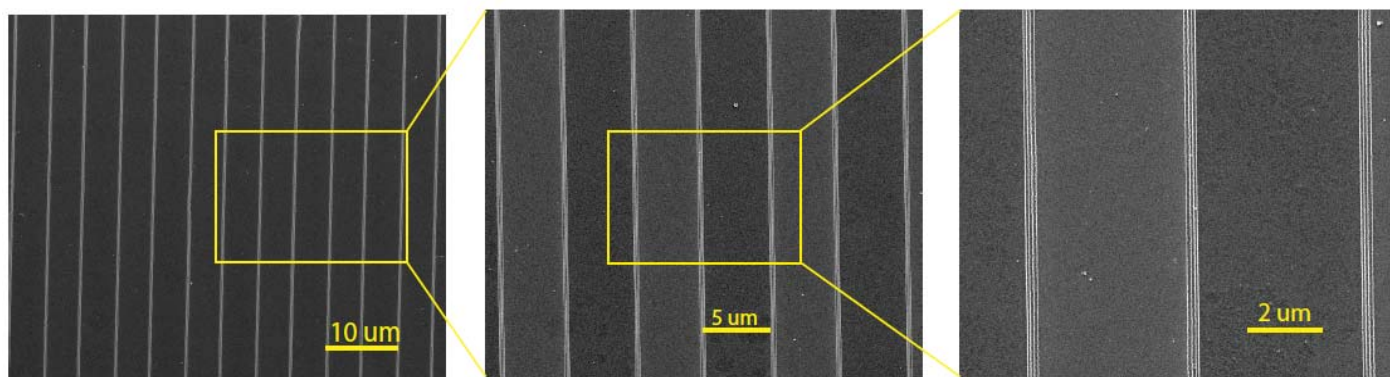


**Figure 3.12-** Side-by-side comparison of nanowire width and pitch. Left- Low-magnification SEM image displaying 18 high density gold nanowire arrays; Center- Low-magnification SEM image displaying 8 high density gold nanowire arrays; Right- SEM image displaying 3 high density gold nanowire arrays which have pitch comparable to adjacent high density arrays.

As a result of Figures 3.6, 3.7, and 3.10-3.12, I came to the conclusion that the HDLPNE method can create nanowire arrays with tunable pitch and gold nanowire widths, and that these variables are consistent from top-to-bottom and side-to-side. This ability should be transferrable to nanowires other than gold and could therefore be applied to improve the number of working devices in a given area for devices which have already been constructed with traditional LPNE. Additionally as it applies to creating solar devices HDLPNE has illustrated the ability to create systems in the realm

required for taking advantage of leaky-mode and plasmon resonances-pitches as small as 100nm but tunable up to 500nm.

A further conclusion is that the pitch of Au nanowires are no longer limited by the diffraction of light as can be realized by the fact that our pitch can be reduced to 50 nm compared to the theoretical limit would be 450 nm; I have fundamentally created a new type of lithography with the HDLPNE method where the pitch is determined by electrodeposition time.

### **3.4 Characterization**

Knowing that HDLPNE allows for tunable pitch and is consistent across the sample is only a benefit if the created nanowires have properties similar to other nanowires of the same type. As a consequence I proceeded to investigate the resistance of the gold nanowires in a single high density array created by HDLPNE to confirm that my gold nanowires were for one, continuous nanowires usable in a device, but secondly that the gold nanowires had resistance comparable to other gold nanowires [56, 96]. Post processing of a single array consisting of three gold nanowires allowed for a two probe current-voltage measurement yielding the results shown in Figure 3.13.

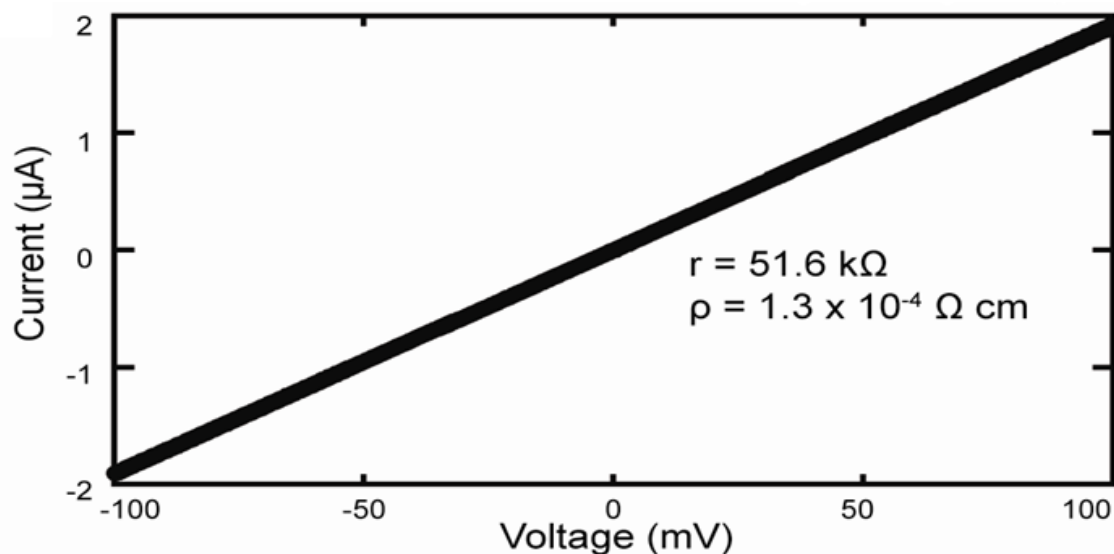


**Figure 3.13-** Current-versus-voltage curve for a high-density 3 gold wire array, with a resistance of  $51.6 \text{ k}\Omega$  and a resistivity of  $1.3 \times 10^{-4} \text{ }\Omega \text{ cm}$ .

The next investigation was to confirm the heights of the individual nanowires in a high density array were consistent from wire to wire. An atomic force microscope (AFM) was employed to obtain the height profile of the individual nanowires in an array. The corresponding AFM image and histogram showing consistent heights between nanowires in a high density array are displayed in Figure 3.14.



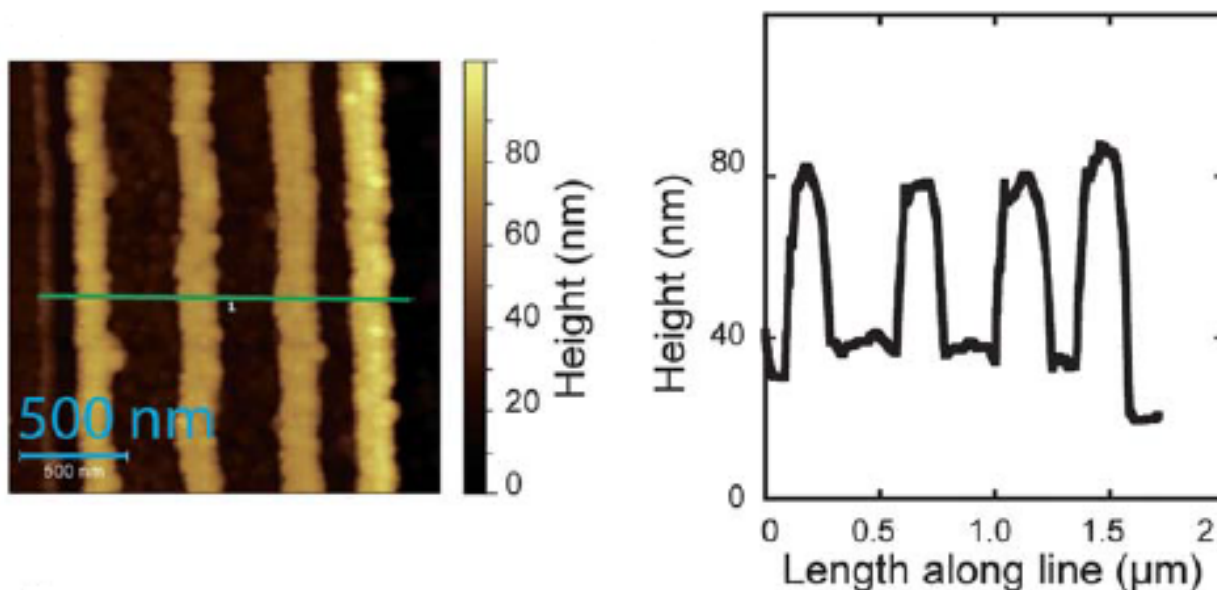


**Figure 3.14-** left; AFM image of 4 gold nanowires, right; Linescan across 4 nanowires shown in left image.

As it relates to a potential solar cell being fabricated from LPNE, I can now be confident that the HDLPNE method does not affect the height of the individual nanowires in a high density array and therefore the thickness of the solar cell should be consistent.

It can be seen in nearly all of the imaged arrays that there is a notable curvature to the nanowires in the high density array. To investigate this HDLPNE was performed on TEM grids from Ted Pella, just as in the traditional LPNE method, and imaged in FEI Tecnai 12 TEM at UC Berkeley's electron microscopy lab. Figure 3.15a displays a TEM image of a nickel electrode after a gold nanowire and nickel spacer have been electrodeposited. As evident from the image, the electrodeposited material is

nanocrystalline; however the nanocrystals are dense and uniform. Furthermore there is a clear definition between the evaporated nickel film and gold nanowire, as well as the gold nanowire and adjacent nickel spacer. This result gives confidence that there is no diffusion or alloying between the gold and nickel depositions. The nanocrystallinity and lack of alloying is evidenced by the electron diffraction shown inset of Figure 3.15a, where every ring is indexed to either pure gold (JCPDS 19-629) or pure nickel (JCPDS 87-0712).

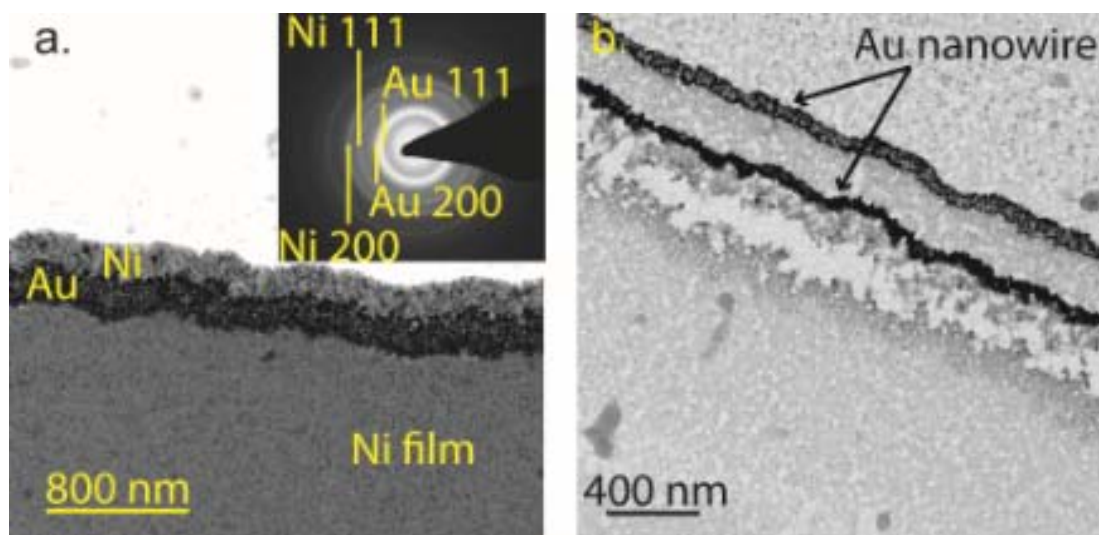


**Figure 3.15-** TEM analysis on HDLPNE nanowires. (a) TEM image after electrodeposition of 1 gold nanowire followed by 1 nickel spacer. Inset- SAED showing nanocrystalline nature and lack of alloying after gold and nickel deposition. (b) TEM image of two 50 nm wide gold nanowires with pitch of 200 nm.

More importantly Figure 3.15 demonstrates a limitation to both the LPNE and HDLPNE methods- the electrodeposited nanowire maintains a

relatively constant width along its length, but the overall straightness is governed by the straightness of the initial nickel edge. As can be seen in Figure 3.15a, the subsequent gold nanowire and nickel spacer electrodeposits follow the same path set by the initial nickel edge. Figure 3.15b shows a TEM micrograph of two parallel gold nanowires approximately 50 nm in diameter and separated by approximately 200 nm. This image not only displays the nanocrystalline nature of the nanowires occurring in all wires synthesized, but that the curvature from the nickel edge is maintained across the array.

The issue of curvature as it relates to nanowires of LPNE can potentially be corrected by the already developed self-perfection by liquefaction (SPEL) technique [97]. This technique has proven successful in reducing nanowire roughness after fabrication by as much as 73% as evidenced by results of a method very similar to LPNE known as the PENCiL method [98, 99]. While SPEL has not yet been attempted on traditional LPNE or HDLPNE arrays, it is suggested that this or other such methods be attempted in the future to address the curvature of the nanowire arrays. By assembling arrays with minimal curvature this will allow for optimal control over the leaky-mode and plasmon resonance, thereby allowing a more robust method for studying their effects.

With the discovery that I can in fact tweak the LPNE method so that the pitch is no longer a function of photolithography but instead electrodeposition time, I now have made the ability to create systems with pitch in the regime necessary to allow for leaky-mode and plasmon resonances. As a byproduct, HDLPNE can also provide for an increased surface density of nanowires that act as full functioning devices compared to traditional LPNE. This ability yields me the necessary assurance to proceed to investigate how an LPNE solar cell changes when HDLPNE is employed.

## **Chapter 4**

### **PbSe Nanowire Solar Cells**

#### **4.1. Au-PbSe core-shell via Coaxial LPNE**

The goal of this chapter will be to portray how I have successfully fabricated PbSe solar cells in my lab via LPNE and how HDLPNE can potentially improve the efficiency as well as reduce cost. Additionally I will present a factor limiting the efficiency of nanowire devices, including my solar cells, and how I have begun working on how to eliminate this limitation.

To begin the solar portion of my dissertation we must revisit the bottom-up solar cell structure shown in Figure 1.2 from Chapter 1. To construct a solar cell with this bottom-up approach, I will use an innovative modification to LPNE, coaxial LPNE; a method initiated in collaboration with my colleague Somnath Ghosh [100]. The motivation behind a coaxial structure is the evidence illustrating its ability to improve carrier collection and efficiency when compared to the like bulk semiconductor itself [21-24]. Coaxial LPNE, as illustrated in Figure 4.1, employs an array of gold core nanowires, created by following the standard LPNE method, to act as a nanoelectrode upon which a semiconductor electrochemical reduction can

take place. The gold nanoelectrodes require structural support after completion of step 7 to assist in adhesion to the substrate upon which electrodeposition of the semiconductor shell layer takes place; this support is provided by the PVD nickel film at the top portion of the substrate as displayed in Figure 4.1.

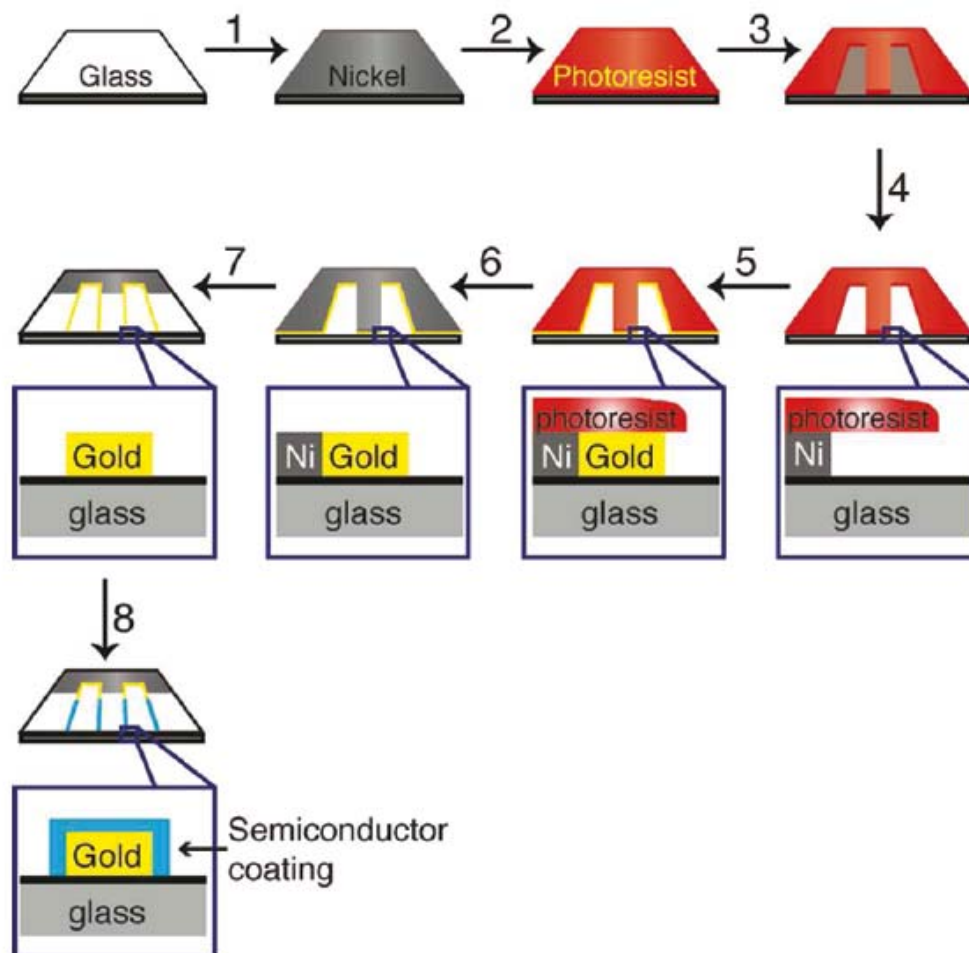


**Figure 4.1-** The coaxial LPNE process flow to create a core-shell structure.

To create a PbSe nanowire based solar cell derived from coaxial LPNE will first require the ability to create a Au-PbSe, core-shell structure, and the successful characterization of this structure. To investigate the capacity to do such, I initially studied the cyclic voltammogram of PbSe, shown in Figure 4.2, where an array of gold nanowires serves as the working electrode in the electrochemical cell to determine a potential range where PbSe could be electrodeposited on the gold nanowires.

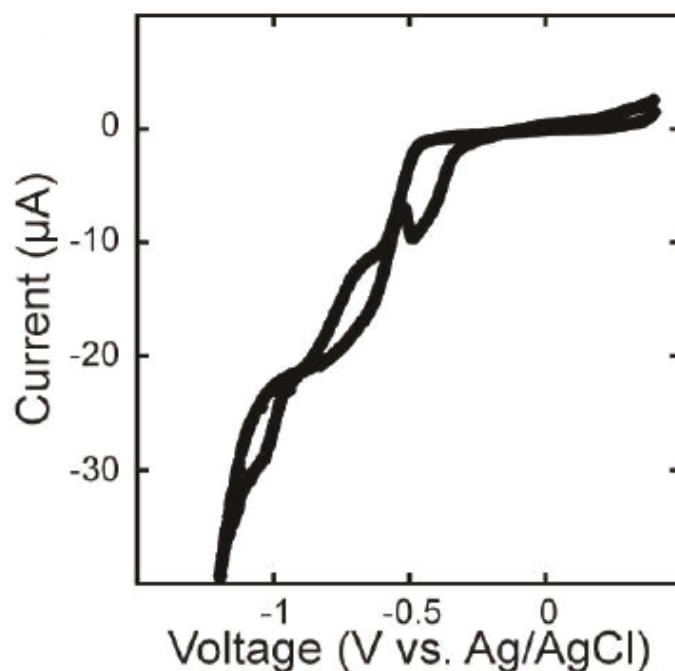


**Figure 4.2-** CV of the PbSe electrodeposition with gold nanowires acting as the working electrode.

Utilizing an electrodeposition bath with identical composition of that used for PbSe nanowires from chapter two, it is evident that the broad peak

between -0.5 and -1.0 V vs Ag/AgCl corresponds to the codeposition of lead and selenium on the gold nanoelectrodes, while potentials negative of this correspond to onset of hydrogen evolution. It was then hypothesized to electrodeposit PbSe on the gold nanowires at a potential of -0.6 V vs Ag/AgCl to allow for good kinetic control while still depositing at a reasonable rate. The result of such an attempt is displayed in the SEM image in Figure 4.3, where a single 100 nm wide gold nanowire has been evenly coated with approximately 200 nm of PbSe.

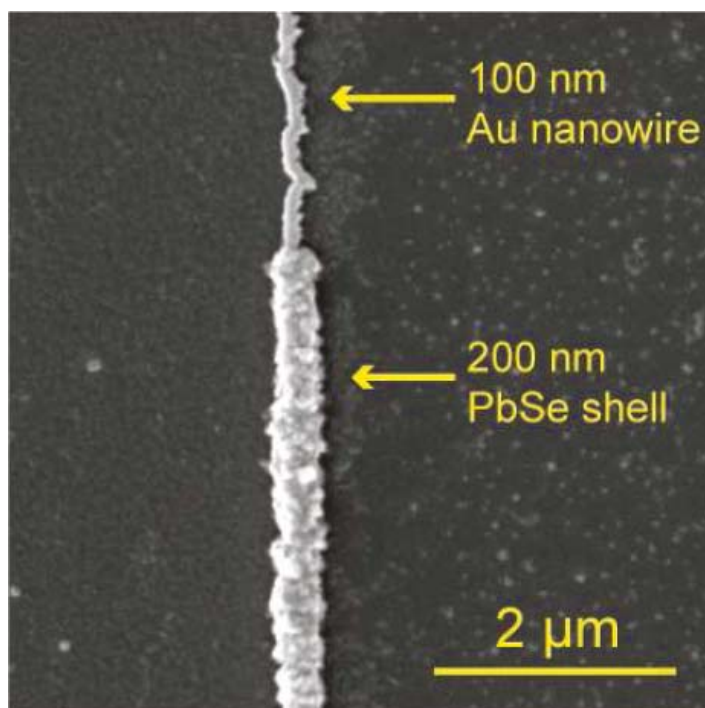


**Figure 4.3-** SEM image showing a 100 nm gold nanowire with a 200 nm PbSe shell; created by using coaxial LPNE.



## 4.2 Characterization

Upon the realization that the coaxial LPNE method emerged successful it was necessary to confirm the presence of the Au-PbSe structure and composition. Verification of the composition and structures were confirmed with the same tools as for the PbSe nanowires- EDX, XRD, and TEM/SAED.

An EDX of a single Au-PbSe nanowire like that from Figure 4.3 was obtained with corresponding results displayed in Figure 4.4. Because a gold core is assumed, the EDX analysis was focused on the PbSe shell layer which yielded a ratio of 1:1 for Pb:Se, permitting confidence that PbSe is in fact the shell layer.

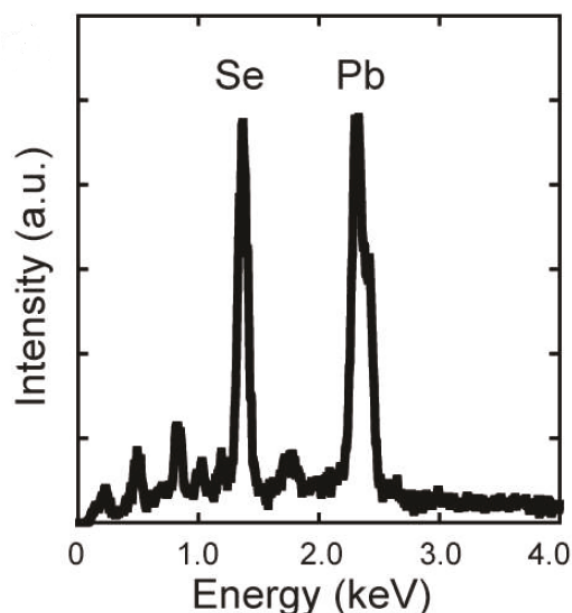


**Figure 4.4-** EDX spectra of a PbSe-coated gold nanowire showing the presence of both lead and selenium.

Upon confirmation of the correct stoichiometric ratio, the structural makeup of the electrodeposit was the next area of study. The XRD of an array of Au-PbSe nanowires was obtained with the resulting pattern shown in Figure 4.5. The pattern from the nanowire arrays confirm the presence of both gold and lead selenide, but just as important, the lack of any Pb, Se or alloying of the metal-semiconductor interface.

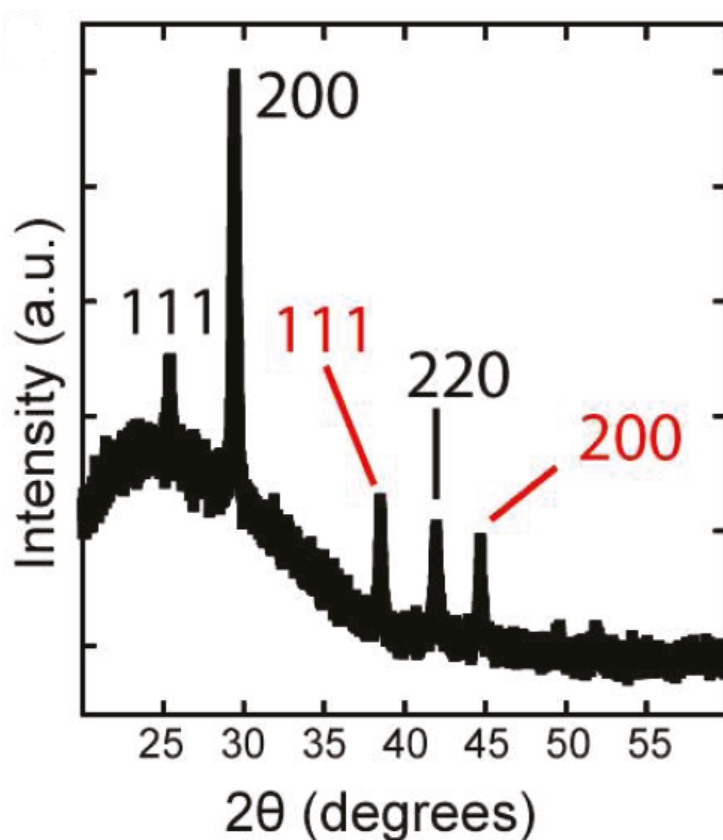


**Figure 4.5-** XRD spectrum of a PbSe-coated gold nanowire with the 111, 200 peaks of gold (red labels) and the 112, 200, and 220 peaks of PbSe (black labels) identified.

Additional confirmation of the structural makeup was acquired from a SAED of a single coaxial nanowire, presented in Figure 4.6, which shows the presence of Au and PbSe but also lacks ring patterns which would correspond to Pb, Se, and any metal-semiconducting interface.

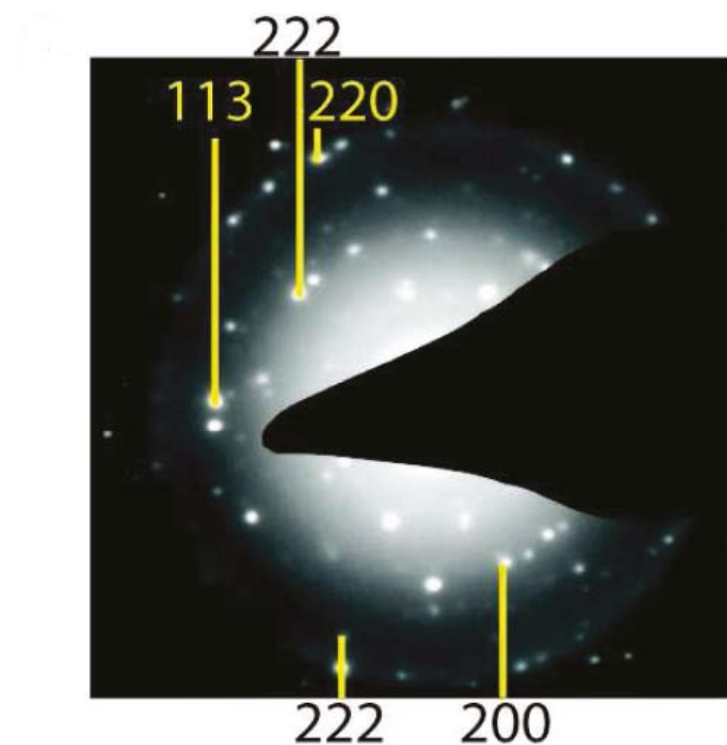


**Figure 4.6-** SAED image of a PbSe-coated gold nanowire with the 200, and 222 peaks of gold (yellow text) and the 222, 113, and 220 peaks of PbSe labeled (black text).

In conjunction with the results from the EDX, XRD, and SAED, I can now come to the conclusion that I have successfully electrodeposited PbSe as a shell on top of a gold core nanowire. The next step taken was to

determine if the shell layer distributes evenly on the gold core. To examine this distribution of the shell layer, the TEM was employed to acquire high-resolution images, an example of which is displayed in Figure 4.7.

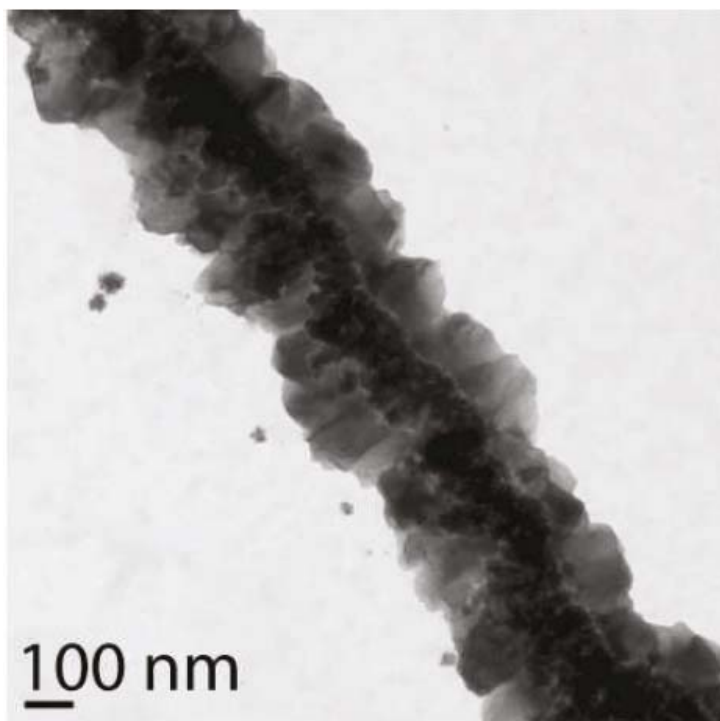


**Figure 4.7-** TEM image of a PbSe-coated gold nanowire.

Figure 4.7 illustrates four key properties about the core-shell system created by coaxial LPNE that are beneficial to a solar cell via coaxial LPNE. First, the Au-PbSe interface is sharp, leading to the conclusion, concurring with previous characterization tools, that there is no alloy at the metal-semiconductor interface. Second, the even distribution of the semiconducting shell around the gold core yields the confidence that there will be no shorting between the inner gold core to other layers in the device;

the even distribution also exhibits that the potential used for the PbSe shell is sufficient to control the deposition process. Third, the grain size in the PbSe shell is much larger than the inner gold core grain size; this can be confirmed by the SAED from Figure 4.6, where the gold core appears as rings in agreement with the nanocrystalline nature from the TEM image, while the PbSe shell appears as individual spots, representing fewer and larger grains. Fourth, all PbSe grains are aligned axially, with respect to the gold core, which will lead to improved e-h separation and transport, as opposed to the randomly oriented grains displayed in stand alone, single PbSe nanowire from Figure 2.18. This arrangement of the PbSe grains in the coaxial nanowire has the potential of leading to a more efficient device.

Once all material characterization had been completed on the Au-PbSe structure, the ability to independently control the dimensions as in LPNE was the next route explored. The length of the coaxial wire will still be controlled by photolithography. Based on the TEM image in Figure 4.7 demonstrating an even width of the shell relative to the gold core, it would be reasonable to assume the height of the wire will also be distributed in a manner equivalent to the width of the shell. This then leads to the fact that the width of the shell should be a function of electrodeposition time, just as in the standard LPNE method. The calibration curves for the width dependency of PbSe shell for differing gold core widths as a function of electrodeposition time,

displayed in Figure 4.8, shows an increasing rate of deposition as the gold core width increases. The increased slope of the curves as the gold core width increases can be attributed to the decreased resistance of the gold core by the following relationship:

$$R = \rho * L / A$$

Where the resistance,  $R$ , will decrease with an increasing area of the nanowire,  $A$ , assuming the resistivity,  $\rho$ , and length,  $L$ , are kept assumed unchanged.

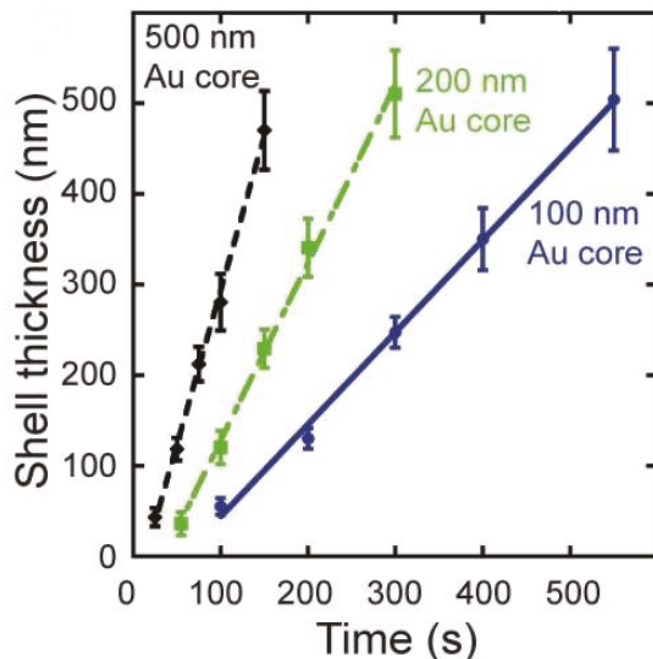


**Figure 4.8-** Calibration curve relating the PbSe shell thickness to electrodeposition time and the gold nanowire width.

To turn this Au-PbSe coaxial nanowire into a usable solar cell is still not a routine task even though I can create a coaxial structure. If these coaxial nanowires are to act as solar cells they need to be able to demonstrate the ability to absorb light. Figure 4.9 shows an I-V curve over a potential range of -2 to +2 V for an array of PbSe-coated gold nanowires in the dark (black curve) and exposed to white light (green curve), using a Hg ARC lamp, with an AM 1.5 filter. When the core-shell structure was exposed to light there was a measurable increase in conductivity in addition to Ohmic behavior, signifying good electrical contact to the gold core. The increase in

conductivity can be attributed to the fact that this coaxial array of Au-PbSe nanowires did respond to light exposure.

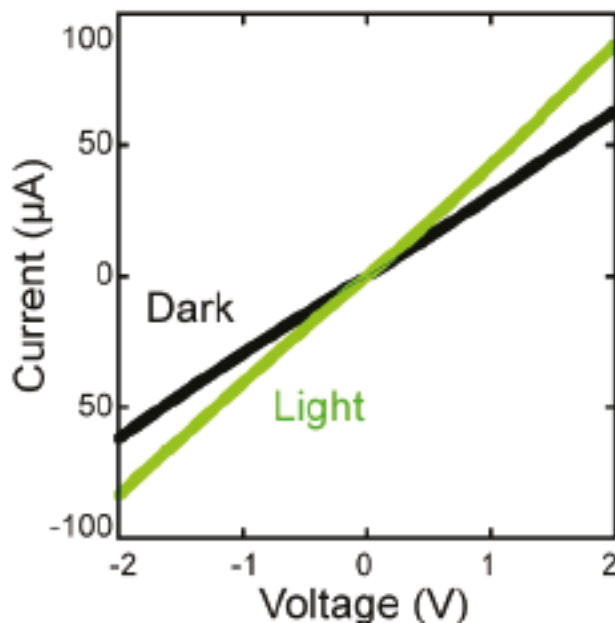


**Figure 4.9-** Light (green) and dark (black) IV curves of an array of 40 x 100 nm gold nanowires coated with 250 nm of PbSe.

To confirm the result that the nanowires do in fact absorb light as well as quantify the percentage of absorbed light, an experimental setup like that shown in Figure 4.10 was constructed. Au-PbSe nanowires, biased at 1 V, were turned 'on' and 'off' to white light via an optical chopper. Because the nanowires are not continuously exposed to light, as was the case for the measurement in Figure 4.9, but only exposed for half the experiment time as opposed to the previous experiment, it was assumed the signal would decrease and therefore a preamplifier was employed to amplify the signal.



What was viewed on the oscilloscope was an on/off signal from the reference, shown as blue in Figure 4.10, as well as an on/off signal from the coaxial nanowire array, shown as red in Figure 4.10.

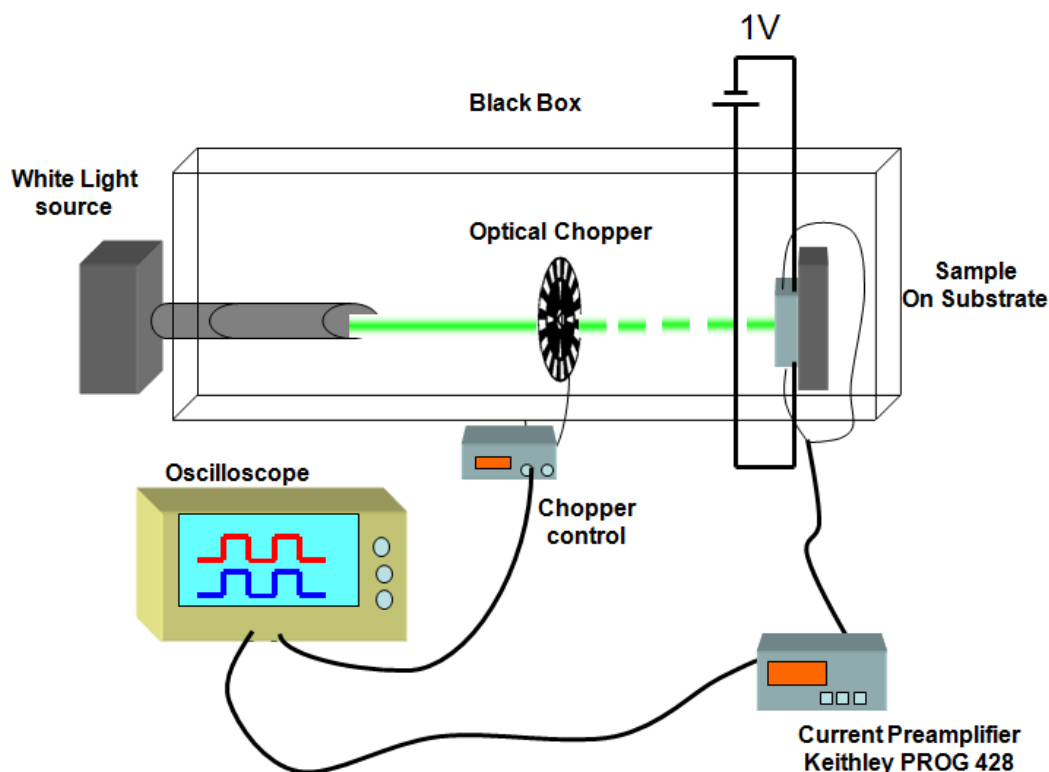


**Figure 4.10-** Experimental setup to test for coaxial nanowire ability to respond to an on-off input signal at a frequency determined by the optical chopper. The blue signal in the oscilloscope refers to the chopper frequency and the red signal in the oscilloscope corresponds to the nanowire signal.

It was first determined that if the signal frequency did not change with the reference frequency, the coaxial nanowire array did not respond to light. If however the signal frequency changed in step with a changing reference frequency, I was confident that I created coaxial nanowires which did in fact respond to light- this photoresponse is illustrated in Figure 4.11.

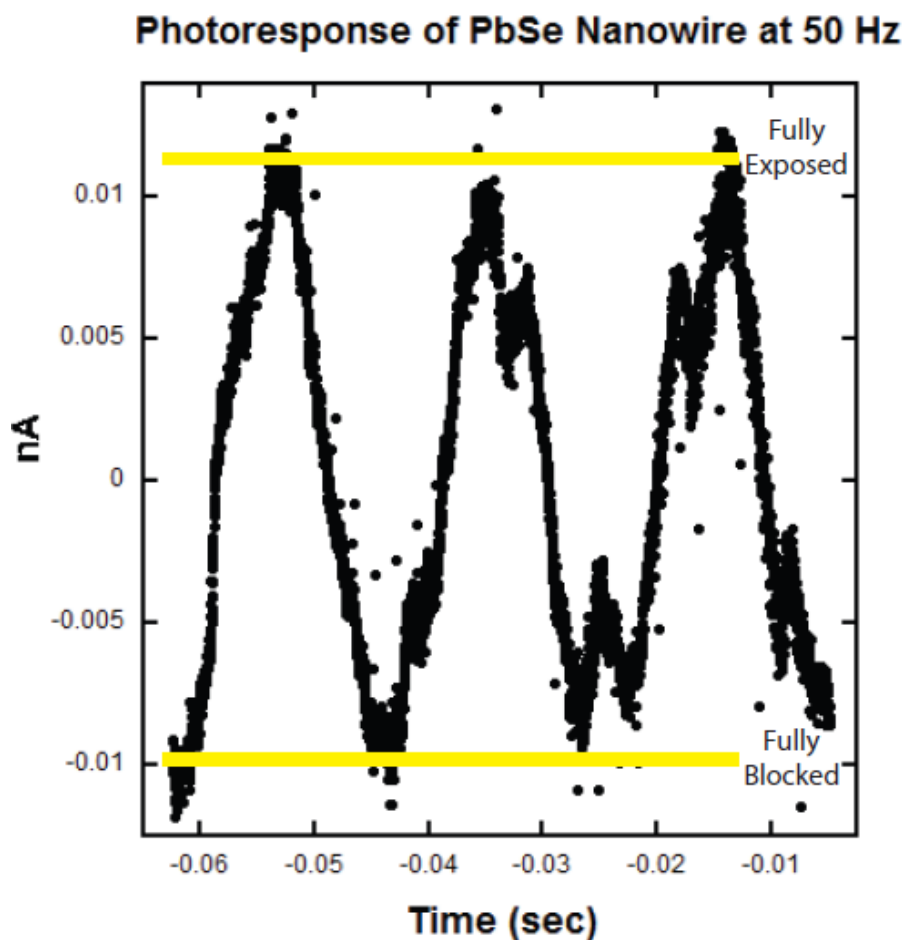


**Figure 4.11-** The photocurrent through an array of 40 x 100 nm gold nanowires coated with 250 nm of PbSe chopped at 50 Hz.

From Figure 4.11, I was able to quantify the number of light-induced charge carriers in the PbSe-gold coated nanowires by modifying the figure via introducing AM 1.5 filtration. By introducing this filtration I have effectively simulated the effects of 1 Sun illumination on the nanowire sample. Assuming that each photon absorbed generates one e-h pair, a reasonable assumption at a bias of 1 V, I calculate that only 9 out of 10,000 photons incident on the sample are absorbed by nanowires. However as only

3% of the sample area consists of the coaxial array, this correlates to approximately 4% of light incident on a nanowire being absorbed.

### **4.3 Preliminary Devices**

Having now successfully demonstrated a technique to build a photoresponsive device based on PbSe which can serve as a foundation in a bottom-up solar cell build via the coaxial LPNE method, the next logical step would be the creation of a single nanowire solar cell based on PbSe. However I would first need to look into the literature to discover previous, full-functioning devices, to mimic the structure of other PbSe based solar cell.

Reports on PbSe based solar cells are limited compared to standard Si, CdTe, CIGS, GaAs, or multi-junction cells. There is however a recent increase in the study of PbSe solar cells because of the properties discussed in Chapter 2 related to MEG, as well as the tunable  $E_g$  of PbSe resulting from its large exciton Bohr radius as the quantum confinement effects take place [101-105]. Harry Atwater's group has recently shown the ability to create a Schottky-type device based on ultrasmall quantum dots (QDs) with sizes as small as 1 nm [105]. His results agree with previous work on PbSe QD solar cells acting as a Schottky-type with comparable efficiencies [106,107]. One concern however regarding a Schottky device is that the structural design of

the cell limits the  $V_{oc}$  to  $E_g/2$  due to the Fermi level being fixed near the middle of  $E_g$  [108]. This limitation could limit the overall efficiency of the solar cell if this structure were chosen. I therefore continued to investigate other potential designs of the cell which could bypass the  $V_{oc}$  limit of Schottky devices (even though  $V_{oc}$  is not the main point of study of this dissertation, a structure which can still maximum  $V_{oc}$  is of interest). This lead to an excitonic solar cell structure of which there are a limited number of reports on excitonic solar cells based on PbSe [103,104]. An excitonic solar cell operates in a different manner than the traditional heterojunction solar cell where band bending limits  $V_{oc}$ . An excitonic solar cell can create a  $V_{oc}$  in excess of  $E_g/2$  and also creates and transfers charge simultaneously. As opposed to a traditional p-n junction solar cell where an electron-hole pair is created upon immediate light absorption, an excitonic solar cell produces a mobile excited state which causes dissociation of the electron into one phase of the device and the hole into another. While an excitonic solar cell would be an ideal structure because of its ability to create a large  $V_{oc}$ , I chose to create a Au/PbSe/SnO<sub>2</sub>/Al structure (a reasonable structure given the lab conditions) which could potentially act as either a traditional p-n junction device [109], or as an excitonic structure [103], where the actual process would need to be determined after more rigorous study.

I then proceeded to construct a low-density nanowire solar cell structure via traditional LPNE according to the illustration in Figure 4.12, as inspired from the literature, keeping in mind that photolithography limits the pitch and therefore this will both lack the effects of plasmons and LMRs as well as a large active area.

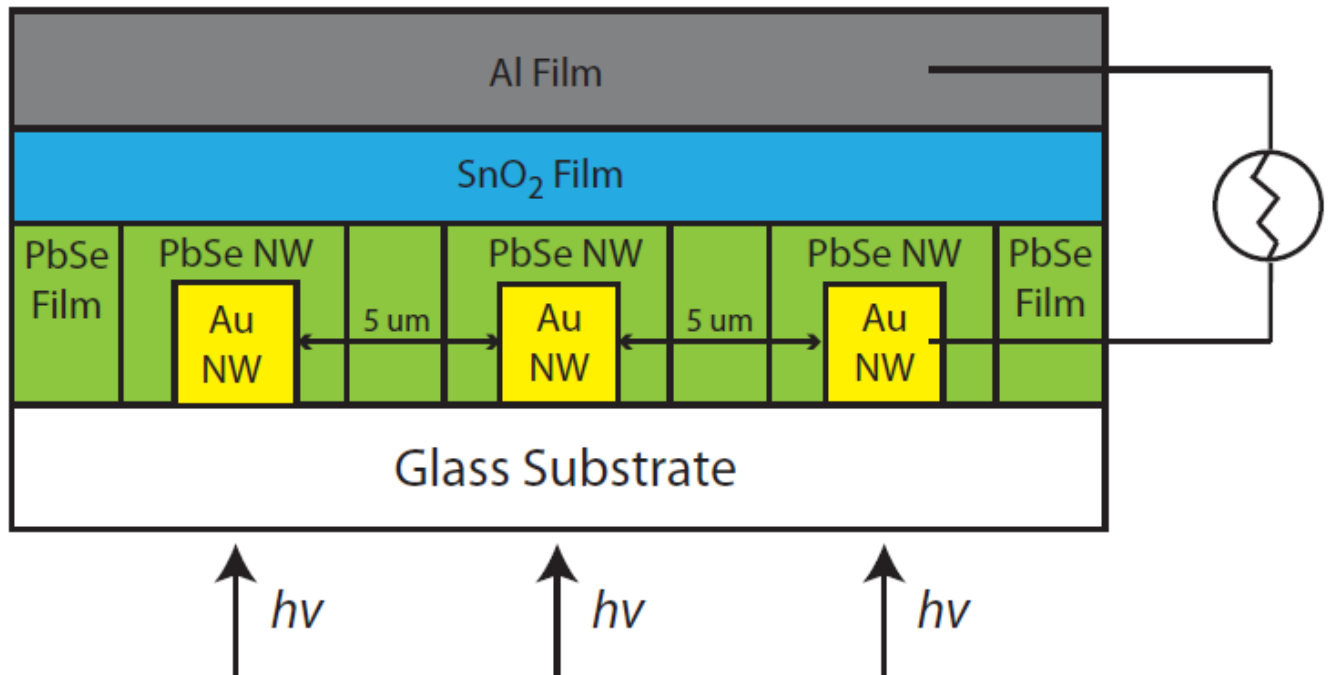


**Figure 4.12-** Proposed solar cell structure where pitch, and therefore device density, is determined by photolithography. The proposed solar cell operation under illumination can be pictorially referenced to Figure 1.2. It is proposed that under AM 1.5 illumination (shown as  $h\nu$ ), and after making silver contacts to the gold nanowires- as illustrated by the black line from the gold nanowires to the circuit, charge carriers will be created in the PbSe and transferred to the gold nanowires and tin oxide layer, the carriers will travel across the resistor, and then recombine.

The first step in constructing a solar cell according to Figure 4.12 is to utilize coaxial LPNE to create a gold core-lead selenide shell array. A thin film of PbSe, 10-20 nm, was then thermally evaporated on top of this Au-PbSe system to prevent shorting from the Au to the next layer of the cell, 60 nm of thermally evaporated SnO<sub>2</sub>. The cell was completed by thermal evaporation of 80 nm of Al to serve as the top contact of the bottom-up solar cell. The corresponding I-V curve for a solar cell with a 100 nm Au core and 250 nm PbSe shell with 5  $\mu$ m separation between Au cores is shown in Figure 4.13.

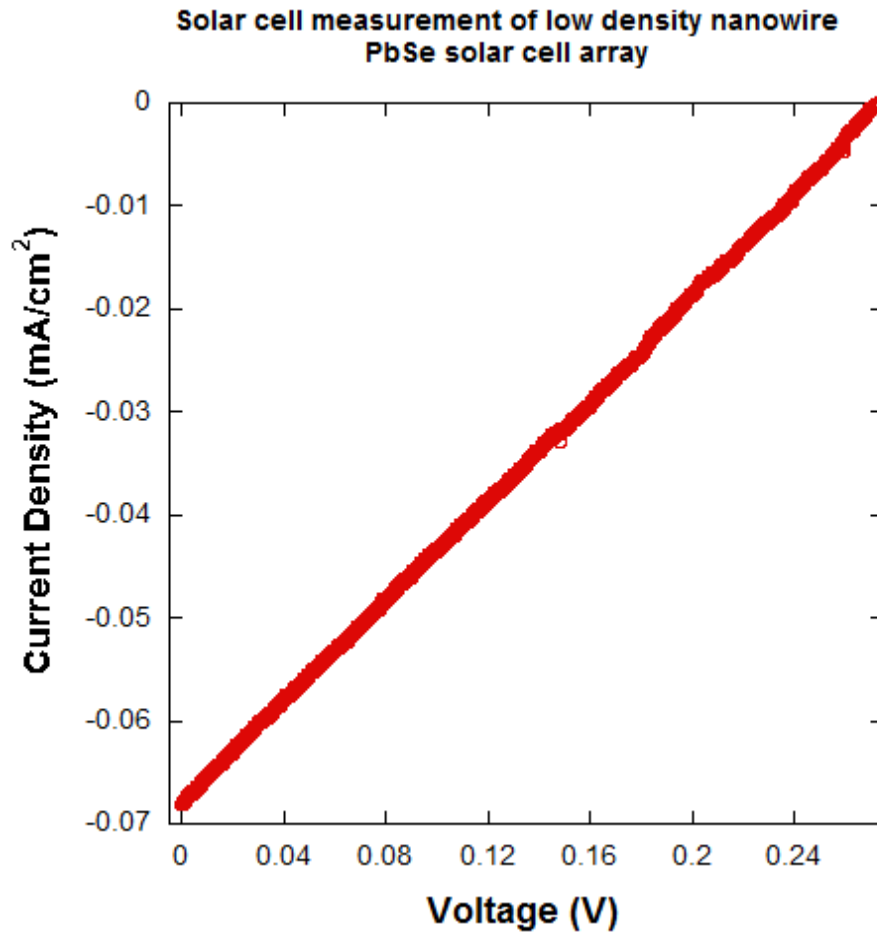


**Figure 4.13-** Solar cell curve for a solar cell based on using coaxial LPNE where the pitch is determined by photolithography; FF= 0.274,  $V_{oc}$ = 0.275 V,  $J_{sc}$ = 0.068 mA/cm<sup>2</sup>.

The average  $V_{oc}$  and FF for the low-density nanowire solar cell shown above under AM 1.5 illumination was 0.275 V and 0.274 respectively. The short-circuit current density for the device was 0.068 mA/cm<sup>2</sup> with an average maximum power of 0.42 uW. While the efficiency and results are hardly impressive, this was one of the first solar cells fabricated via LPNE.

and lends a foundation to study how HDLPNE can potentially improve these results.

To increase the overall efficiency of the device HDLPNE should be employed in conjunction with coaxial LPNE to create high density solar cells according to Figure 4.14 where the pitch is now a function of electrodeposition time. The high density solar cell will not only increase the surface density of the device, and hence the overall device efficiency, but also the potential to increase the efficiency per nanowire by taking advantage of the LMRs in the small pitch semiconductors and light trapping properties of the closely spaced Au cores as discussed in Chapter 1 to further increase  $J_{sc}$ .

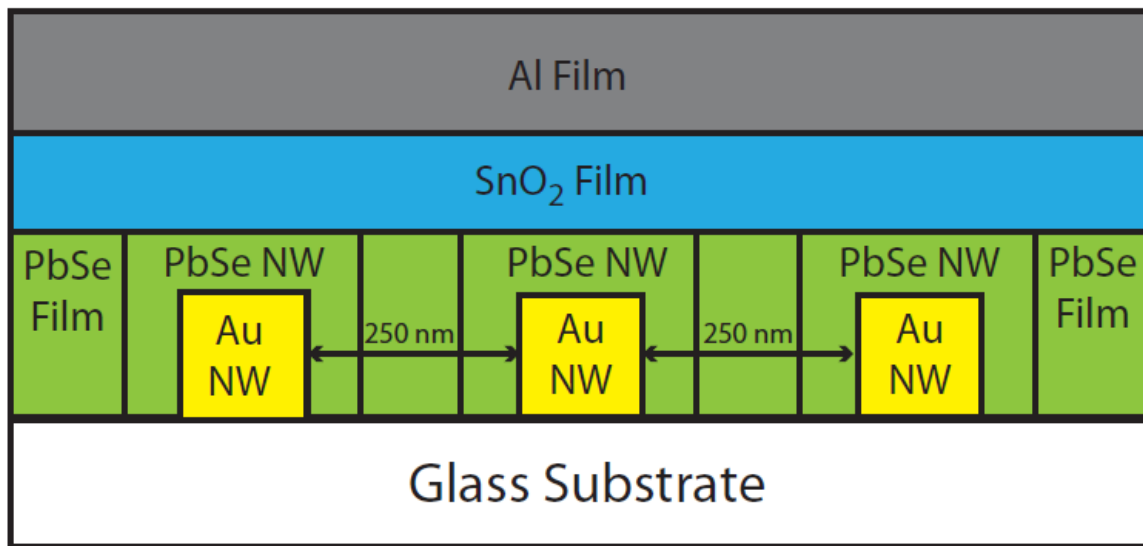


**Figure 4.14-** Proposed solar cell structure where pitch, and therefore device density, is determined by electrodeposition by using HDLPNE. The operation of this cell is identical to the operation shown in Figure 4.12 and is not shown for sake of redundancy.



To test this potential a high density area of four gold nanowires 100 nm wide were fabricated via HDLPNE and then encapsulated with approximately 250 nm of PbSe as illustrated in Figure 4.15 (It was important to compare apples-to-apples in this case as it relates to the nanowire size, as comparing the results of varying nanowire sizes cannot yield confident results as a change in nanowire size itself has the potential itself of affecting the device efficiency). The resulting array proceeded to have the same thin film deposition processes performed as in the low density nanowire solar cell device to complete device fabrication.

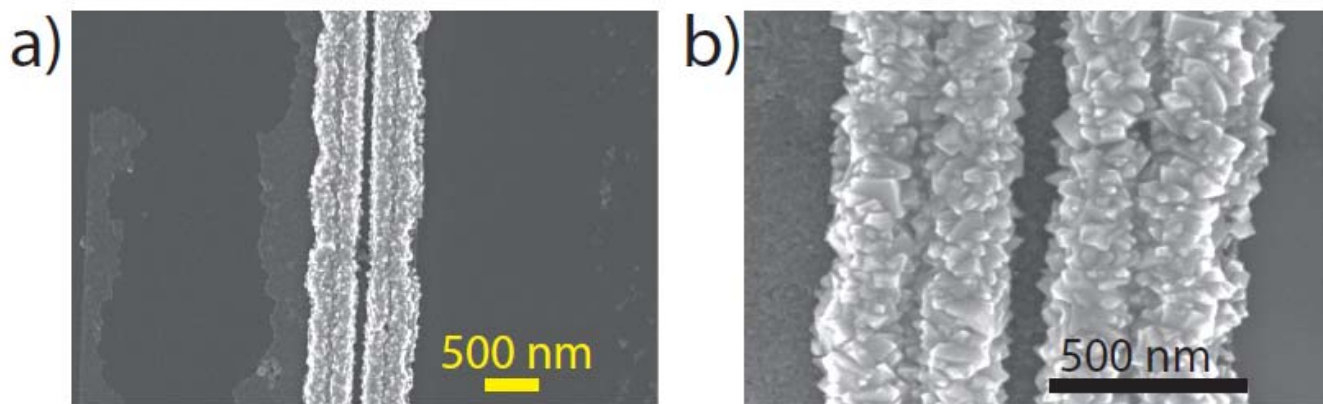


**Figure 4.15-** HD-Coaxial nanowire array for solar cell. (a) Low resolution SEM image showing the consistency of the PbSe on the gold core. (b) High resolution image showing the increased crystallinity and smooth deposit of 250 nm Pbse on the 100 nm gold cores.

Even though the number of nanowires has increased by a multiple of four compared to the low density nanowire device, assuming that each

nanowire in the high density device absorbs the same number of photons as the low density device,  $J_{sc}$  over the device should not change unless other phenomena are occurring. The I-V characteristics were measured for the high density device with the result displayed in Figure 4.16.

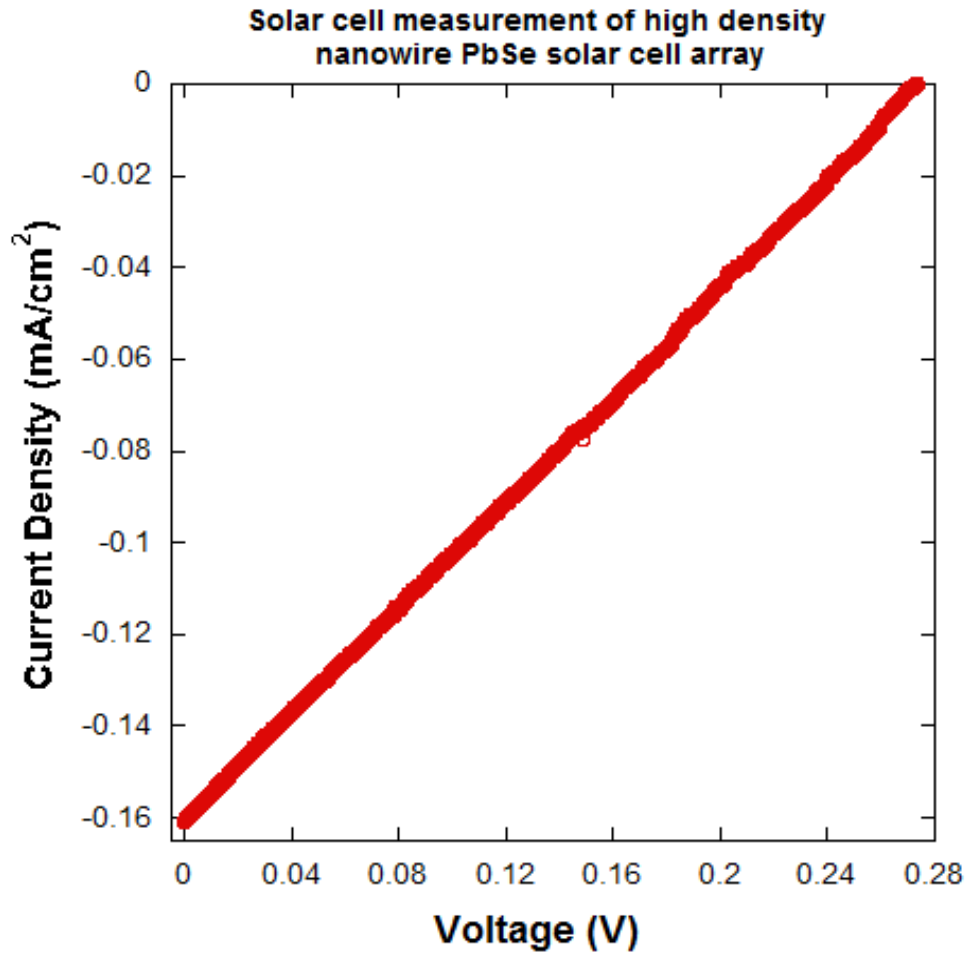


**Figure 4.16-** Solar cell curve for a solar cell based on using HD-coaxial LPNE in conjunction; FF= 0.278,  $V_{oc}$ = 0.279 V,  $J_{sc}$ = 0.160 mA/cm<sup>2</sup>.

The average  $V_{oc}$  and FF for the high density nanowire solar cell shown above under AM 1.5 illumination was 0.279 V and 0.278 respectively. The

results for  $V_{oc}$  and FF are consistent with the single nanowire device and provide additional confidence that a solar cell is in fact being constructed. The short-circuit current density for this device was  $0.160 \text{ mA/cm}^2$  with a maximum power of  $3.37 \text{ uW}$ .

The presence of each individual component of the cell was studied to determine if all components were in fact necessary. Table 4.1 illustrates that when either the PbSe or  $\text{SnO}_2$  is not included in the device, the cell will not operate properly. This leads to the conclusion that the device in fact needs to include all proposed synthesis processes.

Table 4.1- Comparison of current density,  $V_{oc}$  and FF by varying device structure

variation	FF	$V_{oc}$ (V)	$J_{sc}$ ( $\text{mA/cm}^2$ )
No PbSe	0	0	0
No $\text{SnO}_2$	0	0	0
LPNE	0.274	0.275	0.068
HDLPNE	0.278	0.279	0.160

Most importantly it can be seen that the short-circuit current density increased by a factor of 2.4 when comparing the  $J_{sc}$  in the low-density nanowire array to the HD array. By solely increasing the area of nanowire material it is intuitive to think that the current magnitude itself would

increase, but when normalizing to area, the current density would remain constant. Instead I see the current density is enhanced significantly. This enhancement could be explained by the idea of LMR and plasmons in the closely spaced semiconducting and metal nanowires.

While this enhancement most likely is a product of multiple phenomena, the results can be accounted for. One apparent explanation would be nanowire width varying from 10-15% as a function of the error bars; the wider core-shell structure would generate and extract additional photocarriers, thereby increasing the  $J_{sc}$ . Another term that could add to the enhancement could be explained by the variation in the height of the nanowires arrays. During the PVD process, the initial nickel film thickness varies, on average, between 5 and 10%. The thicker nanowires could also allow for additional light absorption and thereby increase the photocurrent. A final option, and believed to be a main contributor, is the trapping of light in the closely spaced Au core and the introduction of LMRs in the closely spaced PbSe semiconducting shell. There is also the potential of coupling LMRs when the semiconducting nanowires are closely spaced [33], on top of the interaction between plasmons and LMRs, both of which have yet to be experimentally investigated.

It is suggested that in depth study needs to be performed in the future to pin point how light trapping enhances  $J_{sc}$  as a function of the gold core

pitch and how LMRs affect  $J_{sc}$  as a function of the semiconducting shell pitch. Additionally repeated tests will need to be executed to provide results which can be statically more conclusive than the solar cells mentioned in this dissertation. However because of the large enhancement in  $J_{sc}$  when comparing the single nanowire device to the high density device, it would be hard to conclude that a portion of the enhancement is not due to light trapping from the small pitch gold cores or LMRs in the small pitch PbSe shells.

#### **4.4 Routes to improve device efficiency**

These solar cells at their present efficiencies will not help address the high cost of their respective product simply because their efficiencies are nowhere near respectable for commercial application. The cost to produce the device is very low based on the fabrication method; however the efficiency will need to be raised considerably to produce a cost efficient solar cell. An immense factor which limits the efficiency of my PbSe solar cells is the nanocrystallinity of the nanowires. As a result of an average grain size in the Au and PbSe nanowires ranging from 10-50 nm, there exists a high recombination rate compared to a crystalline silicon cell as seen earlier that only 4% of incident light induces current carriers. This increase can be realized as the number of recombination sites increases due to the increased number of adjacent grain boundaries which provide additional recombination

sites. Additionally nanowires created by LPNE have higher resistivity than their bulk counterparts, but not solely because of their smaller size, as this would simply cause a change in the resistance by a multiple. Instead, nanocrystalline nanowires created via LPNE typically have resistances which differ by to a larger extent as a result of scattering at the wire surface and grain boundaries [111-113]. As shown by electrical measurements on nanowires made by the Penner group via LPNE, surface and grain boundary scattering accounted for 5 and 65%, respectively, of the increased resistance when comparing to bulk measurements [53]. There is the also the presence of small gaps between some of the grains as can be seen by inspection of the TEM images of LPNE nanowires. This allows for potential oxide layers to form as well as introduces impurities into the overall device thereby reducing the overall quality and efficiency of any device fabricated by this LPNE and its derivatives.

The nanocrystallinity of nanowires from LPNE stems from the method by which they are electrodeposited. The electrodeposition method, overpotential deposition, is used to electrodeposit both the metal and semiconductor portions of the solar cell I previously discussed. Overpotential is the application of voltage significantly past, say 0.1 V and greater, than the necessary voltage for reduction to begin. Overpotential deposition results in a current density large enough that new grain growth is favored on

existing grains rather than continued growth of an already existing grain. This electrodeposition method results in new grains continually forming on grains which are present, hence the resulting nanocrystalline nanowires. The obvious question is why use overpotential deposition if it results in poor quality nanowires; because the large current density provided by overpotential deposition results in a device that can be deposited in less than five minutes. At this point I have reached a paradox; I want to create a device which is cost effective and efficient, but as a result of the cost effective method I have created a device which is inefficient. Suffice to say if solar cells, and other devices fabricated via LPNE, can be produced with an increased crystallinity, the result would be an increased efficiency due to a significant reduction in the aforementioned defects present in the nanocrystalline nanowires. This desire has led to collaboration with Professor John Stickney at the University of Georgia.

I am presently working with members of Stickney's group to use what is known as electrochemical atomic layer deposition (ECALD) to increase the crystallinity of LPNE nanowires [114-117]. Underpotential deposition, the electrodeposition method used by ECALD, is the formation of an atomic layer of one element on a second element at a potential less than that required to deposit the element on itself. Underpotential deposition (UPD) produces a current density on a level which promotes continued growth of an already

present crystal as opposed to new grain formation on present crystals as in overpotential deposition; put another way, the smaller current density prefers an intraelemental bonding. Deposition of layer-by-layer, or epitaxial growth, should result in nanowires that are single crystal or at the least a significant improvement of the crystallinity when compared to overpotential deposition of LPNE nanowires. This layer-by-layer growth via electrodeposition also potentially introduces its own paradox; by making high quality devices and improving the efficiency, the time required for deposition via ECALD may no longer result in a time efficient process; however this possibility can be determined at a later point in time. The ultimate goal of this collaboration would then be to create a solar cell which has all electrodepositions occurring via ECALD. However the first step is to investigate if ECALD is even possible on LPNE substrates.

One of Professor Stickney's students, Brian Perdue, is working on ECALD of CdTe and it was therefore decided that this would be the initial material to determine the viability of ECALD on LPNE substrates. CdTe ECALD studies have also been previously performed by Professor Stickney, as well as a number of other research groups, making the UPD of this material an excellent choice [118-120]. Samples were sent to the Stickney group that had completed steps 1-4 of the LPNE process to allow for UPD into the trench. The first step in this process was to choose what the UPD for



both components should be. To determine the UPD of each component, CVs of both the Cd and Te solution were performed, where the Te CV was done on the Ni film edge, and the Cd CV was done on UPD layer of Te- the corresponding CVs are shown in Figure 4.17 and 4.18. Te was chosen to deposit on the nickel film first because just as in bulk deposition, the more noble element, in this case Te, promotes UPD of Cd itself, thereby further CdTe epitaxial growth [121]. Not mentioned previously, but in the present appearing to be relevant, PbSe deposits in an identical manner; Se, as the more noble element, deposits first due to a smaller overdeposition potential, allowing for a UPD of Pb to occur leading to a successful codeposition even though bulk Pb has yet to be reached [122].

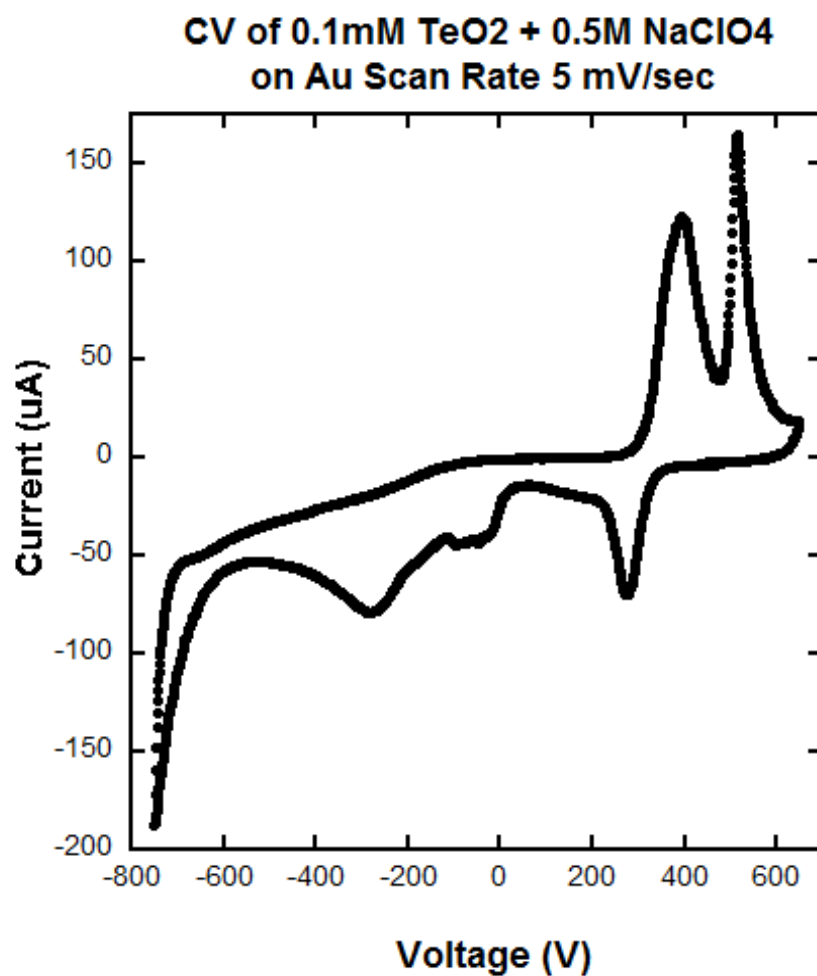


**Figure 4.17-** CV on nickel substrates provided to Stickney's group to determine optimal UPD of Te.

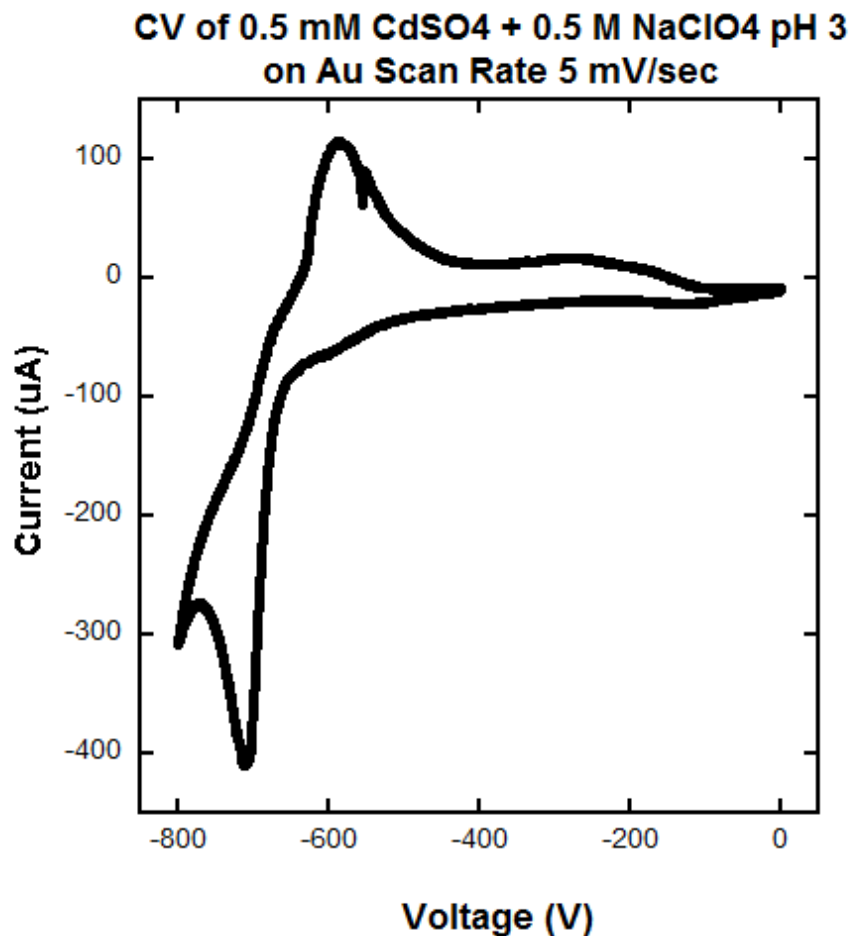


**Figure 4.18-** CV on nickel substrates provided to Stickney's group to determine optimal UPD of Cd.

It was established that the UPD for Te would be -0.2 V vs Ag/AgCl and Cd would be -0.55 V vs Ag/AgCl. Each UPD was held for 10 seconds, in between which a 10 second rinse was performed, followed by introduction of the precursor solution for 10 seconds. The height of the wire would still be a function of the nickel film height, but it is believed the width of the wire should now be a function of deposition cycles. After performing 100 UPD

cycles and completing the final PR strip and chemical etch, it was determined that ECALD was successful at electrodepositing nanowires using LPNE substrates as confirmed by the SEM images shown in Figure 4.19.

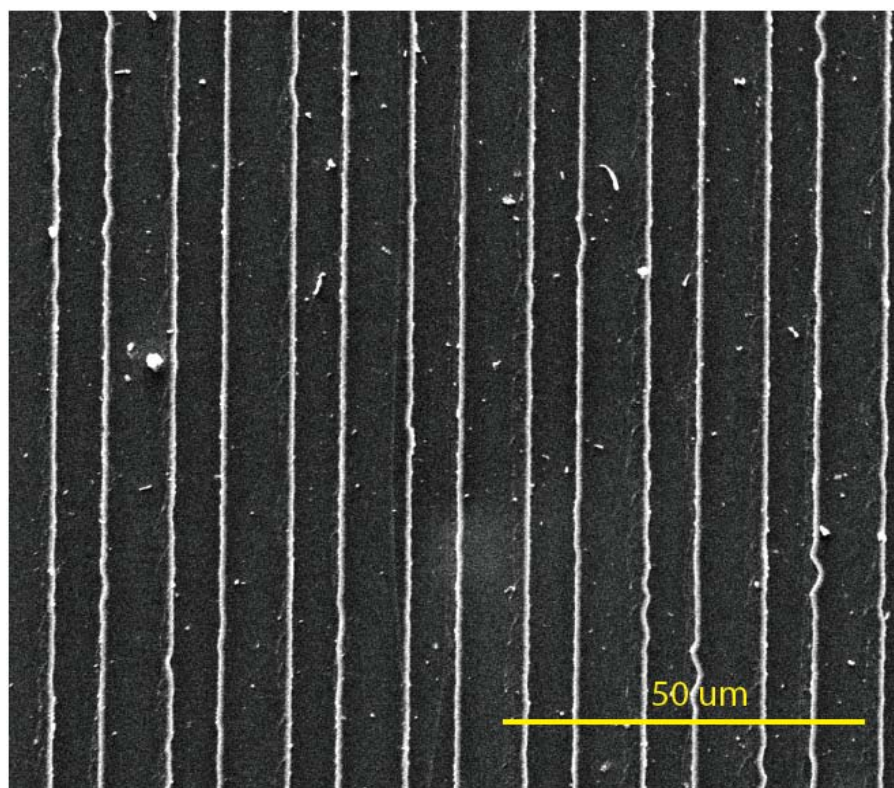


**Figure 4.19-** CdTe nanowire array prepared by alternating UPD of Cd-Te on LPNE substrates.

Just as with nanowires deposited via overpotential deposition, the composition of nanowires deposited UPD by ECALD need to be verified. While this task is not as straight forward with nanowires deposited via ECALD because of the limited sample area, there are still a few routes which can be taken. An electron probe microanalyzer (EPMA) was utilized to

determine the chemical composition of the deposit. EPMA works similar to EDX, in that an electron beam with specific energy bombards the sample which emit X-rays at characteristic wavelengths for specific elements. The X-rays which are emitted are then represented by 'white dots' for a specific element of interest. The EMPA analysis for a ECALD CdTe nanowire is shown in Figure 4.20.

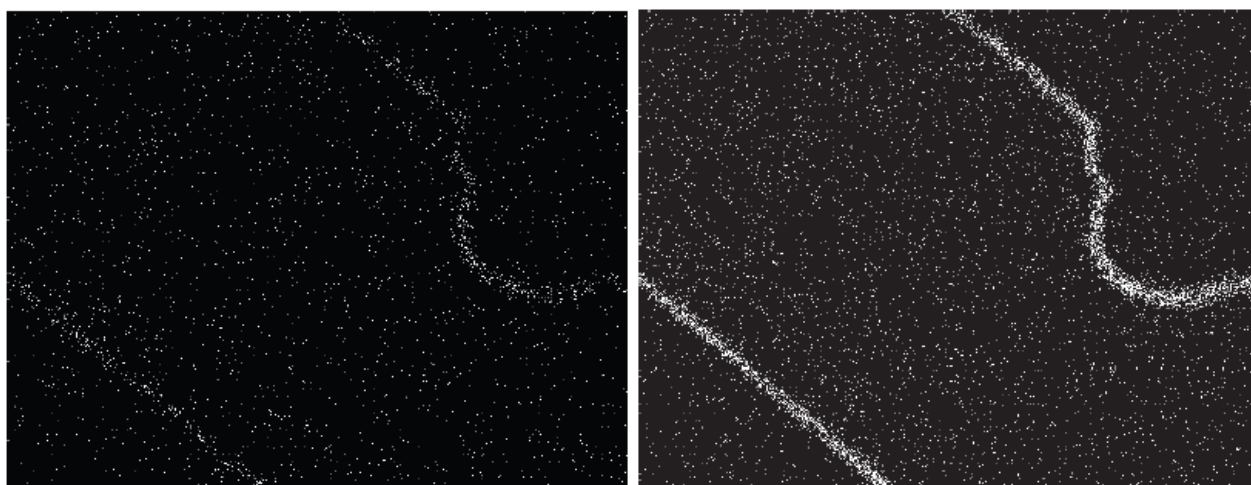


**Figure 4.20-** EPMA of CdTe nanowires by UPD on LPNE substrates.

It was confirmed from EPMA by Brian Perdue that we had in fact synthesized a nanowire with composition of 0.8:1.0, Cd:Te. The excess of Te may create a potential problem for future devices, but can also be eliminated via less UPD time for Te.

Electrical measurements of ECALD were also performed on an array of CdTe nanowires to confirm the semiconducting nature of the nanowire to respond to light. A photoresponsive array of CdTe nanowires also provides

confirmation that ECALD CdTe has been successful as illustrated in Figure 4.21.

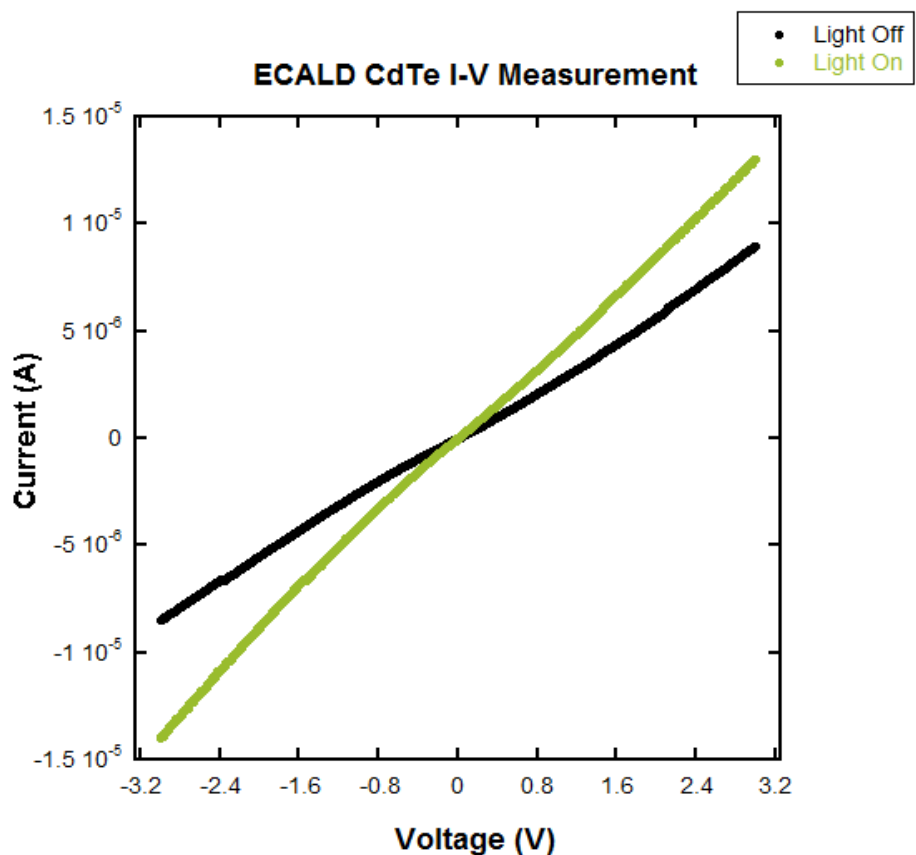


**Figure 4.21-** Light (green) and dark (black) IV curves of an array UPD CdTe nanowires prepared by Stickney's group.

At this point having knowledge that nanowires can in fact be created by exploiting ECALD on LPNE substrates yields the necessary confidence to investigate its potential to create solar cells. Presently I am investigating if core-shell structures can be created by exploiting the ECALD-LPNE relationship to allow for solar cell buildup. Another process for future

investigation would be to determine if HDLPNE can be successful with ECALD. If realized, this would allow for the ability to not only create higher quality devices with an increased surface density for devices which can already be made via LPNE, but additionally provide a more conclusive method by which light trapping properties and LMRs can be investigated in LPNE solar cells as there will be smaller variation in the nanowire width.

As it pertains to creation of an efficient PbSe nanowire based solar cell, ECALD of PbSe has been already been successful in the Stickney group [126]. ECALD of crystalline PbSe nanowires will allow for a more conclusive electrical characterization for the presence of MEG. All MEG measurements to date have been made by means of spectroscopy, the results of which are still up for debate, hence the motivation for an electrical measurement confirmation. PbSe nanowires by ECALD-LPNE would, optimistically, provide crystalline PbSe nanowires in opposition to nanocrystalline nanowires via overpotential deposition, leading to a concrete path for electrical measurements to confirm MEG. Further, by creating ECALD PbSe nanowires with control over two dimensions of the nanowire growth, this allows for a manner by which the PbSe nanowires can be manipulated into 3-dimensional, 2-dimensional, and 1-dimensional regimes at which point the efficiency of MEG can further be characterized. As quantum confinement effects begin to take effect, it would be expected that a difference in 3-

dimensional and 1-dimensional photocurrent would be realized. As the wavelength of input radiation is varied in the 3-dimensional structure, it is hypothesized that the photocurrent remains constant. In stark contrast, the 1-dimensional structure should exhibit a step-like photocurrent response as the input wavelength changes to allow for additional excitons to be generated. Suffice to say, creating ECALD-LPNE PbSe nanowires opens the door for its own independent dissertation work to test for the existence of MEG.

While simultaneously testing for MEG in PbSe ECALD-LPNE nanowires, additional work can be carried out to determine the ideal widths of the gold core and PbSe shell, as well as their subsequent pitch as it pertains to maximizing the efficiency of the PbSe based ECALD-LPNE solar device. In collaboration with Linyou Cao's theoretical results of enhanced absorption in small pitch semiconductor systems, experimental tests can be performed by altering the setup in Figure X to allow for absorption measurements of nanowires; agreement between the theoretical and experimental results would elaborate as to the ideal pitch for the PbSe nanowire. The setup for this measurement process has been prepared according to Figure 4.22. Because I am performing an absorption measurement, there will be the need to employ a monochromatic source which will in turn drastically reduce the input signal on the nanowires. As a result, a lock-in amplifier coupled with a



pre-amp, to amplify signal, was exploited to produce initial absorption results like that in Figure 4.23.

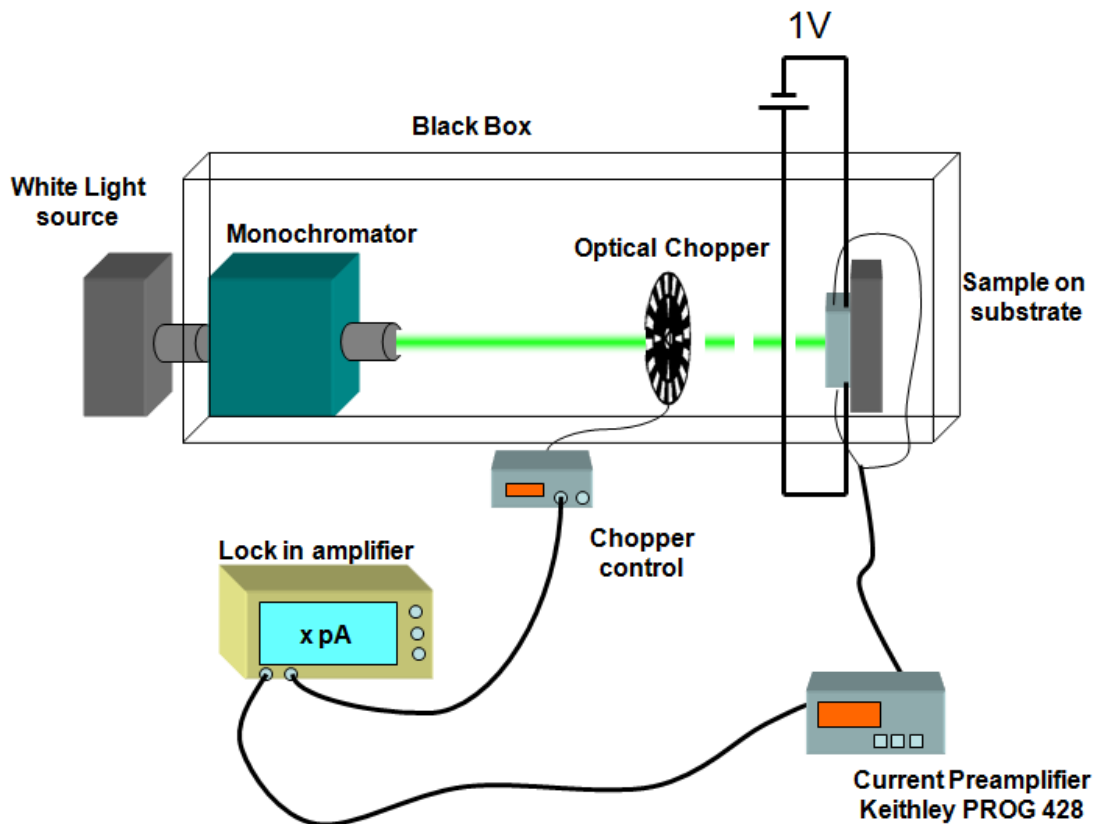


**Figure 4.22-** Experimental setup to measure optical absorption of nanowire arrays.

The lock-in amplifier is used to detect signals at a given reference frequency, in this case the frequency of the light chopper. Because the light chopper determines the frequency at which the nanowires will be blocked and exposed to light, the chopper frequency is the frequency of the nanowire

signal, and therefore the reference frequency will yield a signal which can therefore be trustworthy.

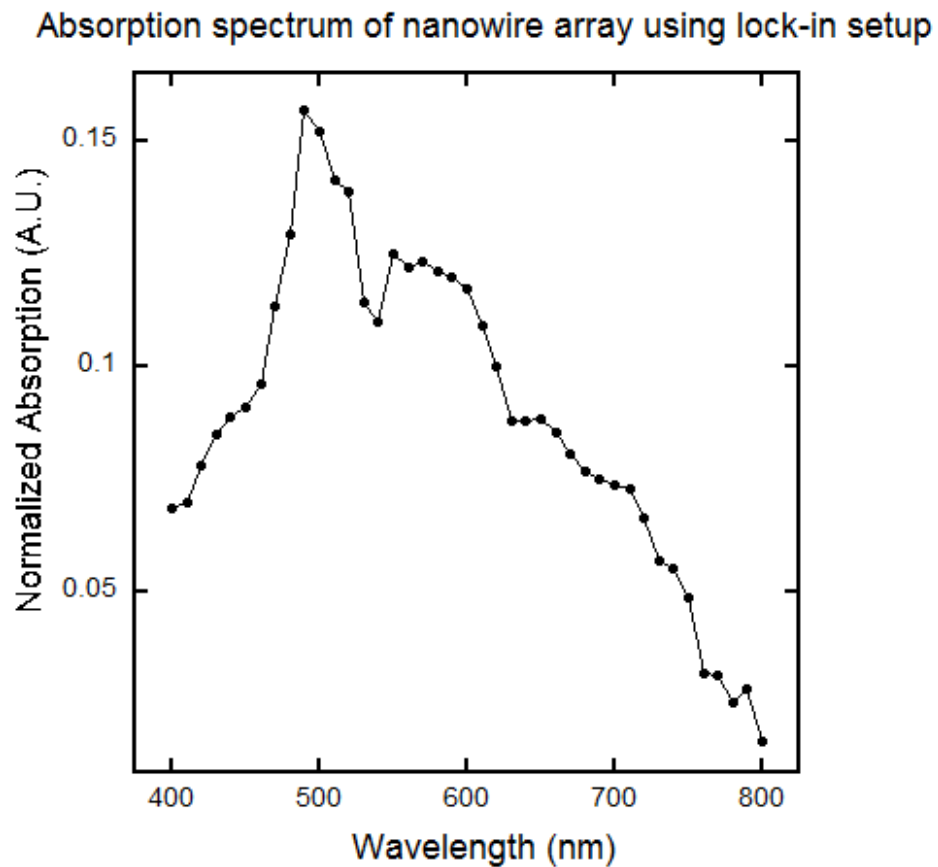


**Figure 4.23-** Absorption spectra of nanowire array using experimental setup in Figure 4.22.

As is the case for studying MEG in ECALD-LPNE PbSe nanowires, in depths study as to how varying the pitch of the semiconductor will affect the LMRs will likely be study of a separate dissertation.

As a result of this dissertation, I have presented the need to address the future worldwide energy demands by using the carbon neutral renewable energy solar cell. The main concern limiting solar cells from being a competitive energy source is their cost effectiveness compared to other mainstream sources. I have presented how I anticipate the creation of a cheap and efficient alternative by using potentially multiple exciton generating PbSe nanowires via LPNE as the semiconductor portion of the cell. I have further illustrated the successful development of the HDLPNE method which will not only for an increase in the active area of the device, but also potentially allow for LMRs and plasmon resonance to enhance the overall efficiency. I continued to display how to successfully fabricate a single nanowire solar cell by employing coaxial LPNE and how the efficiency was enhanced when coupling coaxial and HDLPNE. I have further proposed future routes of investigation as it relates to improving the crystallinity of the nanowires by using ECALD as well as illustrating how the absorption of nanowires, and therefore the leaky-modes, can be identified and measured, with future collaboration with Linyou Cao, to optimize the overall function of the solar cell. This dissertation has laid the groundwork for future students of Professor Erik Menke to continue the work I started with regards to fabrication of a cheap, efficient solar, via the LPNE method and its new found derivatives.

## Bibliography

- [1]. N. Lewis, D. Nocera, *Proceedings of the National Academy of Science of the United States of America*, **2006**, 103, (43), p 15729-15735.
- [2]. Energy Information Administration (**2005**), *Annual Energy Outlook* (U.S. Dept of Energy, Washington, DC).
- [3]. M. Hoffert, K. Caldeira, A. Jain, E. Haites, L. Harvey, S. Potter, M. Schlesinger, T. Wigley, D. Wuebbles, *Nature*, **1998**, 395, p 881-884.
- [4]. United States Development Program (**2003**), *World Energy Assessment Report: Energy and the challenge of sustainability* (United Nations, New York).
- [5]. N. Nakicenovic, R. Swart, eds (**2000**) in *Special Report on Emission Scenarios* (Intergovernmental Panel on Climate Change, Washington DC), p 48-55.
- [6]. J. Petit, J. Jouzel, D. Raynaud, N. Barkov, J. Barnola, M. Bender, J. Chappellaz, M. Davis, G. Delaygue, *et al.*, *Nature*, **1999**, 399, p 429-436.
- [7]. U. Siegenthaler, T. Stocker, E. Monnin, D. Luthi, J. Schwander, B. Stauffer, D. Raynaud, J. Barnola, H. Fischer, V. Masson-Delmontte, *et al.*, *Science*, **2005**, 310, p 1313-1317.
- [8]. E. Moniz, J. Deutch, eds (**2003**) *The Future of Nuclear Power* (Massachusetts Institute of Technology, Cambridge, MA).
- [9]. B. Metz, O. Davidson, H. Loos, L. Meyer, eds (**2005**) *Carbon Dioxide Capture and Storage* (Intergovernmental Panel on Climate Change, Washington, DC).
- [10]. J. Goldemberg, T. Johansson, eds (**2004**) *World Energy Assessment Overview* (United Nations Development Program, New York) ([www.undp.org/energy/weaover2004.htm](http://www.undp.org/energy/weaover2004.htm)).
- [11]. M. Green, *Third Generation Photovoltaics: Advanced Solar Energy Conversion* (Springer-Verlag, Berlin, 2004).

- [12]. N. Lewis, *Science*, **2007**, 315, p 798-801.
- [13]. W. Shockley, H. Queisser, *Journal of Applied Physics*, 1961, 32, p 510-519.
- [14]. V. Klimov, *et al.*, *Applied Physics Letters* **2006**, 89, p 123118.
- [15]. R. Schaller, V. Klimov, *Nanoletters*, **2006**, 6, p 434-429.
- [16]. R. Schaller, V. Klimov, *Applied Physics Letters* **2005**, 87, p 253102.
- [17]. R. Schaller, V. Klimov, *Nanoletters* **2006**, 6, p 424.
- [18]. R. Ellington, A. Efros, *Nanoletters*, **2005**, 5, p 865.
- [19]. M. Hanna, A. Nozik, *Journal of Applied Physics*, **2006**, 100, p 74510.
- [20]. A. Luque, A. Nozik, *MRS Bulletin*, **2007**, 32, p 236-241.
- [21]. M. Gratzel, *Nature*, **2001**, 414, p 338-344.
- [22]. W. Huynh, J. Dittmer, A. Alivisatos, *Science*, **2002**, 295, p 2425-2427.
- [23]. M. Law, L. Greene, J. Johnson, R. Saykally, P. Yang, *Nature Materials*, **2005**, 4, p 455-459.
- [24]. B. Kayes, H. Atwater, N. Lewis, *Journal of Applied Physics*, **2005**, 97, p 114302.
- [25]. Y. Zhang, L. Wang , A. Mascarenhas, *Nano Letters.*, **2007**, 7, p 1264-1269.
- [26]. O. Kluth, B. Rech, L. Houben, S. Wider, G. Schope, C. Beneking, H. Wagner, A. Loffl, H. Schock, *Thin Solid Films*, **1999**, 351, p 247-253.
- [27]. H. Nagel, A. Aberle, R. Hezel, *Progres in Photovoltaics*, **1999**, 7, p 245-260.
- [28]. L. Zeng, P. Bermel, Y. Yi, B. Alamariu, K. Broderick, J. Liu, C. Hong, X. Duan, J. Joannopoulos, C. Kimerling, *Applied Physics Letters*, **2008**, 93, p 221105.
- [29]. J. Zhao, A. Wang, A. Green, F. Ferrazza, *Applied Physics Letters*, **1998**, 73, p 1991-1993.

- [30]. M. Agrawal, P. Peumans, *Optics Express*, **2008**, 16, p 1925–1934.
- [31]. K. Catchpole, A. Polman, *Optics Express*, **2008**, 16, p 21793–21800.
- [32]. P. Bermel, C. Luo, L. Zeng, C. Kimerling, D. Joannopoulos, *Optics Express*, **2007**, 15, p 16986–17000.
- [33]. L. Cao, P. Fan, E. Barnard, A. Brown, M. Brongersma, *Nano Letters*, **2010**, 10, p 2649-2654.
- [34]. L. Cao, P. Fan, M. Brongersma, *Nano Letters*, **2011**, 11, p 1463-1468.
- [35]. L. Cao, J. Park, P. Fan, B. Clemens, M. Brongersma, *Nano Letters*, **2010**, 10, p 1229-1233.
- [36]. L. Cao, P. Fan, A. Vasudev, J. White, Z. Yu, W. Cai, J. Schuller, S. Fan, M. Brongersma, *Nano Letters*, **2010**, 10, p 439-435.
- [37]. L. Cao, J. White, J. Park, J. Schuller, B. Clemens, M. Brongersma, *Nature Materials*, **2009**, 8, p 643-647.
- [38]. J. Nelayah, M. Kociak, O. Stéphan, F. Abajo, M. Tence, L. Henrard, D. Taverna, I. Santos, L. Marzán, C. Colliex, *Nature Physics*, **2007**, 3, p 348-353.
- [39]. M. Stockman, *Physics Review Letters*, **2004**, 93, p 137404.
- [40]. E. Verhanan, M. Spasenović, A. Polman, and L. Kuipers, *Physics Review Letters*, **2008**, 102, p 203904.
- [41]. M. Quinten, A. Leitner, J. Krenn, F. Aussenegg, *Optics Letters*, **1998**, 23, p 1331-133.
- [42]. S. Maier, *Nature Materials*, **2003**, 2, p 229-232.
- [43]. A. Koenderink, A. Polman, *Physics Review B* **2005**, 74, p 33402.
- [44]. R. Zia, M. Selker, P. Catrysse, M. Brongersma, *Journal of Optical Society of America A*, **2004**, 21, p 2442-2446.
- [45]. P. Muhlschlegel, H. Eisler, O. Martin, B. Hecht, and D. Pohl, *Science*, **2005**, 308, p 1607-1609
- [46]. H. Atwater, A. Polman, *Nature Materials*, **2010**, 9, p 205-213.

- [47]. V. Ferry, M. Verschuuren, B. Hongbo, E. Verhagen, R. Walters, H. Atwater, A. Polman, *Optics Express*, **2010**, 18, p 237-245.
- [48]. P. Campbell, M. Green, *IEEE Trans. Electron. Dev.*, **1986**, 33, p 234-239.
- [49] Y. Yang, S. Kung, D. Taggart, C. Xiang, F. Yang, M. Brown, A. Güell, T. Kruse, J. Hemminger, R. Penner, *Nano Letters*, **2008**, 8, p 2447-2457.
- [50]. H. Kim, C. Xiang, A. Güell, R. Penner, E. Potma, *Journal of Physical Chemistry C*, **2008**, 112, p 12721-12727.
- [51]. C. Xiang, S. Kung, D. Taggart, F. Yang, M. Thompson, G. Güell, Y. Yang, R. Penner, *ACS Nano*, **2008**, 2, p 1939-1949.
- [52]. C. Xiang, M. Thompson, F. Yang, E. Menke, L. Yang, R. Penner, *Physica Status Solidi (c)*, **2008**, 5, p 3503-3505.
- [53]. C. Xiang, Y. Yang, R. Penner, *Chemical Communications*, **2009**, 859-873.
- [54]. A. Halpern, N. Nishi, J. Wen, F. Yang, C. Xiang, R. Penner, R. Corn, *Analytical Chemistry*, **2009**, 81, p 5585-5592.
- [55]. F. Yang, D. Taggart, R. Penner, *Nano Letters*, **2009**, 9, p 2177-2182.
- [56]. Y. Yang, D. Taggart, M. Brown, F. Yang, S. Kung, J. Hemminger, R. Penner, *ACS Nano*, **2009**, 3, p 4144-4154.
- [57]. F. Yang, S. Kung, D. Taggart, R. Penner, *Sensor Letters*, **2010**, 8, p 534-538.
- [58]. S. Kung, W. Xing, K. Donovan, F. Yang, R. Penner, *Electrochimica Acta*, **2010**, 55, p 8074-8080.
- [59]. S. Kung, W. Veer, F. Yang, K. Donovan, R. Penner, , **2010**, 10, p 1481-1485.
- [60]. F. Yang, S. Kung, M. Cheng, J. Hemminger, R. Penner, *ACS Nano*, **2010**, 4, p 5233-5244.

- [61]. J. Arter, D. Taggart, T. McIntire, R. Penner, G. Weiss, *Nano Letters*, **2010**, 10, p 4858-4862.
- [62]. Y. Yang, D. Taggart, M. Cheng, J. Hemminger, R. Penner, *Journal of Physical Chemistry Letters*, **2010**, 1, p 3004-3011.
- [63]. D. Taggart, Y. Yang, S. Kung, T. McIntire, R. Penner, *Nano Letters*, **2011**, 11, p 125-131.
- [64]. K. Donovan, J. Arter, R. Pilolli, N. Cioffi, G. Weiss, R. Penner, *Analytical Chemistry*, **2011**, 83, p 2420-2424.
- [65]. S. Kung, W. Xing, W. Veer, F. Yang, K. Donovan, M. Cheng, J. Hemminger, R. Penner, *ACS Nano*, **2011**, 5, p 7627-7639.
- [66]. W. Yan, T. Ayvazian, J. Kim, Y. Liu, K. Donovan, W. Xing, Y. Yang, J. Hemminger, R. Penner, *ACS Nano*, **2011**, 5, p 8275-8287.
- [67]. A. Nozik, *Chemical Physics Letters*, **2008**, 457, p 3-11.
- [68]. M. Hanna, A. Nozik, *Journal of Applied Physics*, **2006**, 100, p 74510.
- [69]. V. Klimov, *Applied Physics Letters*, **2006**, 89, p 123118.
- [70]. R. Kane, R. Cohen, R. Sibley, *Journal of Physical Chemistry*, **1996**, 100, p 7928-7932.
- [71]. R. Schaller, M. Sykora, J. Pietryga, V. Klimov, *Nano Letters*, **2006**, 6, p 424-429.
- [72]. R. Ellington, M. Beard, J. Johnson, P. Yu, M. Olga, A. Nozik, A. Shabaev, A. Efros, *Nano Letters*, **2005**, 5, p 865-871.
- [73]. S. Kim, W. Kim, Y. Sahoo, A. Cartwright, P. Prasad, *Applied Physics Letters*, 2008, 92, p 31107.
- [74]. J. Luther, M. Beard, Q. Song, M. Law, R. Ellington, A. Nozik, *Nano Letters*, **2007**, 7, p 1779-1784.
- [75]. M. Park, S. Connor, T. Mokari, K. Gaffney, *Nano Letters*, **2009**, 9, p 1217-1222.



- [76]. H Saloniemi, T. Kanninen, M. Ritala, M. Leskela, *Journal of Materials Chemistry*, **1998**, 8, p 651-654.
- [77]. H. Saloniemi, M. Kemell, M. Ritala, M. Leskela, *Journal of Materials Chemistry*, **2000**, 10, p 519-525.
- [78]. J. Blackburn, H. Chappell, J. Luther, A. Nozik, J. Johnson, *Journal of Physical Chemistry Letters*, **2011**, 2, p 599-603.
- [79]. E. Burnstein, F. Johnson, R. Loudon, *Physics Review*, **1965**, 139, p 1239-1245.
- [80]. Y. Batonneau, C. Bremard, J. Laureyns, C. Merlin, *Journal of Raman Spectroscopy*, **2000**, 31, p 1113-1119.
- [81]. L. Black, P. Frost, *Applied Spectroscopy*, **1995**, 49, p 1299-1304.
- [82]. L. Burgio, J. Clark, S. Firth, *Analyst*, **2001**, 126, p 222-227.
- [83]. D. Smith, S. Firth, R. Clark, M. Cardona, *Journal of Applied Physics*, **2002**, 92, p 4375-4380.
- [84]. J. Shapter, M. Brooker, M. Skinner, *International Journal of Mineral Processes*, **2000**, 60, p 199-201.
- [85]. M. Fardy, A. Hochbaum, J. Goldberger, M. Zhang, Yang, *Advanced Materials*, **2007**, 19, p 3047-3051.
- [86]. A. Sashchiuk, L. Amirav, M. Bashouti, M. Krueger, U. Sivan, E. Lifshitz, *Nano Letters*, **2004**, 4, p 159-165.
- [87]. L. Burn, *Society of Photo-Optical Instrumentation Engineers*, **2002**, 1, p 7-12.
- [88]. T. Ito, S. Okazaki, *Nature*, **2000**, 406, p 1027-1031.
- [89]. L. Pan, Y. Park, Y. Xiong, E. Ulin-Avila, Y. Wang, L. Zeng, S. Xiong, J. Rho, C. Sun, D. Bogy, X. Zhang, *Nature*, **2011**, 1, p 1-6.
- [90]. J. Anker, *et al.*, *Nature Materials*, **2008**, 7, p 442-453.
- [91]. A. Dionne, A. Sweatlock, H. Atwater, A. Polman, *Physics Review B*, **2006**, 73, p 35407.

- [92]. M. Stockman, *Physics Review Letters*, **2010**, 10, p 137404.
- [93]. A. Aubry, et al., *Nano Letters*, **2010**, 10, p 2574-2579.
- [94]. E. Verhagen, L. Kuipers, A. Polman, *Nano Letters*, 10, 3665-3669.
- [95]. D. Gramotnev, K. Vernon, *Applied Physics B-Laser Optics*, **2007**, 86, p 7-17.
- [96]. C. Durkan, M. Schneider, M. Welland, *Journal of Applied Physics*, **2000**, 61, p 14215-14218.
- [97]. S. Chou, Q. Xia, *Nature Nanotechnology*, **2008**, 3, p 295-300.
- [98]. T. Nguyen, J. Nagarah, Y. Qi, S. Nonnemann, A. Morozov, S. Li, C. Arnold, M. McAlpine, *Nano Letters*, **2010**, 10, p 4595-4599.
- [99]. Y. Qi, J. Kim, D. Nguyen, B. Lisko, P. Purohit, M. McAlpine, *Nano Letters*, **2011**, 11, p 1331-1336.
- [100]. S. Ghosh, J. Hujdic, A. Villicana-Bedolla, E. Menke, *Journal of Physical Chemistry C*, **2011**, 115, p 17670-17675.
- [101]. W. Ma, et al., *ACS Nano*, **2011**, 5, p 8140.
- [102]. J. Tang, et al., *Nature Materials*, **2011**, 10, p 76.
- [103]. J. Choi, Y. Lim, M. Santiago-Berrios, M. Oh, B. Hyun, L. Sun, A. Bartnik, A. Goedhart, G. Malliaras, H. Abruna, F. Wise, T. Hanrath, *Nano Letters*, **2009**, 9, p 3749-3755.
- [104]. K. Leschkies, T. Beatty, M. Kang, D. Norris, E. Aydil, *ACS Nano*, **2009**, 3, 3638-3648.
- [105]. W. Ma, S. Swisher, T. Ewers, J. Engel, V. Ferry, H. Atwater, P. Alivisatos, *ACS Nano*, **2011**, 5, p 8140-8147.
- [106]. B. Murray, S. Sun, W. Gaschler, H. Doyle, T. Betley, R. Kagan, *IBM Journal of Research Development*, **2001**, 45, p 47-56.
- [107]. J. Luther, M. Beard, Q. Song, O. Reese, J. Ellington, A. Nozik, *Nano Letters*, **2008**, 8, p 3488-3492.

- [108]. G. Nair, L. Chang, S. Geyer, M. Bawendi, *Nano Letters*, **2011**, 11, p 2145-2151.
- [109]. O. Semonin, J. Luther, S. Choi, H. Chen, J. Gao, A. Nozik, M. Beard, *Science*, **2011**, 334, p 1530-1533.
- [110]. P. Klocek, *Handbook of Infrared Optical Material*, Marcel Dekker, New York, 1991.
- [111]. K. Fuchs, *Proceedings of Cambridge Philosophical Society*, **1938**, 34, p 100-108.
- [112.] E. Sondheimer, *Advanced Physics*, **1952**, 1, p 1-42.
- [113]. A. Mayadas, M. Shatzkes, *Physics Review B: Solid State*, **1970**, 1, p 1382-1389.
- [114]. B. Gregory, J. Stickney, *Journal of Electroanalytical Chemistry*, **1991**, 300, p 543-561.
- [115]. T. Oznuluer, I. Erdogan, I. Sisman, U. Demir, *Chemistry of Materials*, **2005**, 17, p 935-937.
- [116]. R. Vaidyanathan, J. Stickney, U. Happek, *Electrochimica Acta*, **2004**, 49, p 1321-1326.
- [117]. T. Tsukasa, S. Takabayashi, H. Mori, S. Kuwabata, *Journal of Electroanalytical Chemistry*, **2002**, 522, p 33-39.
- [118]. M. Lay, J. Stickney, *Journal of The Electrochemical Society*, **2004**, 151, p 431-435.
- [119]. D. Kolb, *Advances in Electrochemistry and Electrochemical Engineering*, **1980**, 11, p 125.

- [120]. B. Hayden, I. Nandhakumar, *Journal of Physical Chemistry B*, **1998**, 102, p 4897-4905.
- [121]. M. Panicker, M. Knaster, F. Kroger, *Journal of The Electrochemical Society*, **1978**, 125, p 566.
- [122]. M. Bouroushian, *Electrochemistry of Metal Chalcogenides*, **2010**, p 78.
- [123]. R. Vaidyanathan, S. Cox, U. Happek, D. Banga, M. Mathe, J. Stickney, *Langmuir*, **2006**, 22, p 10590-10595.